A Non-Invasive, Near-Field and Very Near-Field, Phaseless Antenna Characterization System

Pietro Vinetti

November, 2008

TESI DI DOTTORATO

UNIVERSITÀ DEGLI STUDI DI NAPOLI "FEDERICO II"

DIPARTIMENTO DI INGEGNERIA ELETTRONICA
E DELLE TELECOMUNICAZIONI

DOTTORATO DI RICERCA IN
INGEGNERIA ELETTRONICA E DELLE TELECOMUNICAZIONI

A NON-INVASIVE, NEAR-FIELD AND VERY NEAR FIELD, ANTENNA CHARACTERIZATION SYSTEM

PIETRO VINETTI

Il Coordinatore del
Corso di Dottorato

Ch.mo Prof. Giovanni Poggi

Il Tutore

Ch.mo Prof. Giuseppe D'Elia

A. A. 2007–2008

Contents

List of Figures

List of Tables

Introduction

Since the beginning of 50's, Near Field (NF) antenna experimental characterization has been addressed by the antenna community [51, 117] and, in the last decades, Near Field-Far Field (NF-FF) techniques have been developed for various scanning geometries and successfully implemented [57, 58, 53], becoming nowadays an accurate, reliable and well established process for the antenna experimental characterization. Indeed, the characterization of high performance experimental or commercial antennas, as radars [74], military or satellite telecommunication antennas [54, 55] and radomes [56] is performed by near-field (NF) techniques.

The determination of the radiative parameters of the Antenna Under Test (AUT) by measuring the field radiated in its near zone has allowed a dramatic reduction of the dimensions of test facilities, making the indoor characterization practical for a wide class of antennas such as large arrays, satellite antennas and radar antennas, where Fraunhofer [110] distances were too large for using conventional indoor test ranges. Therefore, the use of anechoic chambers has been totally enabled in antenna characterization, ensuring controllable test conditions as close as possible to those of theoretical model and avoiding that high EM power were radiated in the external environment as can occur in the outdoor case.

Standard NF-FF techniques determine the AUT radiation pattern from the knowledge of the tangential component of the electromagnetic (EM) field radiated on a surface with preassigned geometry (frequently planar, cylindrical or spherical) located in the NF zone and enclosing the radiator. Typically, open ended waveguides (OEW) are employed as field probes. Accordingly, the scanning surface cannot be placed as close as desired to the antenna, because of unavoidable coupling effects between the AUT and probe. In addition, the coaxial cables needed to connect the OEW to the measurement chain represents another source of perturbation, as they act as both electromagnetic scatterers and receiving antennas. Therefore, to ensure accurate measurement,

the NF acquisition surface is typically placed at distances not smaller than some (6-7) wavelengths from the AUT.

Nevertheless, increasing the distance of the acquisition surface from the AUT implies a wider acquisition domain in order to ensure the same truncation error on the field data. A more significant truncation error on the near-field measurement can indeed limit the accuracy of NF-FF transformation techniques, reducing the region inside which the FF pattern estimate is reliable. Consequently, dimensions required to the test facility become larger as well as longer scanning times are needed. Even if it is worth noting that a reduction of measurement times can be obtained adopting non-conventional sampling strategies, based on *local field properties* [95]. However, these strategies cannot be exploited when measurement is performed in the close proximity of the radiation source. Thus, the measurement set-up is also required to satisfy tighter requirements on time-stability. Therefore, especially when dealing with low frequencies, indoor test-ranges for testing electrically (and thus physically) large AUTs become very expensive both in terms of installation and operating costs. Furthermore, moving away the acquisition surface from the EM radiation source can worsen the Signal-to-Noise Ratio (SNR), as radiated field presents lower intensities while clutter reflections from side-walls provide essentially a significant contribution to the measure.

Therefore, the distance of the measurement surface from the AUT is determined by trading off two opposing needs: ensuring a non-perturbing measurement of the NF field radiated by the AUT and an accurate and complete measurement of the NF of the radiator.

The issues above described have recently addressed the research for alternative probes. Photonic techniques for the electromagnetic field measurement and in particular electro-optic (EO) sensing have been rapidly recognized as an attractive alternative to OEW, because of the possibility of fully dielectric probes, the use of fiber optics for signal routing and the high immunity to noise and interferences [14]. Dielectric probes, indeed, can provide small sized, lightweight sensing devices with a reduced scattering section, that is definitively negligible when compared to that one of OEW. In addition, they require optical fibers for the connection to the measurement chain eliminating the perturbing coaxial cables. Hence, EO field Sensors (EOSs) represent an attractive solution, especially in all those applications where measurements in the close proximity of the radiator are of interest.

Accordingly, in last years a significant effort has been devoted to the development of non-invasive EOSs, and to date some prototypes have been devel-

oped and experimentally tested [15, 16, 17, 18, 19, 20, 21, 22]. Notwithstanding, the promising results already achieved, the use of EOSs, especially in NF antenna characterization, represents still a border solution, not commercially implemented. This has been essentially ascribed to the reduced sensitiveness in terms of minimum detectable electric field intensity and the low polarization isolation that photonic probe prototypes, typically, have shown when compared to conventional OEW probes.

Another important aspect that significantly bears on the complexity of antenna NF characterization systems is the measurement of the phase of the EM field. As mentioned above, standard NF-FF transformation techniques require the knowledge of the amplitude and the phase of the NF (complex field) tangential component to the measurement surface. Unfortunately, phase measurements enforce stricter specifications on the components of the antenna NF characterization system. Indeed, it requires more sophisticated vector network analysers (VNA) [59], phase-stable cables [60], positioners with high accuracy [61, 62], controlling systems of the environmental conditions (humidity, temperature), that typically become more and more expensive with the increasing frequency. And, moreover, when dealing with the appealing millimetre and sub-millimetre bandwidths [109], constraints imposed by phase measurements can hardly be satisfied by NF facility equipments and the accuracy of the measurements can be significantly reduced, up to become unacceptable in some cases. Accordingly, reliability of conventional NF-FF transformation techniques is compromised, making NF characterization impracticable.

These considerations have pursued the development of alternative NF-FF phaseless techniques, able to estimate the FF pattern by only amplitude data. In particular, in the last decades various *phaseless* NF-FF techniques have been developed [63, 64, 65, 66], able to retrieve the phase information from only amplitude data.

In particular, in the last years at *Dipartimento di Ingegneria Biomedica Elettronica e Telecomunicazioni* (DIBET) of *University of Naples Federico II* effective phaseless NF-FF techniques have been successfully developed [71, 72, 73] and extensively experimentally validated [74, 75], even at millimetre-wave frequencies [76, 77]. It is worth noting that the above described issues, concerning the dimensions of the test facilities, the truncation error and the time-stability of apparatus, are particularly critical in phaseless characterization, as long as to accurately recover the missing phase information, two acquisition surfaces, located in the NF of the radiator and sufficiently spaced apart, are typically required.

The research activity, accomplished during the Ph.D. Course, has been devoted to the development and the experimental validation of an antenna NF characterization system with performances not available in the current conventional systems. The basic idea is to conjugates benefits of photonic techniques for the EM field measurement with advantages of NF-FF phaseless transformation techniques, providing a innovative solution for antenna characterization. In particular, in the thesis an antenna NF characterization system, where NF measurements are accomplished by means of a non-invasive EOS and FF pattern estimates exploit phaseless techniques, is presented. Such a system is, indeed, able to provide the following features.

(i) **Reduction of the dimensions of test facility** - The non-invasiveness of EOS allows to perform NF measurements in the close proximity of the AUT, enabling eventually even measurements in the reactive zone. Thus, a significant reduction of the dimensions of the test facility is obtained, leading to Compact Near Field (CNF) or even to Very Near Field (VNF) antenna characterization systems, where the measure is performed in the reactive zone [51] of the radiator. In addition, the easy probe handling, that can be provided by dielectric sensors, makes practical positioning systems able to scan unconventional (or radiator tailored) surfaces, further contributing to the compactness of the facility.

(ii) **Improvement of the accuracy of the characterization** - Drawing the acquisition surface in the close proximity of the AUT ensures a significant reduction of the truncation on the NF mapping, when open surfaces are exploited. At the same time, the reduction of the distances between AUT and the probe makes higher SNR.

(iii) **Reduction of the the operating costs** - In general, for a given truncation level on the data, smaller acquisition surfaces are required when reducing the distance from the AUT. But, moreover, the non-invasive behaviour, the small size and the lightweight, that typically characterizes EOS, allow to implement Probe Arrays (PA), where multiple sensors operates in parallel to simultaneously collect a set of samples. Accordingly, Fast Near Field (CNF) systems can be realised, where a significant speeding up of the measurement is accomplished by means of a PA.

(iv) **Reduction of the complexity of the system** - The necessity of measuring only the amplitude of the NF relaxes the the strict specifications imposed on the equipments of test facilities by phase measurement. Indeed amplitude measurement does not suffer from the issues pointed out in the case

of phase measurements, and can be accomplished with a less expensive instrumentation and easier procedures.

The research has been articulated on two independent main topics. On one side, the design of a photonic probe with performances adequate to the be employed in the antenna NF characterization. On the other, the development of effective phaseless NF-FF transformation techniques, providing accurate and reliable pattern estimate for a large class of antennas. These research topics have been pursued also by means of cooperations established between DIBET and both National and International Institutions. In particular, the design of the photonic sensor has been carried out inside a cooperation with the *Dipartimento di Elettrica ed Elettronica* (DEE) of *Politecnico di Bari* and *Centro per la Ricerca Elettronica in Sicilia* (CRES).

In order to develop an antenna characterization system with the above described features, the photonic sensor is required to provide: a low scattering section enabling non-perturbing measurements, a high sensitivity compliant with that typical in conventional NF measurement in indoor test facilities, an high polarization isolation able to select the field component of interest and an appropriate operative bandwidth compatible with the class of radiators to be characterized. Different design strategies have been pursued which have resulted in many configurations, each covered by a numerical analysis aimed to assess its advantages and drawbacks. This analysis allowed to determine an innovative solution, able to meet all the above requirements. In fact, the final configuration proposes a device in integrated optics, based on an Electro-Optic (EO) modulator with Travelling Wave (TW) electrodes.

Concerning the phaseless NF-FF transformations, the proposed antenna NF characterization system has required the development of effective and reliable phase retrieval techniques, able to operate with a broad class of radiators. In particular, on the basis of recent remarkable results, achieved at DIBET [71, 72, 73], a general approach, able to provide reliable and accurate results even in the difficult case of steered-beam antennas [74], has been developed for the planar scanning geometry. The developed technique employs a suited mathematical modeling that can incorporate all the *a-priori* information available on the problem, in order to mitigate ill-conditioning and trapping that typically affects phase retrieval when it is faced as the optimization of a proper objective functional. This approach has been demonstrated to provide accurate results also in estimate of the FF pattern side lobes[74], where typically accuracy of phaseless approaches is reduced [111]. The developed approach has been also made robust against mild incoherence (measurement planes mis-

alignment), that typically affects the collected data. Finally, the technique has been successfully extended to cylindrical scanning geometry.

In this thesis, the research activities accomplished and the result obtained during the Ph.D., that has leaded to the development and the the experimental validation of the an antenna NF characterization system with the above mentioned features, are described, enlightening its innovative potentialities in terms of CNF, FNF and VNF. It's worth noting that, although the realisation of a prototype of the designed EO sensor, is currently scheduled at the laboratories of *Selex Sistemi Integrati*, the experimental validation of the characterization system has been performed exploiting the promising photonic probe developed at the *Electromagnetic Wave Division* of the *Advanced Industrial Science and Technology* of Japan [19]. Indeed, by means of a cooperation between DIBET and AIST it has been possible to spend a part of the Ph.D at AIST laboratories (Tsukuba, Japan), where the validation of the proposed system has been successfully accomplished.

The outline of the thesis is the following:

Chapter 1 provides some necessary notions, the nomenclature and the symbols of optics of crystals and electro-optical modulation, that will be essential to understand EO sensors and the design choices of the proposed solution. Furthermore, in order to enligthen the innovative aspects of the proposed solution, the *state of the art* on the topic of EO sensor is presented by means of a review of the most remarkable and original configurations currently described in the literature.

Chapter 2 addresses the design of the EO probe, core of the NF acquisition system. Some of the most interesting configurations that have been considered during the research activities are also presented, enlightening their advantages and their limitations in order to provide a sound understanding of the final design choices.

Chapter 3 addresses the development of phaseless NF-FF techniques. The phase retrieval problem, the mathematical modelling together with the related issues and the role of a-priori information are first discussed. Then, the adopted strategy, based on an effective representation of the aperture field and a proper sampling strategy, is described. The problem of mild incoherence on data is faced and the extension to cylindrical case is presented. The chapter

ends with the experimental results of the developed technique in some relevant and real-world test cases.

Chapter 4 presents the innovative potentialities available with the antenna characterization system proposed. In particular, it describes the features of compact near field test ranges, fast near-field test ranges and very near field test ranges. In this last case, an outline of effective sampling strategy currently under development at DIBET are discussed with some numerical results. At last, the experimental validation of the proposed NF characterization system is reported.

Chapter 1

Dielectric Sensor for Electromagnetic Field Measurement

The interest in photonic sensing of electromagnetic field raised at the beginning of the 80's, encouraged especially by the need for higher frequency characterization [1] of electronic circuits [2]. Even if, the idea of exploiting optical properties of materials, such as Pockels or Farady effect [3], to measure electric or magnetic fields has been already considered in 70's [4]. Because of the possibility of fully dielectric probes, EO sensing became attractive for electromagnetic compatibility (EMC) and free space measurements, such as antenna NF characterization [5]. Notwithstanding this interest, only at the end of 80's the first prototypes of innovative dielectric probes, appeared in the open literature [6, 7, 8].

During the 90's the improvements of fabrication techniques of integrated optics devices has significantly pursued the research for *non-invasive* probes. In addition, the increase of the environmental exposure to artificial EM fields, that has characterized the last decades, have made EM field monitoring, especially in proximity of the radiation sources, a relevant topic in the EM scientific community. Accordingly, the interest for non invasive dielectric probes, able to introduce a negligible perturbation in the measurement, have increased making it nowadays a *hot topic* in EM sensing research [9].

The basic idea of the investigation is to develop a *non invasive* device able to transduce a radio-wave signal into an optical one, so that OEW probes and the coaxial cables could be replaced by the transducer and fiber optics in the

measurement chain, respectively. In Fig. 1.1 the schematic of the optical measurement of radio waves is presented.

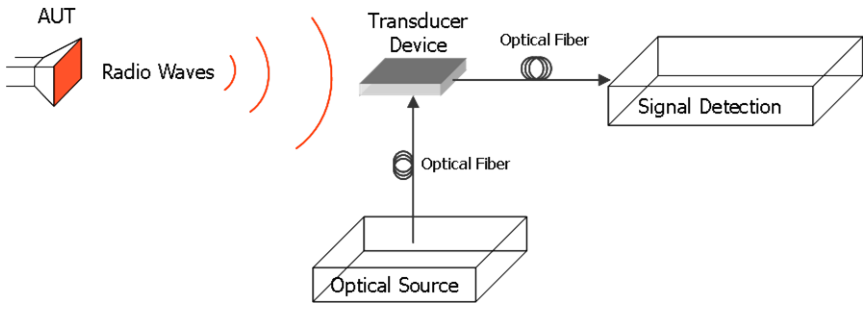

Figure 1.1: Optical Measurement of Radio waves

Various physical phenomena, arising in particular dielectric materials and related to the interaction of microwaves and optical properties of the media, have been considered in order to realize the non invasive transducer. Among the most relevant ones, electro-optic (EO) effect, photo-absorption effect, magneto-optic effect, thermo-optic effect have been investigated [3]. Some alternative probes prototypes have been also developed [10, 11, 12, 13]. Naturally, their performances and the operating bandwidth can significantly vary, depending on the phenomena, the chosen material, the topology and the realization process. In last years, sensors based on EO effect have been demonstrating to be the most promising [14] in terms of performances and also practicability, for the radio-wave signal measurements. Accordingly, investigations on alternative probes have been mainly focused on this phenomena and several prototypes, based on different materials and different technologies, have been developed and experimentally tested [15, 16, 17, 18, 19, 20, 21, 22].

The aim of this first chapter is to present, together with the relative nomenclature and symbols, the basic notions concerning optics of crystals, EO effect, EO modulators and their quality parameters. These concepts which will be essential and used throughout the whole text. Furthermore, a review of the most remarkable and original configurations of EO field sensors (EOS), which are currently described in the literature, is presented. Accordingly, the *state of the art* of the topic will be presented to enlighten the innovative aspects of the solution proposed in the thesis. We also present the integrated photonic sensor, developed at AIST, that has been actually employed in the measurement campaigns for the experimental validation of the proposed NF antenna charac-

terization system.

1.1 Electro-Optic Effect

Electro optic effect [3] is typical of some anisotropic crystal and consists in a variation of the optical dielectric tensor tensor [23] in presence of an external electromagnetic field. This effect belongs to a class of non-linear phenomena of the material that can be more generally modelled as follows:

$$\boldsymbol{D} = \underline{\epsilon}(\boldsymbol{E}^m)\boldsymbol{E} \tag{1.1}$$

where $\boldsymbol{E^m}$ is the external EM field, $\underline{\epsilon}$ is the optical dielectric tensor, $\boldsymbol{D}$ and $\boldsymbol{E}$ are the optical electric induction and field, respectively [23, 3]. EO effect manifests itself as far as the frequency of the external field is much lower that the optical one. Hence, it is remarkable in the microwave or even in the millimetre bandwidth as well.

By expanding the tensor $\underline{\eta} = \epsilon_0 \underline{\epsilon}^{-1}$ [24], being ϵ_0 the vacuum permittivity, in Fourier series with respect to $\boldsymbol{E}^m$ and truncating to the second order term we get:

$$\underline{\eta}_{ij} \cong \eta_{ij}(0) + \sum_k r_{ijk} E_k^m + \sum_{kl} s_{ijk} E_k^m E_l^m,\ i,j,k,l = 1,2,3 \tag{1.2}$$

where subscripts $1, 2, 3$ indicate respectively the component x, y, z in a Cartesian reference system $0xyz$, whose axes are parallel to the dielectric principal axes [23] of the crystal, and:

$$\begin{cases} r_{ijk} = \frac{\partial \eta_{ij}}{\partial E_k^m} | \boldsymbol{E}^m = 0 \\ \\ s_{ijk} = \frac{\partial \eta_{ij}}{\partial E_k^m \partial E_l^m} | \boldsymbol{E}^m = 0 \end{cases} \qquad i,j,k = 1,2,3 \tag{1.3}$$

Accordingly, two different types of EO can be distinguished: Pockels effect (r_{ijk} coefficients), where the refraction index is linearly dependent on the external field, and Kerr effect (s_{ijkl} coefficients), where the refraction index varies not linearly with external field [3]. Typically, only one of the two effect is dominant and the other can be neglected, therefore, EO crystals can be subdivided in two classes: linear and not linear. From now on we will refer to the Pockets effect, as it is the case of more relevant interest for the purposes of the

work.

Exploiting its symmetry properties, the linear electro-optic tensor [23, 24], given by $(r)_{ijk},\ i,j,k=1,2,3$, can be re-arranged in a 6×3 matrix, whose elements are indicated as electro-optic coefficients [3]:

$$\Delta(\frac{1}{n^2})_p=\sum_k r_{pk}E_k^m,\ p=1,2,3,4,5,6 \text{ and } k=1,2,3 \tag{1.4}$$

where p identifies the specific coefficient $(\frac{1}{n^2})$ of the optical indicatrix [3].

Many inorganic crystals manifest a remarkable EO effect, but Lithium Niobate ($LiNbO_3$) is the most commonly used for EO devices, due to the high values of the elements of the EO tensor and to its relatively easy growth process [122]. However, DAST (4-dimehylamino-N-methyl-4-stilbazolium tosylate) organic ionic salt crystal, whose EO capabilities are potentially superior over the other EO crystals, have been recently re-considered in integrated optics applications, as new advanced techniques for growing have been developed [26]. Lithium Niobate is an uni-axial tri-gonal (3m) crystal [3], therefore the presence of an external EM field with the only z-component does not affect the direction of its principal dielectric axes, but only the refractive indexes:

$$\begin{cases} n_0(E_z)=n_0-\frac{1}{2}r_{13}n_o^3E_z \\ n_e(E_z)=n_e-\frac{1}{2}r_{33}n_e^3E_z \end{cases} \tag{1.5}$$

where n_o and n_e are respectively the ordinary and the extraordinary refractive indexes in absence of the EM field.

1.2 Electro-Optic Modulation

EO modulation [3] consists in the modulation of an optical signal by a external EM field. By exploiting EO effect different modulations scheme can be accomplished, but all essentially based on a phase modulation. The basic idea is, indeed, to exploit the EO effect to change the refractive index of the crystal by applying a voltage with electrodes. Accordingly, the phase of an optical signal propagating trough the crystal is related to the applied voltage. Then, if needed, the phase modulation can be converted in a different scheme by introducing in the optical circuit proper components. Typically, amplitude modulation is adopted, thanks to its relatively easiness in the demodulation stage [27].

A quantitative parameter that typically is used to indicate synthetically the performances of a phase EO modulator is the *half wave* voltage [3], say V_π, that represents the voltage amplitude to be applied to accomplish a phase shift of π (hence a change in the signum) in the output signal:

$$\Delta\phi = \pi \frac{V}{V_\pi} \tag{1.6}$$

where V is the applied voltage and $\Delta\phi$ is the phase shift between the input and the output signal of the modulator. Indeed, for a given phase shift, EO modulators with low value of V_π require a lower driving voltage to accomplish the shifting [24]. Naturally, the half-wave voltage is strictly related to the EO material properties and the geometrical characteristics of the modulator.

EO phase modulators can be classified in *transverse* and *longitudinal*. In transverse modulators the modulating field is transverse with respect of the propagation direction of the optical signal. Conversely, longitudinal modulators have the modulating field parallel to the direction of propagation of the optical signal. The following sub-section will briefly present the two kind of modulators enlightening their main features.

1.2.1 Longitudinal EO modulators

In longitudinal EO modulator the modulating field is parallel to the direction of propagation of the optical beam. Therefore, electrodes are placed on the faces of the EO material where the optical signal impinges and comes out. In fig. 1.2 a schematic of EO longitudinal modulator is depicted. The input polariser filters out all the undesired field components from the optical beam, allowing the proper polarisation to imping on the crystal [3]. For a longitudinal EO modulator in $LiNbO_3$, the half-wave voltage, V_π is given by, [3]:

$$V_\pi = \frac{\lambda_o}{r_{13} n_o^3} \tag{1.7}$$

where λ_o is the optical wavelength. It's worth noting that in eq. 1.7 there is no dependence on the active length, L, i.e. the length of the modulator. This is a general feature of longitudinal modulators: the active length does not affect V_π value.

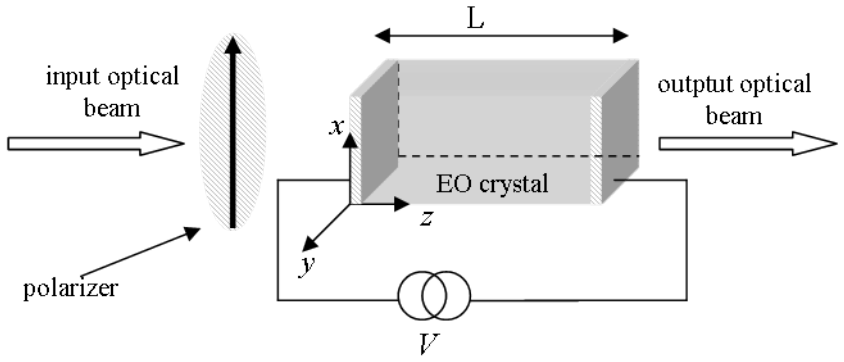

Figure 1.2: Longitudinal EO Modulator Schematic

1.2.2 Transverse EO modulators

Transverse EO modulators have electrodes deployed along faces parallel to the propagation direction of the optical beam. A schematic of EO transverse modulator is represented in Fig. 1.3: For the transverse EO modulator in $LiNbO3$,

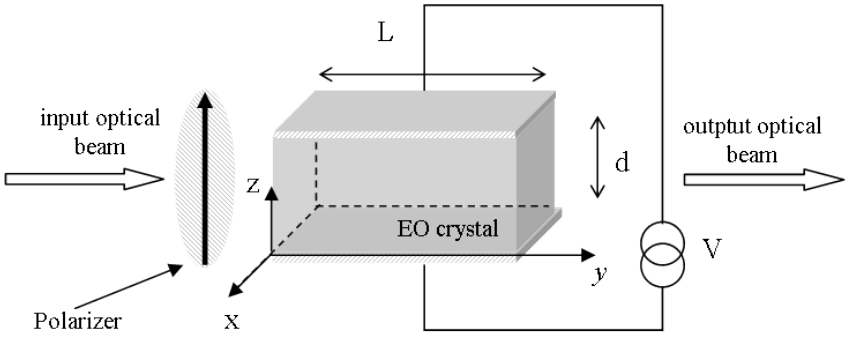

Figure 1.3: Transverse EO Modulator Schematic

the half-wave voltage with is given by, [3]:

$$V_\pi = \frac{\lambda_o d}{r_{33} n_e^3 L} \tag{1.8}$$

where L and d are the length and the distance between the electrodes, respectively. In this case, V_π depends on the length of the electrodes. This features, in addition to other advantages of transverse modulators [3], is particularly attrac-

tive as it provides a further parameter to reduce the half-wave voltage. Therefore, typically transverse EO modulator are preferred to longitudinal ones.

There are two categories of transverse EO modulators: lumped modulators and travelling wave (TW) modulators. Lumped modulators have active length much shorter than the wavelength of the modulating field in the crystal, so that it is possible to assume that the applied voltage is practically constant along the electrodes. Accordingly, lumped modulators present a drop of performances as the frequency increases. Indeed, by enforcing in eq. 1.7 that L, the active length of the modulator, to be equal to the tenth part of the minimum wavelength (in the crystal) of the microwave signal, say $\lambda_{rf}^{min}/10$, we achieve:

$$L = \lambda_{rf}^{min}/10 \Rightarrow V_\pi \propto \frac{10d\lambda_o}{\lambda_{rf}^{min}} \propto \frac{d\lambda_o}{\lambda_{rf}^{min}} \tag{1.9}$$

On the other hand, TW modulators have active length of several wavelength of the modulating field. In this case, the modulator is typically a device realised in integrated optics technology and the electrodes structure is a real Transmission Line (TL) [28], printed on and terminated on a matched load, so that no standing wave can arise. A simple schematic of the TW EO modulator is depicted in Fig. 1.4. The transmission line is properly designed to achieve a *phase velocity*

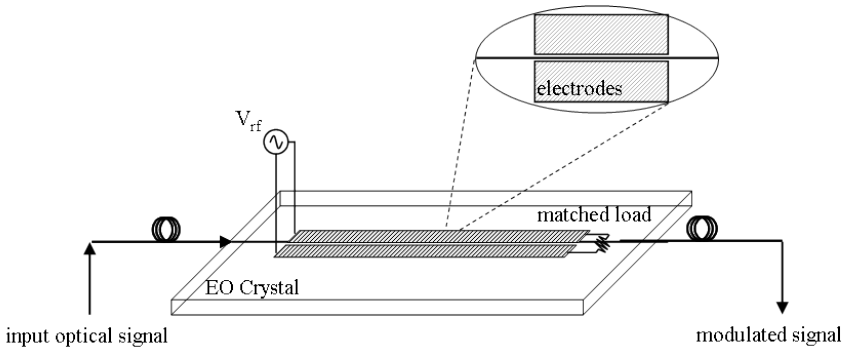

Figure 1.4: Travelling wave EO modulation scheme

matching condition[29]: the phase velocity of the microwave signal is tuned to be identical to that of the optical signal. This allows to the optical wave front to be conditioned by the same voltage during all the propagation in the overall active region, despite of its length.

1.2.3 Amplitude EO Modulators

Despite of the kind of EO modulator, it is possible to introduce proper components in the optical circuit to convert the phase modulation in amplitude one. A commonly adopted solution, especially for transverse EO modulator in integrated optics, is to use a Mach-Zehnder Interferometer (MZI) [3] that, by means of the interference phenomena, transforms the phase modulation in an amplitude one. The MZI is schematically depicted in Fig 1.5. The optical in-

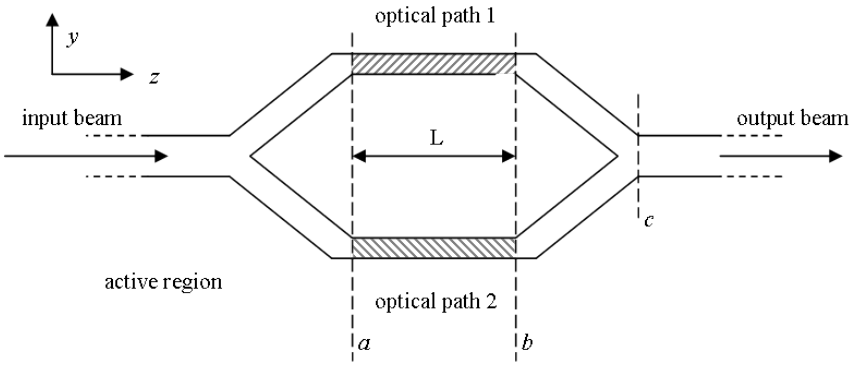

Figure 1.5: Mach-Zehnder Interferometer Schematic

put power is equally divided in the two arms of the interferometer by means of a first Y-junction [29]. Then, the two attained signal experience two different optical path, and at last by means of a second Y-junction they recombine interfering.

Let us now point out the relationship between the phase shift of the optical signals in the two arms of the MZI and the amplitude of the output beam. For sake of simplicity let us assume that the optical beam is linearly polarized and that the power of the input optical beam, say I_{in}, is equal to $2A^2$. At section (a) of the MZI (see Fig. 1.5) the optical fields in the arms of the interferometer are in phase, and are given by:

$$\begin{cases} \boldsymbol{E}_1|_{(a)} = E_1(z)|z = a = A\boldsymbol{i} \\ \boldsymbol{E}_2|_{(a)} = E_2(z)|z = a = A\boldsymbol{i} \end{cases} \tag{1.10}$$

where $\hat{E}_i,\ i = 1, 2$ is the optical electric field in the i-th arm of the MZI and $\boldsymbol{i}$ is the unity vector that identifies the field polarization direction. At section (b) the two optical signal have accumulated a phase difference, say $\Delta\phi$, due to the

asymmetry in the optical paths:

$$\begin{cases} \boldsymbol{E}_1|(b) = \boldsymbol{E}_1(z)|z = b = Ae^{j\Delta\phi}\boldsymbol{i} \\ \boldsymbol{E}_2|(b) = \boldsymbol{E}_2(z)|z = b = A\boldsymbol{i} \end{cases} \tag{1.11}$$

Then the output optical power at section (c), say I_{out} is given gy:

$$\begin{aligned} I_{out} &\propto |E_1|_{(b)} + E_2|_{(b)}|^2 = A^2|1 + e^{j\cdot\Delta\phi}|^2 = A^2|e^{-j\frac{\Delta\phi}{2}} + e^{j\cdot\frac{\Delta\phi}{2}}|^2 = \\ &= A^2\cos^2(\frac{\Delta\phi}{2}) \Rightarrow \frac{I_{out}}{I_{in}} = \cos^2\frac{\Delta\phi}{2} \end{aligned} \tag{1.12}$$

The *transmission factor*, say T, of a MZI is defined as the ratio between output and input optical power [3], and is given by eq. 1.13:

$$T = \frac{I_{out}}{I_{in}} \tag{1.13}$$

. It results that T is non-linear and its graph is depicted in Fig. 1.6. By

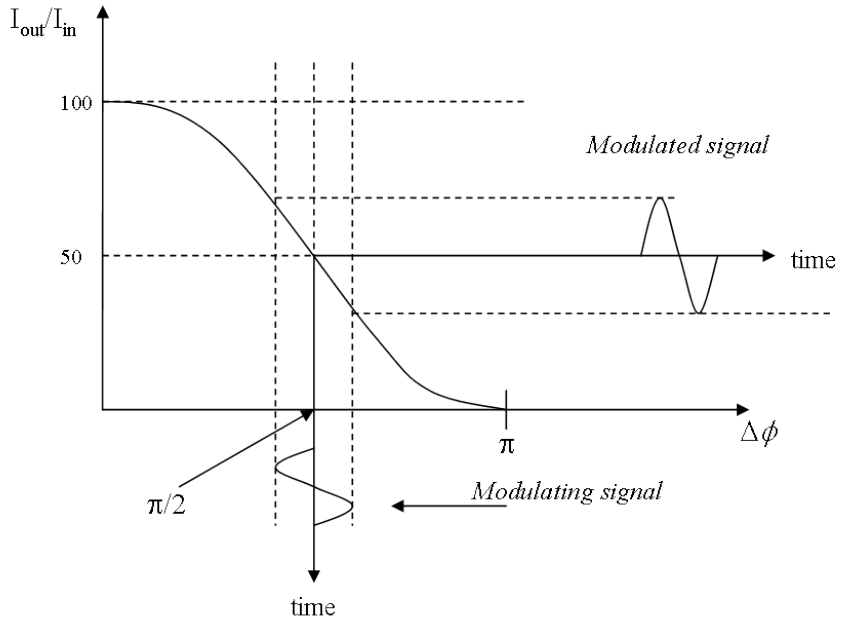

Figure 1.6: Mach-Zehnder Transmission Factor

assuming that the phase shift of the modulated signal is sufficiently small it is possible to linearise the above characteristic around a working point. The optimal choice for the working point is $\pi/2$ as the transmission factor provides a more linear characteristic and also the highest gain around such point [3]. Hence, by linearisation around $\phi_0 = \pi/2$ it results:

$$\begin{cases} \Delta\phi = \phi_0 + \Delta\phi' \\ \phi_0 = \pi/2 \\ \Delta\phi' \ll \phi_0 \end{cases} \tag{1.14}$$

$$T = \frac{I_{out}}{I_{in}} = \cos^2 \frac{\pi/2 + \Delta\phi'}{2} = \frac{1 + \sin(\Delta\phi')}{2} \cong \frac{1}{2}[1 + \Delta\phi'] \tag{1.15}$$

Therefore, the optical power at the output of the MZI is linearly dependent on the phase shift between the interfering signals. Naturally, a biasing contribution in the phase shift is necessary to obtain the optimal conditions in terms of linearity and gain of the system.

Let us now show how a MZI can be exploited in a EO modulator in order to accomplish an amplitude modulation scheme. We will refer to the TW EO modulator as this is the case of more relevant interest. In Fig. 1.7 the schematic of the device is illustrated. Typically, to introduce the biasing for the MZI a dc

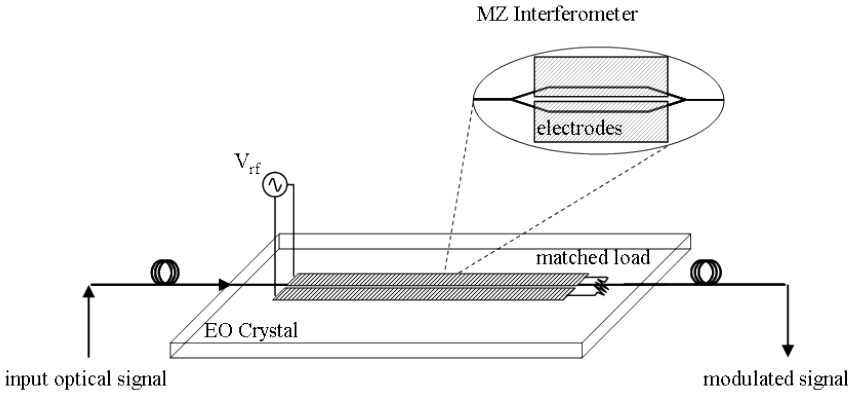

Figure 1.7: Travelling-wave EO amplitude modulation scheme

voltage, say V_0, is applied together with the modulating voltage, say V_m:

$$V = V_0 + V_m; \tag{1.16}$$

As the optimal bias is $\pi/2$, V_0 should be equal to $V_\pi/2$. In this case, eq. 1.15 holds and from eq. 1.6 it results that:

$$\Delta\phi = \frac{\pi}{2} + \pi\frac{V_m}{V_\pi} \Rightarrow \Delta\phi' = \pi\frac{V_m}{V_\pi} \tag{1.17}$$

By substituting eq. 1.17 in eq. 1.15, we obtain the transmission factor of the MZI of the EO TW modulator:

$$T = \frac{1}{2}[1 + \pi\frac{V_m}{V_\pi}] \tag{1.18}$$

By assuming that the EO material is Lithium Niobate we can substitute eq. 1.8 into eq. 1.18 achieving:

$$T = \frac{1}{2}[1 + \pi\frac{V_m}{V_\pi}] = \frac{1}{2}[1 + V_m\pi\frac{r_{33}n_e^3L}{\lambda_o d}] \tag{1.19}$$

where L, the active length, is the length of the arms of MZI.

It's worth noting that the above reasoning does not depend to the assumption of a TW modulator configuration. Hence, the same results, and in particular eq. 1.19, holds also for lumped transverse EO amplitude modulator.

1.2.4 Frequency Limits in EO Modulation

An important aspect of EO modulation concerns its operating frequency limits. Indeed, depending on the kind (lumped or TW) of the considered EO modulator, the operative bandwidth can be significantly different, therefore, a separate discussion is required to enlighten the frequency limits of lumped and TW modulator.

Let us refer first to the lumped modulator. As electrodes length is much lower that the wavelength in the EO material the EO device can be schematically modelled as an RC lumped circuit [3], that is shown in Fig. 1.8. The resistance R_m accounts for Ohmic losses due to electric conduction, the capacitance C_m accounts for the capacitive effect of parallel plate electrodes and at last resistance R_{int} accounts for the internal resistance of the signal generator of voltage V. As known, considering as output the actual modulating voltage, say V_m, the circuit transfer function, say $H(\omega)$, is given by:

$$H(\omega) = \frac{V_m(\omega)}{V} = \frac{1}{1 + j\omega C_m(R_m + R_{int})} \tag{1.20}$$

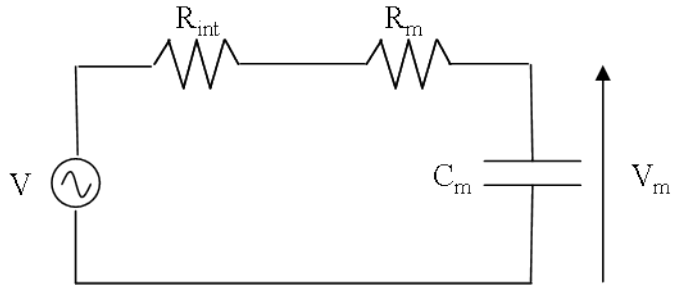

Figure 1.8: Circuital model of lumped EO modulators

Hence, the EO modulator acts as a low pass filter whose $3dB$ cut-off frequency, say f_{3dB}, is given by:

$$f_{3dB} = \frac{1}{2\pi C(R_{int} + R_m)} \tag{1.21}$$

It's worth noting that typically $R_m \ll R_{int}$, therefore modulator resistance can be neglected. Hence, the bandwidth of a lumped EO modulator, say B, is given by:

$$B = [0, \frac{1}{2\pi C(R_{int} + R_m)}] \cong [0, \frac{1}{2\pi C R_{int}}] \tag{1.22}$$

On the other side, TW EO modulators can be represented by a TL, terminated on a matched load, where the phase velocity match condition is ensured. In Fig. 1.9 the schematic of a TW modulator is illustrated. Accordingly, its

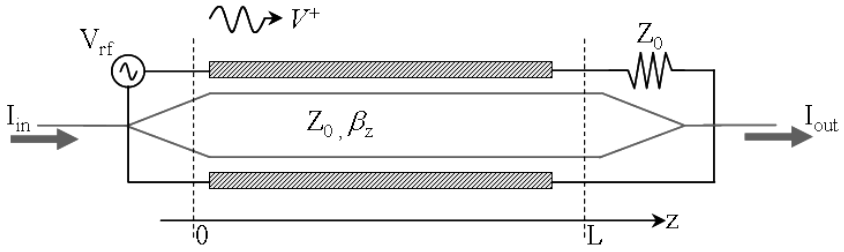

Figure 1.9: Circuital model of TW EO modulators

bandwidth is essentially related to portion of the TL bandwidth, where the

phase velocity matching condition is ensured. Indeed, the dispersion phenomena of the TL can reduce frequency range, where the phase velocity match is ensured. The bandwidth is then strongly dependent on the specific material properties and the geometrical parameters of the considered TW modulator. However, typically, the bandwidth of a TW modulator is much wider than a lumped one. In the case of $LiNbO_3$ TW modulators in integrated optics bandwidth generally exceeds $10GHz$ and can extend up to $40GHz$.

1.2.5 Parameters of EO Amplitude Modulation

As pointed out in the previous sections, the parameters that are commonly exploited to evaluate the performances of a EO modulator are:

- The half-wave voltage, V_π
- The operative bandwidth, B

However, the overall performances of a modulation scheme depends on the characteristics of all the devices constituting the optical chain. Indeed, optical power sources, optical amplifiers, fiber connections, insertion losses and photo-detectors contribute significantly to the characteristics of the signal to be demodulated. A typical EO amplitude modulation scheme is depicted in Fig. 1.10, where I_{in} and I_{out} are the optical power at the input and output of the EO modulator, respectively, V is the voltage applied to the modulator and V_{out} is the voltage at the output of the photo-detector. The parameter that commonly is used to describe the performance of the overall optical chain is the Signal-to-Noise Ratio (SNR) [27] of the electric signal at the input of the demodulation stage. By exploiting eqs. 1.16 and 1.17, it is possible to evaluate the power of the component of interest, say S_{out}, of the signal delivered to the demodulation block. Indeed, the V_{out} is given by:

$$V_{out} = \eta \frac{I_{in}}{2}[\Delta\phi] = \eta \frac{I_{in}}{2}[1 + \pi \frac{V_m}{V_\pi}] \tag{1.23}$$

where η is the photo detector efficiency. Hence, the power of the signal component of interest in V_{out} is given by:

$$S_{out} = \eta I_{in}(\pi \frac{V_m}{V_\pi})^2 \tag{1.24}$$

Concerning the noise power, we can consider only the photo-detector as

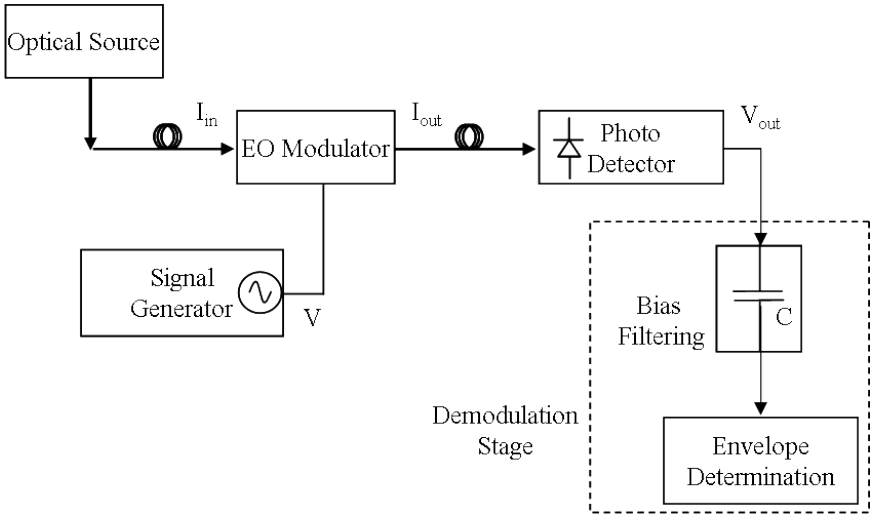

Figure 1.10: Optical chain in EO amplitude modulation

other devices of the chain introduce a negligible contribution if compared. Hence, when a shot noise limited photo-detector is exploited [27], the noise power at the input of the demodulation stage is given by:

$$N = 2\pi h f_c B \tag{1.25}$$

where h is the Plank's constant, f_c is the frequency of the optical carrier, B is the bandwidth of the signal. Concluding, the SNR at the output of the optical detector is given by:

$$SNR \doteq \frac{S}{N} = \frac{\eta I_{in} (\pi \frac{V_m}{V_\pi})^2}{2\pi h f_c B} \tag{1.26}$$

1.3 E-Field Sensor with $LiNbO_3$ optical modulator

The EO probe configuration proposed by Kuwabara et al. in [20] represents an answer to the need of a small wide-band electric field sensor for electromagnetic interference (EMI) testing and electromagnetic compatibility (EMC) applications, where the probe typically measures in proximity of the EM source. In particular, by exploiting optical fiber connections it eliminates the perturbing influence of the coaxial cables, necessary to connect the sensor to the rest of the measurement chain in conventional systems.

The probe structure is essentially made of a dipole antenna [30], acting as a signal generator for a lumped EO amplitude modulator, located at its gap. When the antenna is immerse in an electric field, the voltage induced across the gap is applied to the modulator and the electric field strength is obtained by amplitude demodulation of the optical carrier. A schematic of the EO measuring system is presented in Fig. 1.11

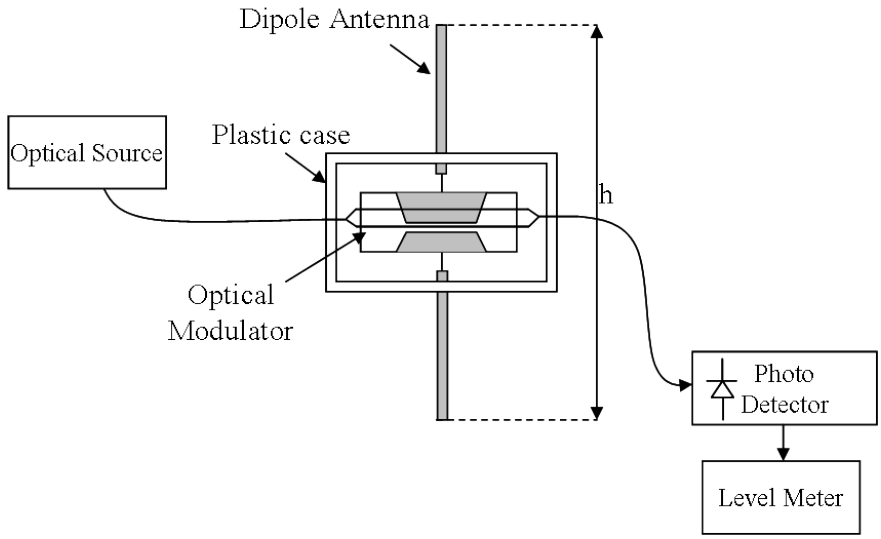

Figure 1.11: E-Field field sensor with a dipole antenna

Most of the sensor materials are non metallic in order to minimize the perturbation introduced in the measurement. Metal-rod elements are $50mm$ long and $4mm$ large in diameter and each one is connected to one electrode of the optical modulator. The overall length of the sensor is $14cm$, including the optical modulator. The optical modulator is based on an integrated MZI realised by means of channel waveguides on a Z-cut $LiNbO_3$ substrate. Only one arm of the interferometer passes through the gap region ($10\mu m$ wide) of the two metal rods for a total active length of $27mm$. This configuration provides a small half-wave voltage ($V_\pi = 4V$). The working point [3] of the MZI is achieved by means of optical biasing: a difference in the optical properties of the channel waveguides provides the bias phase difference of $\pi/2$ in the two interfering optical signal.

The circuital model of the sensor is presented in Fig. 1.12 where $\boldsymbol{h_e}$ is the effective length of the dipole antenna [30], $\boldsymbol{E}$ is the incident unknown elec-

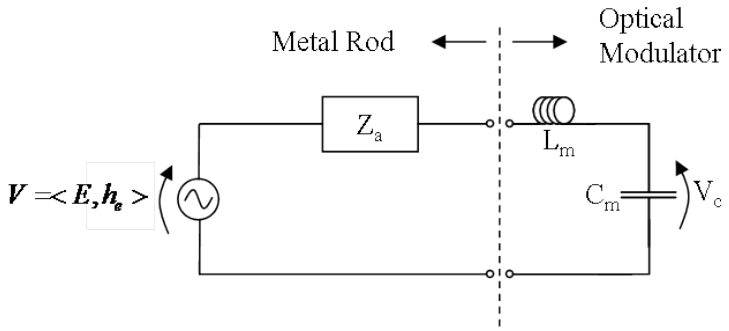

Figure 1.12: E-Field sensor equivalent circuit

tric field, $< \cdot, \cdot >$ indicates the usual scalar product in $\Re^3$, Z_a is the input impedance of the antenna, C_m is the input capacitance of the optical modulator, L_m is the inductance due to metal wire connections between metal rods and electrodes. Then the voltage applied to the optical modulator is given by, [20]:

$$V_c = \frac{E * h_e}{1 + \omega C_m(jZ_a - \omega L_m)} \tag{1.27}$$

where ω is the angular frequency. From eq. 1.23, the output voltage of photo detector is given by:

$$V_{out} = \eta I_{in}[1 + (\pi \frac{V_c}{V_\pi})] \tag{1.28}$$

By substituting 1.27 in 1.28 it is possible to obtain the theoretical response of the EO sensor:

$$V_{out} = \eta I_{in}[1 + (\frac{\pi}{V_\pi} \frac{< \boldsymbol{E}, \boldsymbol{h_e} >}{[1 + \omega C_m(jZ_a - \omega L_m)]} \tag{1.29}$$

A transverse electromagnetic (TEM) cell characterization has been performed by Kuwabara et al. and reported in [20]. In order to experimentally evaluate the frequency response and the sensitivity of the probe, a signal from 35 to $-101dBm$ in the frequency range $[100Hz, 1Ghz]$ has been supplied to the cell. Some of the figures presented in [20] with the comparison of the theoretical model and the experimental results are here reported. In particular, in Fig. 1.13 it is presented the theoretical and experimental relative sensitivity of the probe by the operative frequency, when the power of the optical source is $-11dBm$ and the modulator contacts inductance, L_m is assumed to be $4\mu H$. In Fig. 1.14, the theoretical and experimental optical power output of the sys-

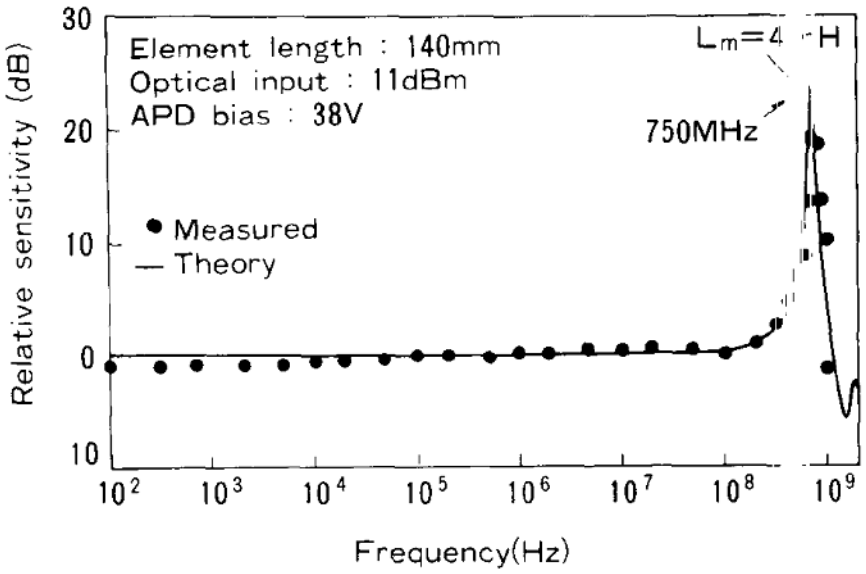

Figure 1.13: Frequency response of the E-Field sensor

tem is presented, at two frequency of interest ($50MHz$ and $750MHz$), as a function of the electrical field strength. Experimental results are in a good agreement with the theoretical model: the sensor exhibits a flat response till $300MHz$, after that the response is dominated by a resonance at $750MHz$, where the sensitivity presents a maximum value. The resonance is due to the resonant behaviour of the dipole antenna. According to [20] the sensor has a large linear dynamic range (about $100dB$), a wide bandwidth (up to $1GHz$) and it is able to detect a minimum field strength of $0.22mV/m$ at $50MHz$ and of $0.079mV/m$ at $750MHz$. Authors claim that the performances of the sensor are compliant with those required in EMC applications.

1.4 Fully Dielectric Sensor

Naghski et Al. in [21] have proposed an EO sensor configuration completely free from metal electrodes. They, indeed, propose a sensor made up only of an integrated MZI, realized on a Lithium Niobate Z-cut substrate. In order to achieve different optical paths in the two interferometer arms, without using metallic parts, a *push-pull* configuration is introduced by means of selec-

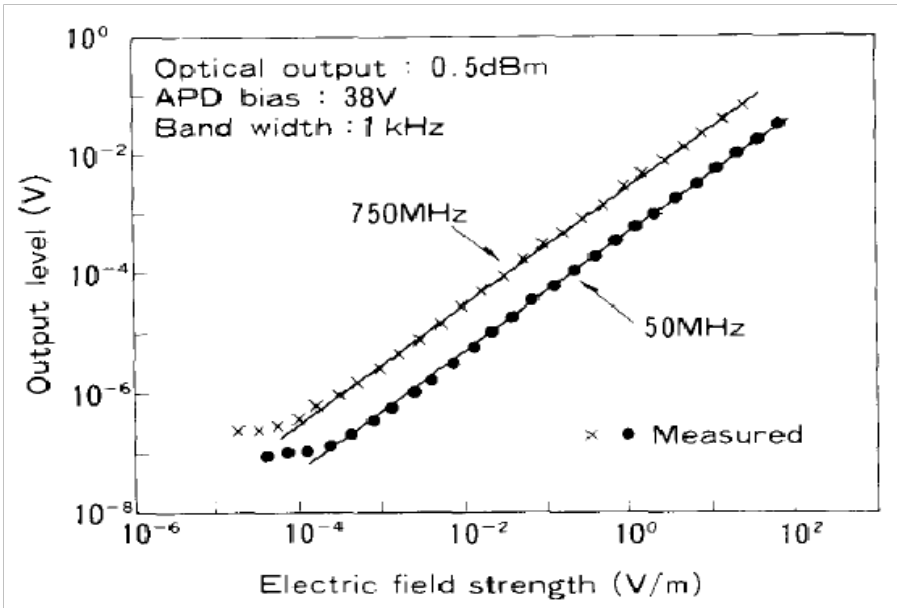

Figure 1.14: Output voltage on the incident electric field intensity

tive *reverse poling* of crystals ferroelectric domain [31, 32]. In Fig. 1.15 the schematic of the sensor is presented. The absence of electrodes can reduce significantly the scattering section [33] of the device, hence the perturbation introduced in the measurement, as well as improve the operational speed of the EO device, since the parasitic capacitances associated to the metallic electrodes are absent. Further, the typical close spacing of electrodes can lead to arcing phenomena that can damage the device, especially when dealing with high intensity fields. Accordingly, the absence of metal enables the probe to be exploited in intense field measurements as well.

In [21] the optical transfer function of the device can be determined:

$$I_{out} = \frac{I_{in}}{2} * (1 - \pi \frac{E_z}{E_\pi}) \tag{1.30}$$

I_{out} and I_{in} are the optical power respectively at the output and the input of the MZI and E_π is the *the half-wave field*, defined from eq. 1.8 as follows:

$$E_\pi = \frac{V_\pi}{d} = \frac{\lambda}{n_e^3 r_{33} E_z L} \tag{1.31}$$

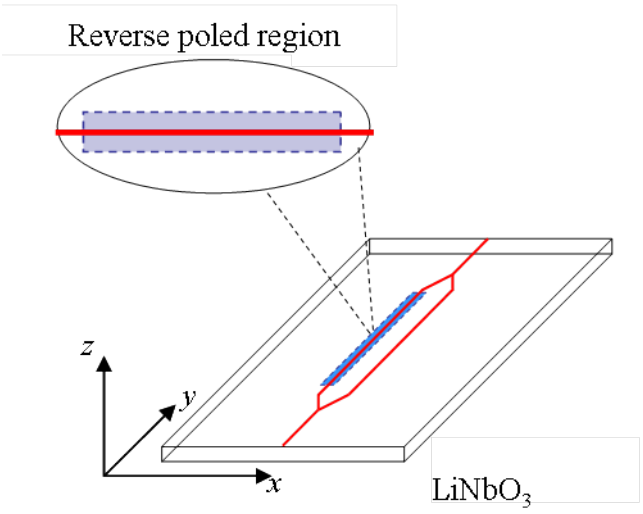

Figure 1.15: Fully dielectric sensor schematic

where r_{33}, n_e, L_r are defined in section 1.2.3 and E_z is the z-component of the uniform incident electromagnetic field.

By characterizing all the equipment of the measurement chain and enforcing SNR $= 1$ (see section 1.2.5) authors estimated the minimum detectable field: $E_{min} = 0.11V/m\sqrt{Hz}$. Further, they assumed that the maximum operative frequency, f_r, is limited only by the *transit time* [3] thus achieving a $f_r \approx 6GHz$.

In [21] it is also also reported the fabrication of the EO sensor. In particular, they realised the optical circuit in $0.5mm$ thick, Z-cut, optically polished, $LiNbO_3$ substrate. The circuit was essentially constituted by a symmetric MZ interferometer with a full branch angle of 1° and a total device length of $30mm$. The straight regions of the arms were $12mm$ long and were spaced 140 μm apart. The channel waveguides, aligned along the y direction, were formed by proton exchange and the reverse-poled region was produced by titanium diffusion [40].

Naghski et al. performed the experimental characterization of the sensor in a TEM cell working up to 1.2 GHz. Experimental results indicated that values of E_{min} and f_r are equal to $0.22V/m\sqrt{Hz}$ and higher than $1GHz$, respectively. Authors addressed the reason of the discrepancy between theoretical and experimental E_{min} to a reduction of the EO coefficient caused by reverse poling and/or field fringing effects due to the electrode geometry.

1.5 E-Field sensor with segmented electrodes

The approach exploited in the EO probe design, presented in section 1.3, has been followed by others authors [8]. Nevertheless, it's worth noting that in that design the electrode capacitance of the modulator increases linearly with the length, therefore long electrodes can lead to high impedance mismatch between the driving antenna and the modulator that reduce the overall performances of the device. Indeed, even if the half-wave voltage of a EO modulator decrease with the active length, C_m increases and accordingly the impedance mismatch reduces the voltage, V_c, applied to the modulator, see Fig. 1.16. Meier et Al. in [17] have proposed an integrated E-field sensor that provide

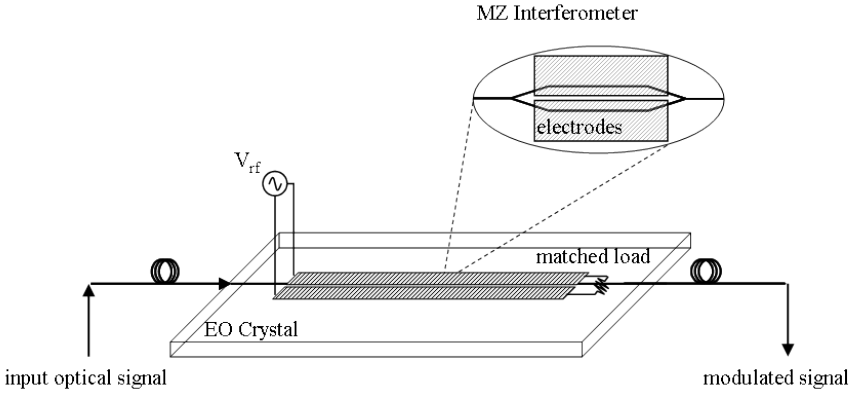

Figure 1.16: Schematic of the E-Field sensor with segmented electrodes

a solution to this problem: the antenna is integrated in a segmented electrode structure. The configuration is schematically depicted in Fig. 1.16. The receiving antenna is deployed and segmented along the optical circuit propagating axis, y, so that it operates as electrodes of the optical circuit. This allows to model the probe with the equivalent electric circuit shown in 1.17. where C_m is the capacitance of the modulator, C_d and R_d are the input capacitance and resistance of the dipole antenna, respectively. Authors retain that due to the short electrical length of the dipole ($\lambda/100$), its impedance can be assumed to be a pure capacitance of about $200pF$, then $C_d \approx 0.2pF$. At the same time, the unsegmented modulator can be modelled as a pure capacitance load of $20pF$, then $C_l = 20pF$. By segmentation, the equivalent capacitance of the

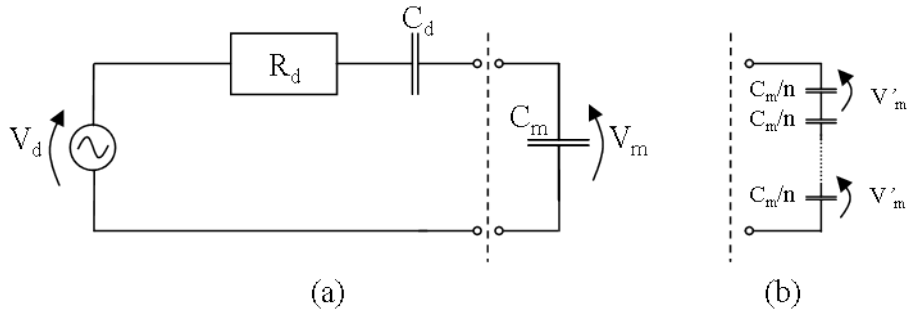

Figure 1.17: Circuital model of the E-Field sensor: unsegmented (a) and segmented (b) electrodes

modulator is given by:

$$C_{eq} = \frac{n^n}{C^{n-1}} \tag{1.32}$$

where n is the number of segment. It's straightforward that n can be chosen in order to optimize the ratio of voltages applied to the unsegmented and the segmented modulators, respectively V_m and V'_m. Indeed, in [17] it is shown that the optimum value of segmentation,n_{opt} is:

$$n_{opt} = \sqrt{\frac{C_m}{C_d}} \Rightarrow (\frac{V'_m}{V_m})_{opt} = \frac{1 + N^2_{opt}}{2n_{opt}} \tag{1.33}$$

Accordingly, Meier et al. concluded that the electrode segmentation is useful when large modulator electrodes are coupled with short dipole antenna or in general when large ratio C_m/C_d are concerned. For experimental verification the Authors examined several field probes with segmentations of $1 < n < 70$. These devices were fabricated on X-cut, Y-propagating $LiNbO_3$ substrates with a size of $30mm$x$3mm$x$2mm$ and had a modulator electrode length of $20mm$. The overall dipole length was set equal to the substrate length of $30mm$, according to 1.16. The sensitivity improvement due to segmentation is shown in Fig. 1.18 as a function of the number of segments. The optimal segmentation level is $n = 12$ and the relative improvement of the probe sensitivity is about $16.5dB$ with respect to unsegmented probe. The dipole capacitance were determined in $C_d = 0.158pF$ by a curve fitting method with the experimental data points.

The frequency response of the probe were measurements using a TEM cell

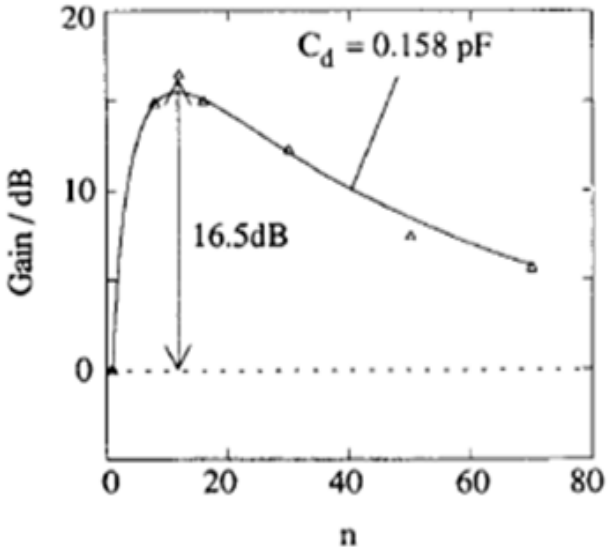

Figure 1.18: Probe sensitivity gain on the electrode segmentation level

and a LPD (logarithmic period dipole) antenna for the upper frequency range and were limited by the optical receiver to $f < 4GHz$. The experimental result showed that the overall system has a flat response up to $3GHz$ and a sensitivity, E_{min}, at $f = 100MHz$ of a $1mV/\sqrt{Hz}$, when the optical source power is $1mW$.

1.6 Bulk EO sensor in Cadmium Telluride

Recently, Togo et Al. in [10] have presented a photonic electromagnetic field sensor, based on a bulk Cadmium Telluride [3], able to operate up to the millimetre bandwidth. The operating principle of the EO probe is schematically depicted in Fig 1.19. The probe is made up of two polarizing-beam splitters (PBSs), a quarter-wavelength plate (QWP), a Faraday rotator (FR) and an EO crystal of Cadmium Telluride (CdTe) with an optical reflecting coating on the. The optical pulses delivered by a polarization maintaining fiber (PMF) are collimated and propagate toward the EO crystal, where due to the transient EM field a polarization modulation is accomplished and the optical pulses are reflected back by the mirror. In particular, the EO crystal is properly oriented in order that optical pulses propagates along the (110) crystallographic direction

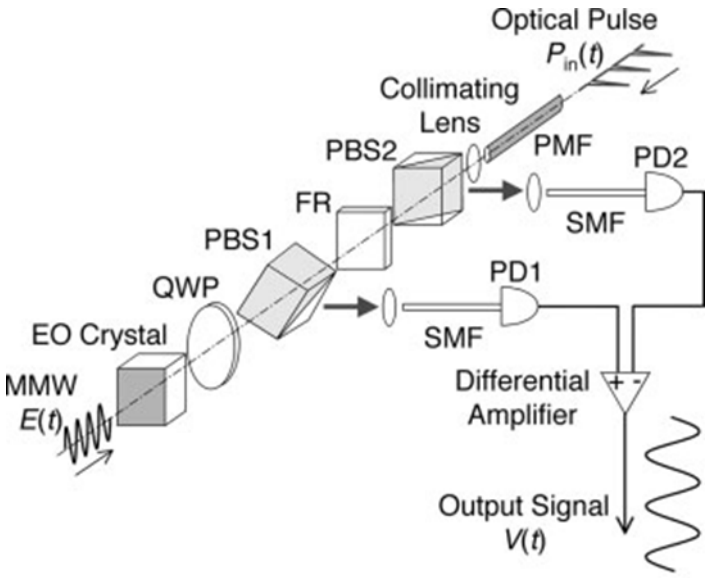

Figure 1.19: Schematic of the EO sensor

[3] and the EM field component parallel to the (001) crystallographic direction induces a polarization modulation in the optical signal, see Fig. 1.20. Then, by means of the two PBSs the orthogonal components of the optical pulses are extracted, converted in electrical signal, delivered to a differential amplifier and analysed by conventional measurement instrumentation (oscilloscope and/or spectrum analyser). In [10] it is shown that the electrical voltage

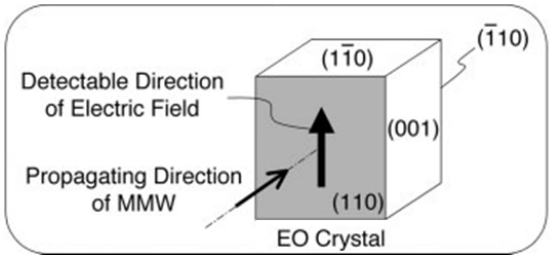

Figure 1.20: Polarization modulation scheme

signals, $P_{out1}(t)$ and $P_{out2}(t)$, at the input of photo detectors PD1 and PD2,

respectively, are given by:

$$P_{out1}(t) = \frac{1}{2}1 + \alpha E(t) * P_{in}(t) \tag{1.34}$$

$$P_{out2}(t) = \frac{1}{2}1 - \alpha E(t) * P_{in}(t) \tag{1.35}$$

$$\alpha = \frac{2\pi l}{\lambda} n^3 r_{41} \tag{1.36}$$

where P_{in}, $E(t)$,l,λ,n and r_{41} are respectively the optical input power, the EM field incident on the device, the length of the crystal, the refractive index, and the electro-optic coefficient. Hence, by means of the differential amplifier, the output voltage signal is made proportional to the EM unknown field.

Togo et Al. employed the EO sensor in the near-field measurement of

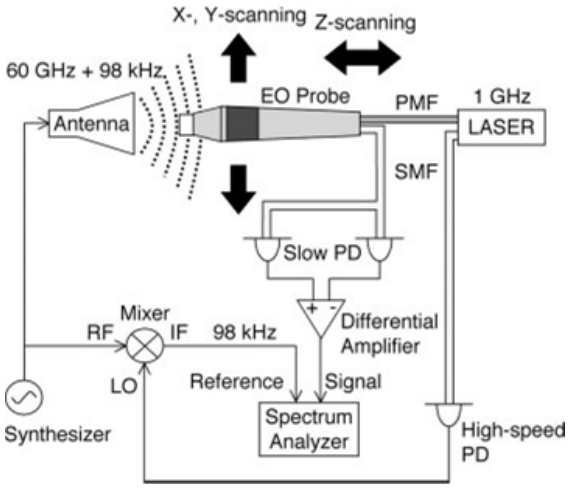

Figure 1.21: Measurement set-up

a millimetre wave antenna. In particular, they mapped the field radiated at 1λ from the aperture by a standard gain horn (SGH) antenna, operating at $60GHz$, by means of the photonic measurement system depicted. They also compared experimental results with the numerical result attained by a commercial software simulator, based on FEM method [34]. A selection of the comparative results presented in [10] is here reported. In Fig. 1.22 and 1.23 H-plane and E-plane of the antenna near field mapping are reported, respectively. A good agreement between experimental and numerical results are obtained in the H plane, as shown in Fig. 1.22. Instead Fig. 1.23 shows that in the E-plane there

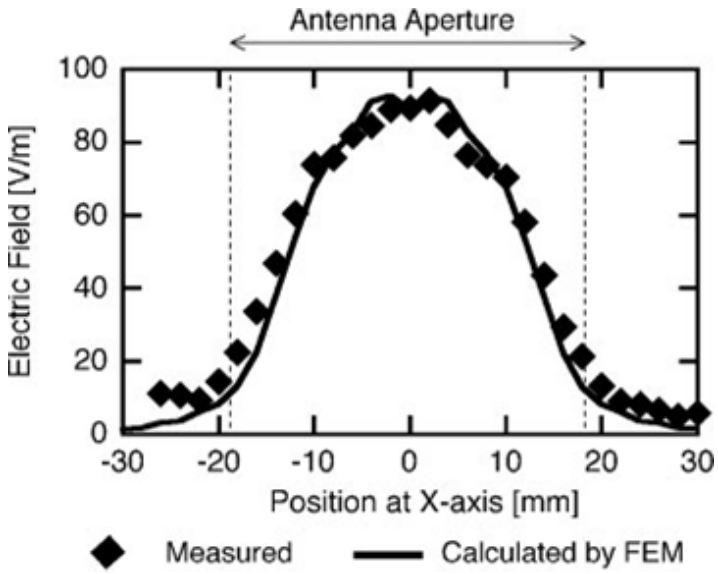

Figure 1.22: SGH near field mapping: H-plane

is a slight difference between measured and calculated data. The authors addressed this difference to the spatial resolution of the EO probe, that is limited by the size of the optical-beam spot in the EO crystal.

In [10] Authors claims that the developed EO probe is able to detect a minimum electric field value of less than $1V/m$ over a bandwidth lager than $150GHz$.

1.7 EO Sensor with a Printed Antenna

The *Electromagnetic Wave Division* of the AIST has been involving in the photonic measurement techniques for a long period [19, 35, 36, 37, 38]. In particular, they developed an EO probe for EM field sensing in integrated optics, based on a Lithium Niobate crystal, and characterized by a printed dipole antenna. This sensor has been successfully employed in the NF experimental characterization of antennas [19]. The probe structure is schematically depicted in Fig. 1.24. The device is made of a X-cut $LiNbO_3$ substrate, whose dimensions are $13mmx3mmx0.5mm$, where a printed triangular dipole antenna has been printed on. The antenna length is about $2.46mm$ and its width at the gap region is about $1.5mm$. A MZI, operating in a reflection fashion,

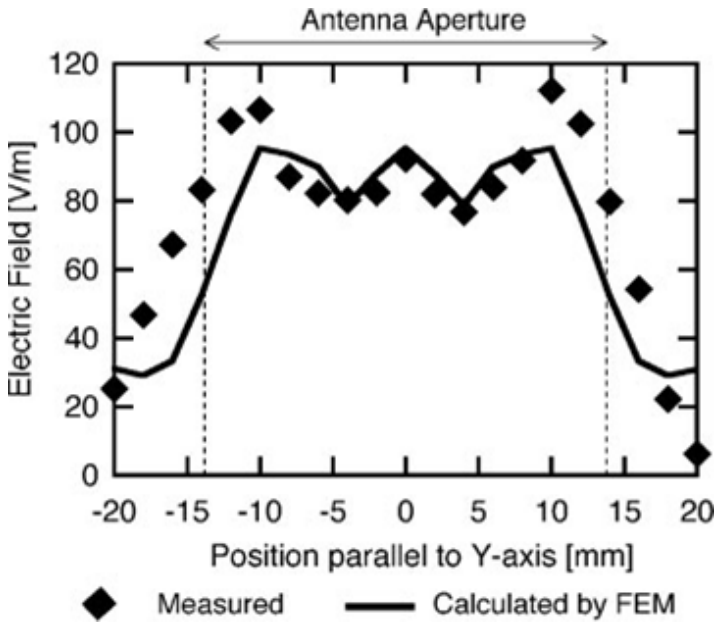

Figure 1.23: SGH near field mapping: E-plane

has been integrated in the device.

The NF experimental characterization of a SGH antenna operating in the X-band has been performed at AIST laboratories by means of the photonic probe. The measurement results have been compared to those ones of standard measurement techniques (OEW probes) and also to the numerical prediction of a MoM commercial software [39]. Some of the results published in [19] are here reported. In particular, in Figs. 1.25 and 1.26 antenna E-plane and H-plane pattern, achieved by OEW are depicted. where k_{xn} and k_{yn} are the the respectively x and y components of the propagation vector, normalized to the wavenumber. The comparison shows that there is a good agreement of experimental results from data collected by the photonic probe and OEW probe.

Recently, at AIST a new small EO sensor, still based on $LiNbO_3$ crystal, has been developed. The new configuration is made of an integrated lumped MZI, operating in a reflection fashion, and a printed dipole antenna array. The antenna array allows to improve the sensibility with respect to the previous configuration as a the effective length of the modulator is longer. The probe is schematically depicted in Fig. 1.27. In particular, the probe structure is made of a $13mmx3mmx0.5mm$ X-cut wafer of Lithium Niobate, where a MZI has

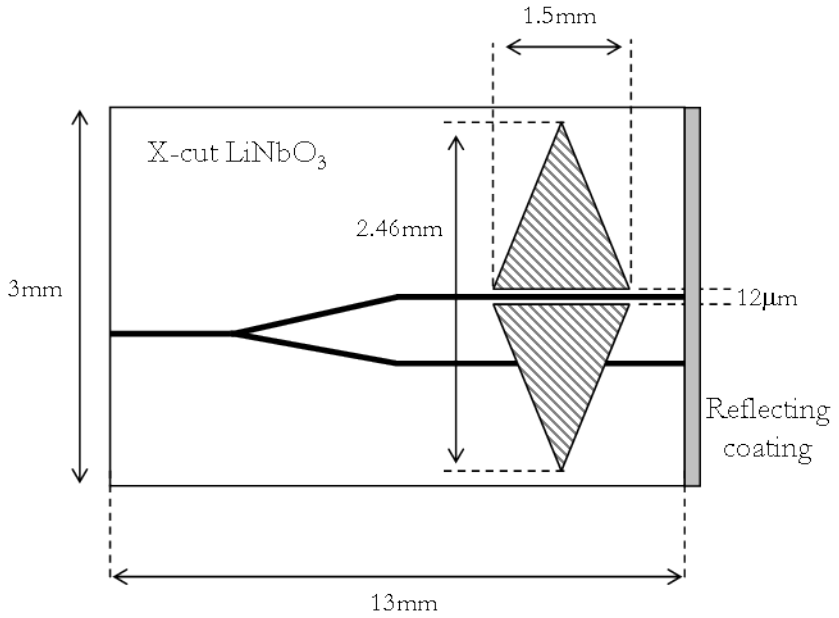

Figure 1.24: Schematic of the EO sensor with a printed antenna

been realised in by means of *TI+ in-diffusion* [40] waveguides. The printed antenna is a passive array of 7 short dipoles, spaced $100\mu m$. Each dipole has a total length of $2.4mm$ and a width of $100\mu m$. Dipole electrodes are separated by a gap region of $12\mu m$. Only one arm of the interferometer passes through the gap region of the array and hence is influenced by EO effect. A reflecting coating, made of a gold thin film, has been realised in order to achieve a MZI in reflection configuration. Concluding, a picture of the actual probe is presented in Fig. 1.28.

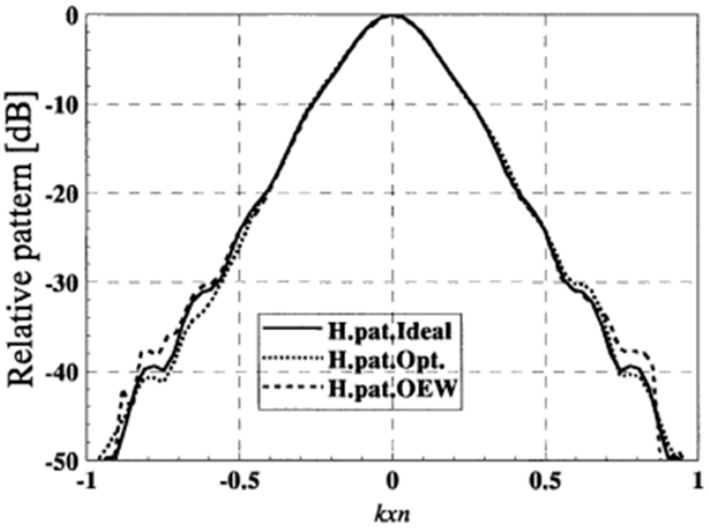

Figure 1.25: Antenna FF pattern: H-plane cut

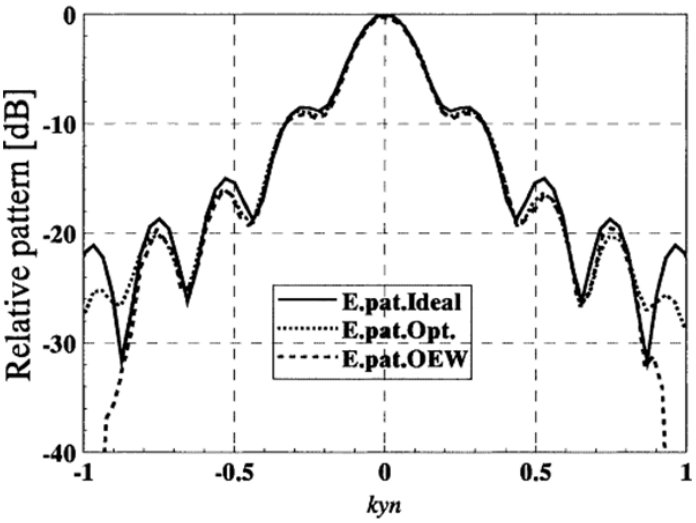

Figure 1.26: Antenna FF pattern: E-plane cut)

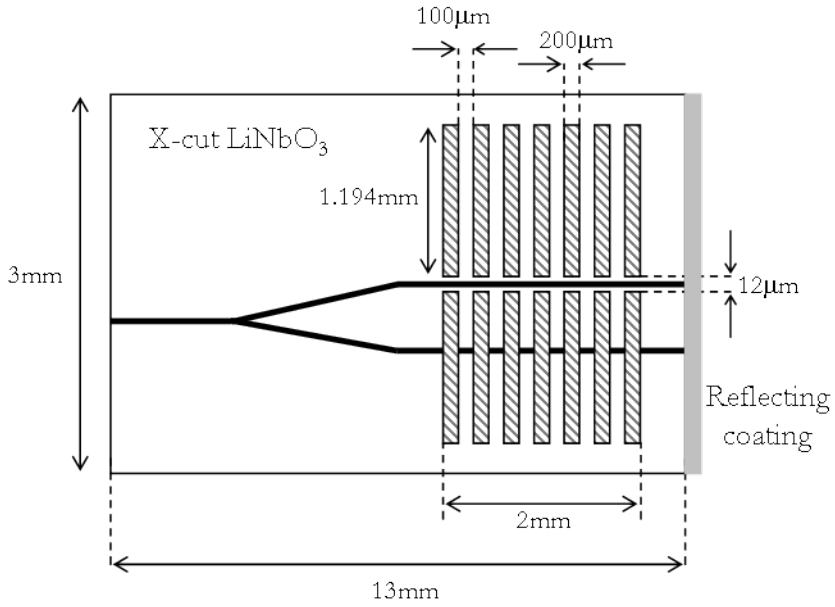

Figure 1.27: Schematic of the EO sensor with a printed antenna array

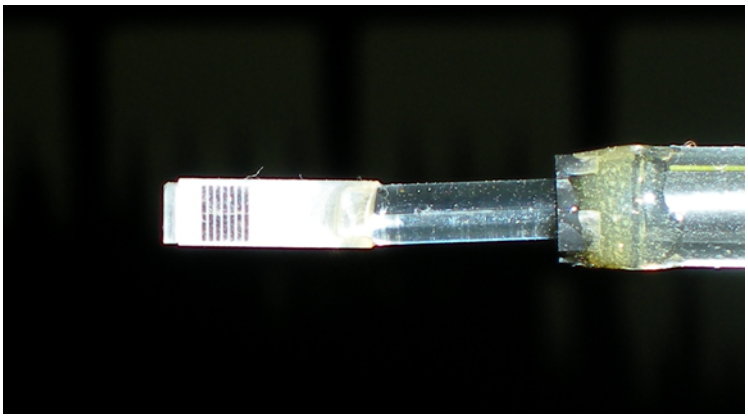

Figure 1.28: Rencently developed EO sensor structure

1.8 Summary of EO sensor characteristics

In this section it is presented a synthetic review of the EOS presented in the chapter. Indeed, in Table 1.8 there are summarized the main features of the above described EOS, in terms of sensitivity (E_{min}), maximum operating frequency (f_{max}) and selectivity toward to the field incident polarization. Concerning this last point, as no information is expressly indicated in the open literature, we estimate of the behaviour has been done on the basis of the sensor topology. In particular, we referred as *high* selectivity to those configurations where metallic elements or eventually an antenna selects the component of the impinging field that contribute to EO modulation. Conversely, we referred as *low* selectivity to configurations, where a proper orientation of the probe is required to achieve effective EO modulation of the optical signal.

Probe	E_{min}	f_{max}	Selectivity
Metal Rods Sensor	$0.079mV/m$	$1GHz$	High
Fully Dielectric Probe	$0.22V/m/\sqrt{Hz}$	$\geq 1GHz$	Low
Segmented Electrodes Sensor	$1mV/\sqrt{Hz}$	$\leq 4GHz$	High
Bulk Sensor	$< 1V/m$	$150GHz$	Low
Printed Antenna Sensor	n.a.	$10GHz$	High

Table 1.1: Summary of EOS main features

Chapter 2

Travelling Wave Electro-Optic Electromagnetic Field Sensor Design

The use of conventional metallic probes in NF antenna characterization makes the choice of the position and the shape of the acquisition surface strictly limited by and determined by the correct trade-off, involving:

- the time-stability of the measurements
- the accuracy of measurement
- the accuracy of FF estimation
- the available facilities
- the operating costs

Indeed, unavoidable mutual coupling effects between probe and AUT as well as perturbations introduced by the linking coaxial cables can become significant, if the acquisition surface is not enough far apart from the radiation source. Accordingly, a limitation on the minimum distance between the metallic probe and the AUT arises: typically NF measurements distances are larger than six wavelengths. At the same time, given the truncation error, larger distances imply wider acquisition surfaces and consequently higher scanning times. Hence, enlarging the distance between the measurement surface and the AUT generally requires facilities with larger dimensions, higher scanning times, more

stable apparatus and higher operative costs. Limitations coming from conventional probes have pushed the research to investigate on alternative solutions for the radio-wave signal measurements. Optical techniques have been increasingly considered as a valid alternative because of the low invasiveness, the large bandwidth, the high immunity to noise and interferences. In particular, as pointed out in 1, EO sensing has been recognized as the most promising approach [14] for the radio-wave signal measurements and some EO probes prototypes, based on different materials and different technologies, have been developed and experimentally tested.

Notwithstanding the remarkable results already achieved, the use of EO field sensors, especially in NF antenna characterization, should be considered at the moment in a prototyping stage and it does not find application in commercial scanning systems, remaining up to now still a border solution implemented for experimental purposes. This is essentially due to the reduced sensitiveness in terms of minimum detectable electric field intensity and the low polarization isolation that photonic probe prototypes generally ascribed to EOS if compared with conventional OEW probes.

As mentioned in the Introduction the aim of the research activity on this topic during the three years Ph.D. course has been to develop an innovative Near-Field antenna characterization system able to overcome the limitations of existing systems, considering the most innovative solutions ever proposed in this application area. During the Ph.D. course, part of the research activities has been focused on the design of a photonic field probe for NF antenna characterization, based naturally on EO effect, able to provide sensitivity and polarization isolation adequate for the purpose application. Different EO probe configurations, each one with peculiar characteristics, have been designed and numerically tested: starting from the less invasive structure, more complex solutions have been considered to satisfy all the above requirements. The research activity leaded to the project of an innovative EO probe topology, where for the first time a Mach-Zehnder interferometer in travelling-wave configuration has been considered. This solution, indeed, allows improving significantly the sensitivity and the operative bandwidth of the sensor.

In this chapter it is described the research activity accomplished and the final probe design. The most relevant photonic probe configurations that have been analysed will be first presented in the next sections, poitining out advantages and drawbacks, in order to better enlighten the design criteria which have determined the final configuration.

2.1 Requirements and Guidelines for the EO Field Probe Design

The choice of exploiting EO effect lead naturally to the use of Lithium Niobate as EO material. Indeed, this crystal is widely considered, especially in integrated optics, not only for its remarkable EO effect, but also for it relatively easy fabrication and its well established optical circuit manufacturing techniques. Crystal's properties have been considered according to the datasheet of Lithium Niobate, produced by Crystal Technologies[122]

The main attractive feature of a EO probe concerns its *non-invasive* behaviour: the perturbation introduced by the probe in the measurement should be negligible. This requirement can be satisfied by a probe with a low scattering section [33] in order to disregard the electromagnetic coupling with the radiation source. Therefore, thanks to the potentiality of achieving small monolithic devices [44], the design of the EO probe should be addressed to solutions in integrated optics. Further, although the exact determination of the invasiveness of a photonic probe would require a complete characterization of a prototype, it is reasonable to assume the absence or eventually the reduced presence of (printed) metallic elements on a electrically small substrate ensures a negligible perturbation. Accordingly, as a design guideline, metal should be properly and providently introduced on the substrate, trying to keep the device free of metallic parts as much as possible.

Even in materials where EO effects is remarkable, such as $LiNbO_3$, the modulation effects on the optical signal are relatively small. Accordingly, EO probes typically present a reduced sensitivity, in terms of minimum detectable field values, say E_{min}. It's worth noting radiated powers in indoor antenna characterization applications are limited: vectorial and scalar network analysers do not provide high power output (rarely they exceed $+20dBm$ in output power). Hence, the electromagnetic field intensity are low, even in NF measurements, and probe sensitivity must be adequate. This does not represent an issue with conventional probes because of their metallic nature, but it can be an issue with EO probes, that forces to introduce multiple both optical and microwave signal amplification stages in the measurement chain (see 4.4) to keep acceptable the SNR level.

Therefore, in order to avoid a more complex and expensive measurement system, adequate EO probe sensitivity is required. In particular, the design goal consists in developing a EO sensor with a sufficient E_{min} to be employed in NF measurements with conventional instrumentation, without multiple am-

plification stages for both the optical and the microwave signal that typically are required. To this end, first an effective EO modulation is mandatory: the proper modulating field distribution has to be induced in the crystal substrate to exploit at best the EO effect.

For sake of simplicity let us consider a reference system $Oxyz$. From now on along this chapter, unless differently indicated, we assume that the coordinate axes of the reference system coincide with the *dielectric axis* of Lithium Niobate [23] with z-axis coincident with the optical axis of the crystal [23].

Optimal conditions to exploit at best the EO effect in Lithium Niobate would require that E_z, is the dominant component of the modulating electric field. Furthermore, it is E_z is needed to be constant along the active region of the integrated MZI. Indeed, although in $LiNbO_3$ all the field components concur to the EO modulation, the E_z component presents a relative EO coefficient, r_{33}, significantly higher than the others [3]. Further, despite of the other components it does not affect axis directions of optical indicatrix [23]. Constant amplitude is required to exploit at the best the overall active length of the interferometer, avoiding averaging effects due to spatial variations [3] that would significantly reduce the overall device sensitivity.

Accomplishing the optimal distribution of the modulating field inside the EO crystal is not enough by itself to ensure that requirements concerning sensitivity are satisfied. Indeed, this condition is only necessary to ensure that the EO modulation is performed in the optimal way, but it does not ensure that the *modulation depth* [24] of the optical carrier is adequate to be detected by conventional instrumentation. Accordingly, probe topology should be properly designed to obtain and also exploit the optimal modulating field distribution to get the desired sensitivity.

Another important aspect in the design of a EO field probe for NF antenna characterization consists in *polarization selectivity*: the capability of the device to isolate the E-field component of interest. It's worth noting that, from the theoretical point of view, the probe *effective length* [30] is not required to satisfy any specific condition and it can be, in principle, arbitrary. Naturally, in this general case a vectorial probe compensation [41] would be always mandatory in order to correctly distinguish the contributions of each component of the unknown field to the modulating field. Therefore, we require the probe to have a total effective length linearly polarized.

The operating frequency bandwidth has been fixed to X-band. But, we retain that the designed solution can be properly and easily scaled to operate in higher frequency ranges up to the millimetre band-width.

Requirement	Description	Design Guideline
Invasiveness	Negligible scattering section	Device free of metal as much as possible
Sensitivity	Minimum Detectable E-Field Value	Optimal distribution of the induced modulating field and proper probe topology
Selectivity	Capability of selecting the polarization of interest of the unknown field	Proper probe topology design
Bandwidth	$[8GHz, 12.5GHz]$ X-band	

Table 2.1: EO Probe Design Requirements and Guidelines

The above considerations, summarised in Tab. 2.1, constitute the requirements and the general guidelines to be pursued when designing a photonic probe.

2.2 Fully Dielectric EO Probe

In order to keep the scattering section as low as possible, following the approach proposed in [20], a probe structure fully dielectric has been first considered. The device is a Lithium Niobate Z-cut substrate, where a integrated MZI in *push-pull* configuration can be realized by means of the selective *reverse poling* of ferroelectric domains [31, 32]. Therefore, it's possible to assume that such a structure has a negligible scattering section as far as its electrical lengths are comparable to some wavelengths in the EO material. The structure has been analysed by means of an Electromagnetic Software Simulator (EmSS), based on Finite Element Method (FEM) [34], able to provide the electromagnetic field distribution inside a preassigned volume. The probe structure is depicted in Fig.2.1, as it appears in the EmSS. In order to determine the behaviour of the structure to a generic excitation, a parametric simulation has been performed. In particular, the electromagnetic field distribution excited inside the crystal by a plane wave, linearly polarized, has been computed when the propagation direction of the wave varies. A complete characterization requires that for each impinging direction two plane waves with orthogonal polarizations. In the EMsS simulation a linear polarization has been

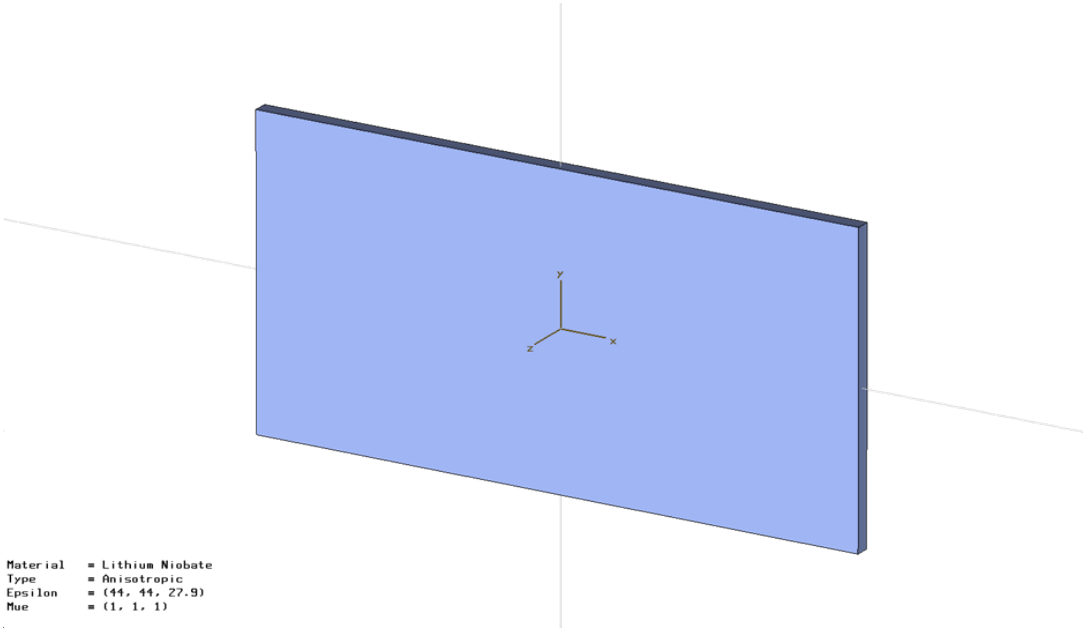

Figure 2.1: EO Probe structure in the EMsS

considered for the excitation wave, therefore the co-polar component has been assumed to have electric field along i_θ, while the cross-polar has been assumed to have electric field along i_ϕ, see Fig. 2.2.

Due to the structure symmetry, it has been sufficient to analyse only the angular sector corresponding to the first octant of the $Oxyz$ space, $\phi \in [0, \pi/2]$ and $\theta \in [0, \pi/2]$. In order to explore completely the range of applicability of such configuration, the simulation frequency interval has been fixed in $[6GHz, 13GHz]$, although the actual interest bandwidth corresponds to the X-band. The amplitude of the electric field of the excitation plane wave has been set to be $1V/m$. An angular sampling step of $\pi/8$ for the excitation impinging direction has been chosen. According to the frequency bandwidth of interest, the substrate dimensions have been fixed in $30mm$x$10mm$x$0.5mm$, in order to contain the probe dimensions comparable to the free space wavelength at the highest frequency.

For the sake of brevity all the numerical results, regarding the field distribution induced inside the EO crystal for each frequency of the band of interest, for each impinging direction of plane wave, for copolar and crosspolar polarization, are not here reported. We report only the result for one representative

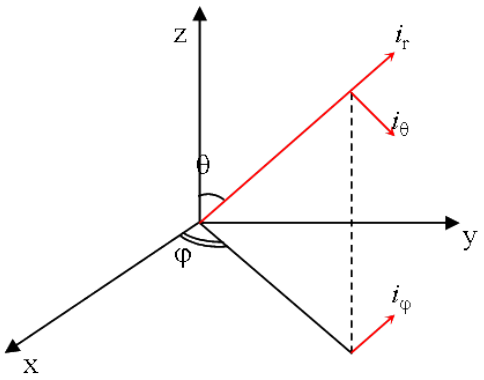

Figure 2.2: Spherical reference system in the EMsS

case as a support to the successive discussion about numerical results. In particular, the copolar plane wave at the frequency of $10GHz$ with propagating direction $\theta = \pi/4$ and $\phi = 0$ has been considered. The plane wave excitation schematics as it appears in the EM software simulator is presented in Fig.2.3 . The field distribution induced in the crystal volume is described by means of 2D contour plots, corresponding to the amplitude of each component on coordinate planes. In particular, three cut planes have been considered: plane $x = 0$, plane $y = 0$ and plane $z = 0.2mm$ (50μ under the crystal surface) in order to analyse the field in the region, where the integrated optical circuit lies. The $|E_z|$ component is presented on the x, y and z cut plane in Fig.2.4-2.6,respectively. In Fig.2.7 and Fig.2.8, $|E_x|$ and $|E_y|$ components are respectively presented in the z cut plane.

Fig.2.7 and Fig.2.8 show that the amplitude of E_x component varies significantly inside the crystal volume, assuming values comparable to E_z. On the other side, E_y can be neglected in the region of interest inside the crystal (the central region). For sake of brevity, other cut-planes for $|E_x|$ and $|E_z|$ components are omitted as they do not contribute significantly to the knowledge of the field distribution. For the particular case, numerical results point out that the electric field induced inside the crystal is significantly oscillating and essentially given by the E_x and E_z components.

The full numerical analysis leads essentially to the same conclusion of the considered case, above discussed, especially when dealing with frequencies in the interval $[6GHz, 8GHz]$. Hence, the considered structure presents an induced field distribution spatially variable and strongly dependent by the im-

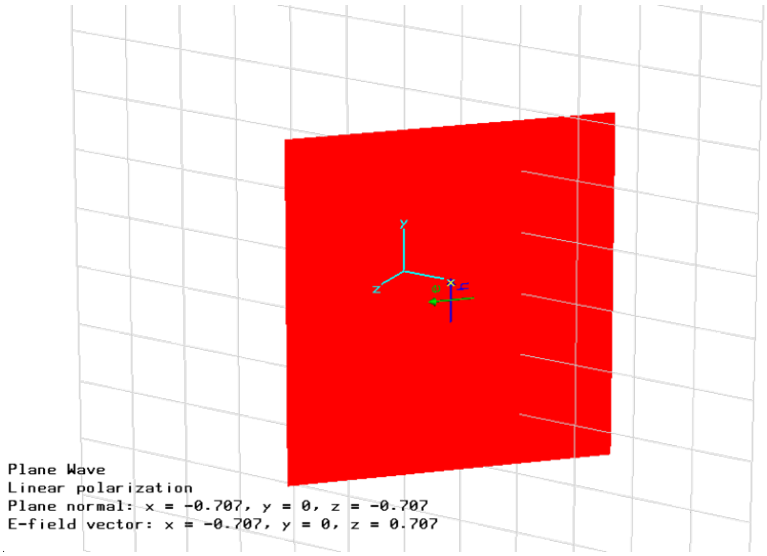

Figure 2.3: Spherical reference system in the EMsS

pinging wave direction, the operative frequency and the polarization of the excitation wave. In addition, it's worth noting that the intensity of the induced modulating field achieves small values, typically comparable with the amplitude of the applied excitation. Therefore, this configuration does not provide the optimal conditions for EO modulation.

Notwithstanding it is not possible to evaluate the final device performances only from numerical results, it is realistic to estimate that they will be reduced, in terms of both sensitivity and selectivity towards the impinging polarization. Therefore, the considered configuration is not adequate to all those applications where field amplitude levels are low and field spatial distribution is unknown. However, it's worth noting that such a dielectric probe present a low scattering section, and this feature makes it attractive in all those applications where radiated power are significant and, moreover, polarization of the field under measure is *a-priori* known. For instance, one of these applications can be failures diagnosis of radiating elements in radar systems, where typically radiated power are elevated and aperture field distribution inside the radiating elements is known [42]. Therefore, the development of a prototype of a fully dielectric sensor has been the aim of a collaboration between the *Dipartimento di Ingegneria Biomedica Elettronica E Telecomunicazioni* (DIBET) of *Università di Napoli Federico II*, Naples, Italy, and the *Dipartimento di Ingegneria*

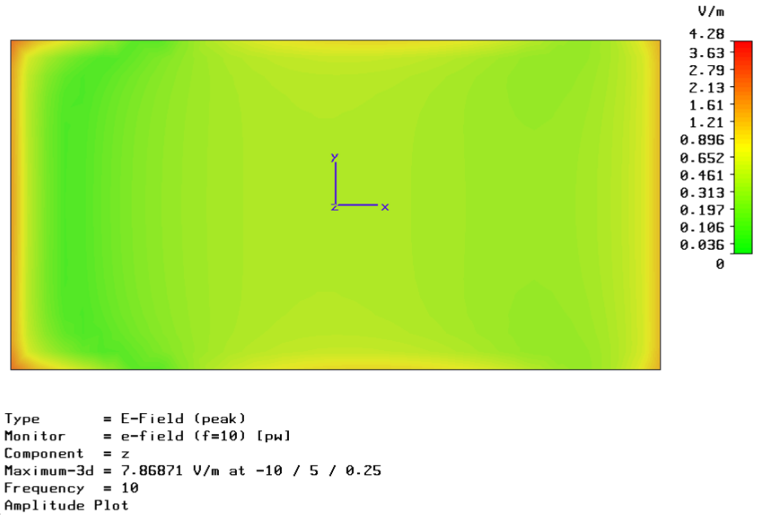

Figure 2.4: $|E_z|$ in the z-cut plane

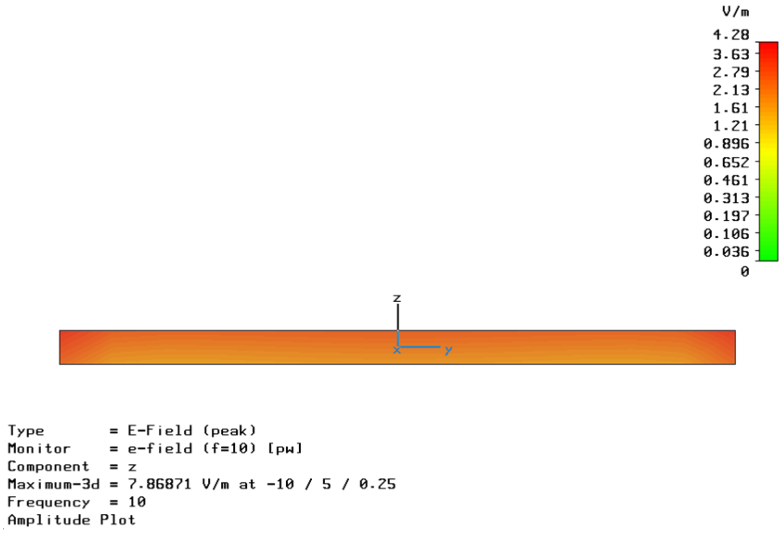

Figure 2.5: $|E_z|$ in the y-cut plane

Elettronica ed Elettrotecnica (DEE) of *Politecnico di Bari*, Bari, Italy, and the *Centro per la Ricerca Elettronica in Sicilia* (CRES), Palermo, Italy [121].

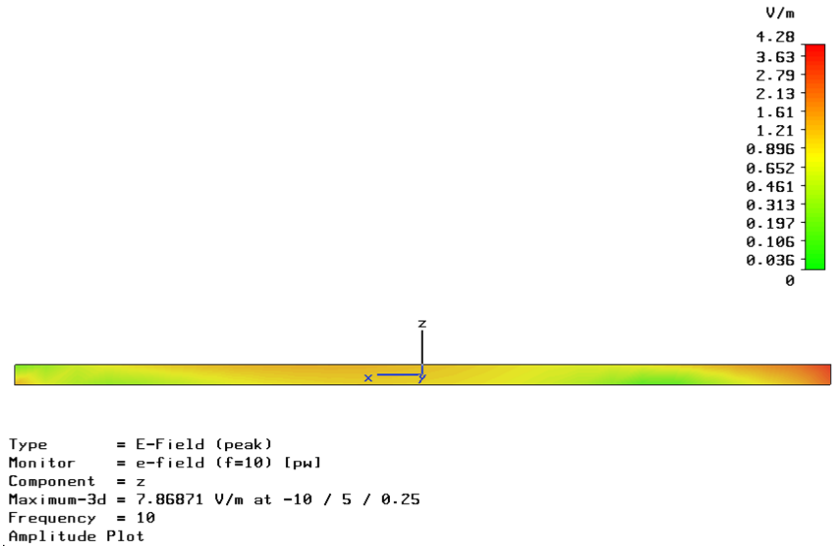

Figure 2.6: $|E_z|$ in the x-cut plane

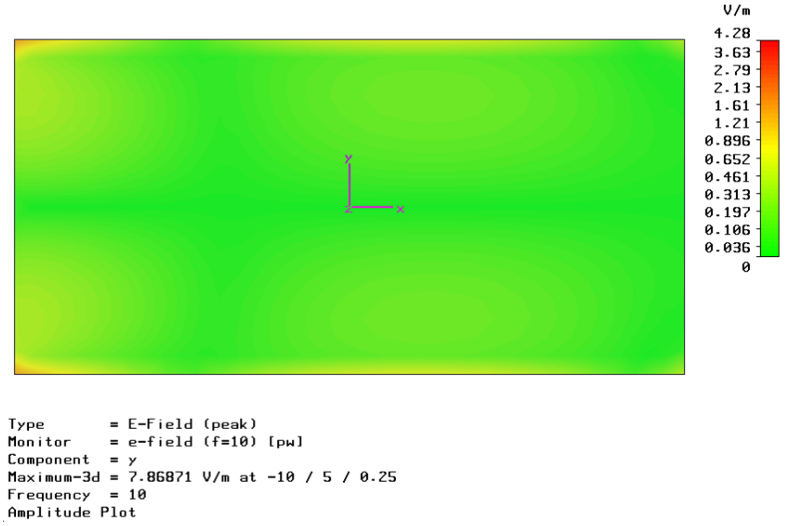

Figure 2.7: $|E_x|$ in the z-cut plane

2.3 Dielectric Resonator Probe

The strong dependence of the field distribution, induced inside the completely dielectric probe, on the excitation characteristics does not provide the condi-

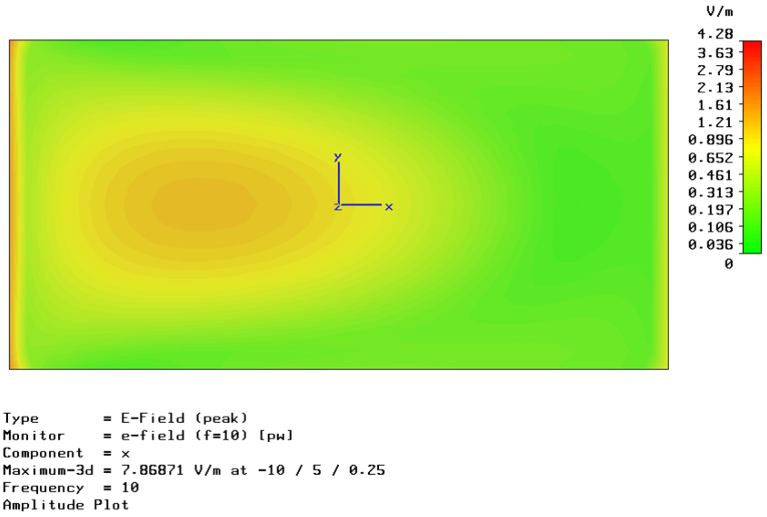

Figure 2.8: $|E_y|$ in the z-cut plan

tions to correctly exploit the EO effect for the modulation. The variability of the spatial distribution of the modulating field on the frequency, the polarization and the propagation direction of the excitation wave make complex the relationship between the optical signal intensity and the amplitude of the modulating field, so that the performance of EO modulation depends strongly on the actual working conditions.

As pointed out in section 2.1, ideal conditions to EO modulation would require that, despite of the operating frequency and the characteristics of the excitation, the modulating field is constant in the active region of the MZI and essentially polarized along the z-axis direction. Such characteristics remind to typical field distributions of resonant structures [43]. Therefore, a dielectric resonator configuration has been considered to realise the EO probe.

The structure is made of a cylinder of radius $a = 3cm$ of homogeneous dielectric material, whose basis have been loaded with a thin film of a conductor (perfect electrical conductor in software simulations). In the middle of the structure it has been introduced a thin Z-cut cylindrical substrate of Lithium Niobate, with the optical circuit integrated in, so that it is deployed in the transverse section of the cylinder. It's worth noting that this configuration relates the radius of the cylinder to the dimension of the MZI. Although, at this stage the integrated optical circuit is not yet defined, a realstic value has to be considered. The height of the cylinder, d, has been fixed to $1cm$, in order to

reduce the scattering section and at the same time dimensions of the lateral surface sufficient to couple the cavity with the external electromagnetic radiation. It's worth noting that the scattering section of the configuration can be further reduced, by substituting the metallic film of the basis by a proper dielectric material with high permeability ($\mu_r \gg 1$) or with a multi-stratus structure.

Although made of a stratified structure, due to the small value of $LiNbO_3$ substrate thickness $(0.5mm)$, the overall device can be assumed as a homogeneous cylinder loaded with metal films on the basis, from thw microwave point of view. Hence, the structure can be analysed by using a cavity model: lateral surface of the cylinder is assumed to be perfect magnetic conductor (PMC). This could allow to evaluate the resonance frequencies and field distribution of modes in a closed form. Permittivity of the dielectric material, constituting the resonator, has been chosen in $\epsilon_r = 14$. This choice is given by a trade-off between two opposing needs. From one side, the value of ϵ_r should be increased in order to reduce improve the accuracy of the cavity model and reduce the dielectric discontinuity with $LiNbO_3$. On the other side, a low value of ϵ_r improves the radiative coupling (and, due to reciprocity, the receiving) of the structure. In addition it allows increasing the single-mode operating bandwidth.

The analysis has been also performed with the EMsS. A schematic of the dielectric resonator probe as it appears in the EMsS is reported in Fig.2.9. According to the cavity model, the fundamental mode has been found out to

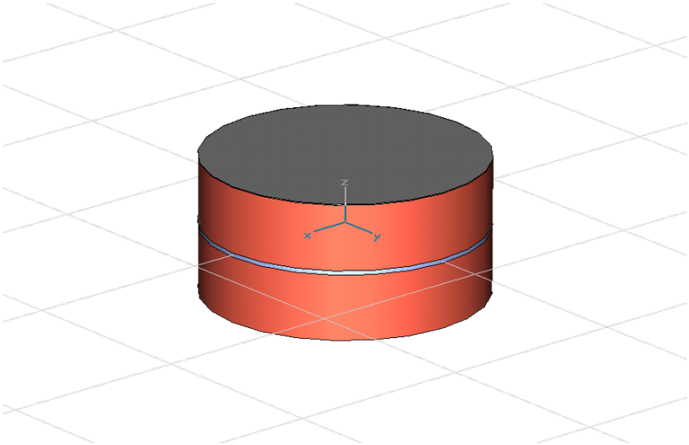

Figure 2.9: Dielectric Resonator Probe schematic: $LiNbO_3$ substrate (blue color), homogeneous dielectric material (red colour)

Mode	Cut-off Frequency (GHz)
1	1.35 GHz
2	2.23 GHz
3	2.81 GHz
4	3.07 GHz
5	3.89 GHz

Table 2.2: Cut-off frequency of resonance modes

be a transverse magnetic (TM) one. In particular, it is a (TM_{110}), characterized by the components H_r E_ϕ and E_z, whose cut-off frequency is given by:

$$f_{mnp} = \sqrt{\left\{ \begin{matrix} X_{np}^2 \\ X'^2_{np} \end{matrix} \right\} + [\frac{\pi a}{2d}(1+m)]} \tag{2.1}$$

where X_{np} and X'_{np} are the positions of the first null of the $n-th$ Bessel ordinary function, $J_n(x)$, and of the null of its first derivative, $J'_n(x)$, respectively.

The eigenmode solver of the EM simulator provides results compliant with those evaluated by means of the ideal model of the cavity. In particular, the software predicts the cut-off frequencies for the first five modes, indicated in Tab. 2.3: These frequencies computed by EmSS well matches with the theoretical frequencies computed by 2.1. Numerical analysis shows also that the electric field of the fundamental mode is essentially given by the E_z component in the active region of the device. It's worth noting that the first higher mode is a transverse electric (TE) and therefore and, therefore, is not suitable for an effective EO modulation: it presents only E_x and E_y components. Therefore, the dielectric resonant sensor should operate on the fundamental mode only.

As seen from eq. 2.1, by increasing the ratio a/d it is possible to separate the resonance frequency of the higher order modes from that of the fundamental mode. Therefore, on one side, in is possible to reduce d, affecting the coupling of the cavity with external excitations. On the other side, it is possible to increase a, increasing unfortunately the scattering section of the device as well. Accordingly, there is a trade off regarding the choice of a/d that does not allow to achieve operative bandwidth larger than $1GHz$ on the fundamental mode. In addition, the operating frequency range of the device is limited to the low frequency range, lying completely outside of the X-band. Indeed, to increase the cut-off frequency of the fundamental mode the radius of the cylinder, a,

should be significantly reduced, implying a consequent reduction of the active length of the MZ interferometer that lies in the cylinder cross-section. Consequently, the sensitivity of the probe will be unacceptably reduced. By the way, it is possible to double approximately the cut-off frequency of the fundamental mode, without losing in sensitivity, by reducing a to a half its previous value with a MZI operating in reflection. Indeed, by splitting into halves the MZI and by introducing a reflecting coating at the end of its braches, the optical signal can propagate itself two times in the same half of the MZI, running a complete interferometer.

In conclusion, numerical and analytical analysis showed that it is not possible to obtain an operating bandwidth comparable to that one of interest. In particular, we beieve that the dielectric resonator probe cannot operate at frequencies higher than $4GHz$. However, this frequency limit can be enough in many applications of EMC and environmental noise control.

2.4 Travelling Wave EO Sensor

The limits of the configurations previously considered indicate that the introduction of electrodes in the structure, in order to achieve a device which better matches with the requirements. Electrodes, indeed, force field lines to take a peculiar shape in their proximity, despite of the features of the excitation. Therefore, by properly designing the electrodes it is possible to guarantee an effective EO modulation in all the operating conditions. At the same time, it is reasonable that electrodes with a small surface still preserve the non-invasive behaviour, if compared to that one of OEW. Then, the considered probe structure is made up of a Lithium Niobate crystal substrate, where an EO modulator integrated in and proper metallic elements are printed on.

As pointed out in section 2.1, the EO probe should have adequate sensitivity to detect field intensity value typical achieved with standard indoor NF characterization systems. Unfortunately, sensitivity is a critical point of the design of photonic probes as it is involved in a trade-off with non-invasive behaviour and bandwidth. Indeed, to contain the probe scattering section to the lowest possible one, an integrated lumped EO modulator can be considered as in [19, 17, 20]. But, as indicated in section 1.2 lumped modulators present usually high half-wave voltage values that increases with the maximum operating frequency. Hence, a photonic probe operating on a wide frequency range and integrating a lumped modulator could provide an unacceptable low sensitivity, requiring some microwave and optical amplifications stages along the

measurement chain.

In order to improve the sensitivity and avoid more complex and expensive measurement equipments, an innovative solution exploiting an integrated TW EO modulator, instead of a lumped can be considered. The electrically longer electrodes improve the sensitivity of the probe without significantly affecting its non-invasive behaviour. Furthermore, the TW configuration ensures a wider operative frequency range, covering even more of the bandwidth considered till now. Although the choice of the crystal cut affects the topology of the optical waveguides, at this stage it is not necessary to discuss about it.

In order to satisfy the polarization selectivity requirements, a small printed antenna is introduced and connected to the modulator as source generator for the modulating signal. In Fig. 2.10 a schematic of this configuration is presented. Alternatively, it is possible to consider a different design strategy,

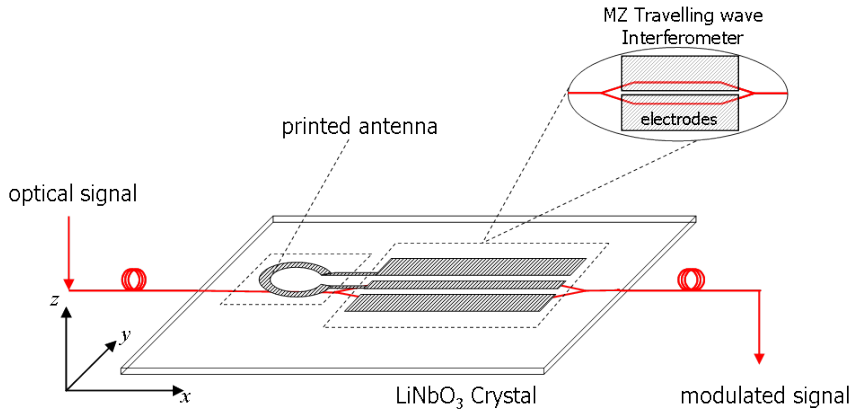

Figure 2.10: Travelling Wave probe schematic

where the antenna and the electrodes of the EO TW modulator are integrated together in a single structure. Unfortunately, this solutions has demonstrated to be ineffective for the application of interest, because of its high complexity. Indeed, the design involves a single printed structure, that should act on a large frequency band as a receiving antenna, satisfying requirements concerning selectivity, and at the same time as a matched TL. However, this design strategy has been explored: some promising structured have been identified and analysed by means of the EmSS. Unfortunately none has shown to fully satisfy the required specifications and, for the sake of brevity, the performed analysis is not reported here.

Hence, a modular approach has been adopted: a conventional TW EO modulator driven by a printed antenna. This choice allows also to separate device design parameters that are responsible for the polarization selectivity (printed antenna parameters) from those ones related to the sensitivity (parameters of the TL), providing a more easy control in the design of the structure. Another advantages of the modularity is that it introduces a further degree of freedom, opening the way to the realization of the printed antenna, even on substrates different from $LiNbO_3$. Naturally, proper interconnection of the two substrates with the printed structures can be not trivial. However, it worth noting that matching the antenna impedance with the TL characteristic impedance is not critical. An eventual small mismatch, indeed, would reduce only the sensitivity of the probe (maximum when the matched condition is accomplished), but not affect its correct functioning. Therefore, as fas as the probe sensitivity degradation is acceptable, the impedance mismatch can be disregarded.

As the range of variation of some parameters of the EO modulator can be limited by the specifications of the integrated optical circuit, it's worth discussing the MZI design before facing the design of the printed structure. In turns, this last point can be naturally divided in two independent tasks: the design of the TL and the design of the printed antenna. Hence, to accomplish the design of the overall device it is necessary to accomplish three main design tasks:

1. the design of the integrated optic circuit
2. the design of the transmission line
3. the design of the printed antenna

The EO TW modulator design, that is articulated on the above tasks, has been carried out in cooperation with Department of Electro-technique and Electronic of Politecnico di Bari and the Centro per la Ricerca Elettronica in Sicilia. Next sections discuss separately the identified design tasks.

2.4.1 Optical Circuit Design

Naturally, in order to design an integrated optical circuit the first point to be addressed is the determination of the waveguide structure [44], the basic element for the construction of a optical circuit. Therefore, the first aspect to be discussed concerns the waveguide fabrication technology. Thermal Annealing

Proton exchange (TAPE) [45], based on a blend of Benzoic Acid and Lithium Benzoate at 3%, on Z-cut (Y-propagating), has been chosen to realize waveguides for the optical signal in Lithium Niobate. This technology ensures low losses channel waveguides [44] for extra-ordinary waves, without affecting EO properties of the substrate [45]. The optical wavelength has been fixed to $1550nm$ in order to reduce photo-refractive effects.
For sake of convenience let us introduce a Cartesian reference system, $Oxyz$ with x and y axis parallel respectively to the crystallographic direction $Y(010)$ and $Z(001)$ of Lithium Niobate. The chose characteristics of the TAPE process lead to a refraction index variation is given by [45]:

$$\begin{aligned}\Delta n(x,y) \quad &= \Delta n_0 \cdot \quad \frac{erf(\frac{d_e+x}{d_x}) + erf(\frac{d_e-x}{d_x})}{2 * erf(\frac{d_e}{d_x})} \\ &\cdot \frac{erf(\frac{w+y}{d_y}) + erf(\frac{w-y}{d_y})}{2 * erf(\frac{w}{dy})}\end{aligned} \tag{2.2}$$

where $\Delta n_0 = 0.0253$ at $\lambda = 1310nm$, $d_e = 3\mu m$, $d_y = 1.82\mu m$, $w = 0.6\mu m$ and $d_x = d_y/1.18$. In Fig.2.11 a contour plot of the transverse section refractive index profile is presented. It's worth noting that a buffer layer of bi-oxide of Silicium (SiO_2), $1\mu m$ thick, has been deposited over Lithium Niobate in order to make the realisation of electrodes easier. By means of a software simulator suited for integrated optics device design, the structure has been analysed to determine the guiding characteristics. In particular, numerical analysis indicated that the structure is single-mode: a quasi-TM fundamental mode is supported and higher order do not propagate at the chosen operative wavelength. In Fig.2.12 it is reported the computed fundamental mode field distribution. A simulation has been performed to evaluate optical losses of waveguides. The flow of the optical power when the fundamental mode is propagating along the waveguide has been computed. Results, reported in Fig. 2.13, show that the optical losses are small. Indeed, it is possible to estimate that waveguide losses are approximately equal to $.35dB/cm$, that is a reasonable value.

It is possible, then, to proceed on whit the design of the integrated Mach-Zehnder Interferometer. The adopted solution is a geometrically symmetric MZI, whose dimensions are indicated in Fig. 2.14. The MZI is made up of two symmetrical Y-junctions, that spaces the arms of $100\mu m$. This distance has been fixed in order to ensure that tails of optical modes propagating in the arms do not interfere. Input and output channels are $3mm$ long. Y-junctions

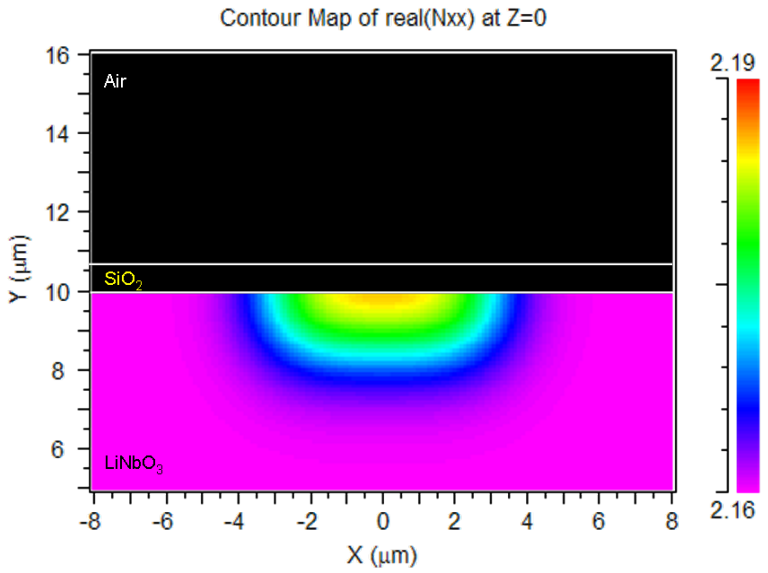

Figure 2.11: Index profile in the transverse section of the TAPE waveguide

are made with S-bend waveguides in order to reduce optical losses, and are connected to input and output channels by means of linear tapers, whose length is $1mm$. The active length of the interferometer, L, has not yet fixed as it can be tuned in a later stage on the basis of the sensibility requirements and of the actual losses of both the optical waveguide and the microwave TL.

As no electrical biasing is possible in a EO field sensor and a symmetrical structure has been considered, the operating point of the MZI is determined by an optically differentiation the two paths. Indeed, by controlling the thickness of a oxide film on the interferometer arm, it is indeed possible a fine control of the optical mode effective refractive index [44]. Titanium Dioxide (TiO_2) and Telluride Dioxide (TeO_2) have been individuated as film material with the proper characteristics to ensure the achievement of the MZI operating point.

It's worth noting that, when the MZI operates in reflection fashion, it is possible to obtain the phase biasing between the two optical paths by a proper oblique lapping of the reflecting coating. In Fig. 2.15 a schematic of this strategy is presented.

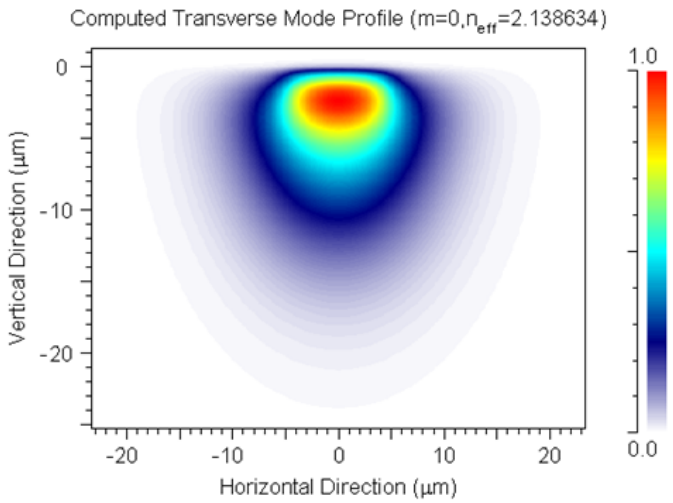

Figure 2.12: Fundamental mode of the TAPE waveguide

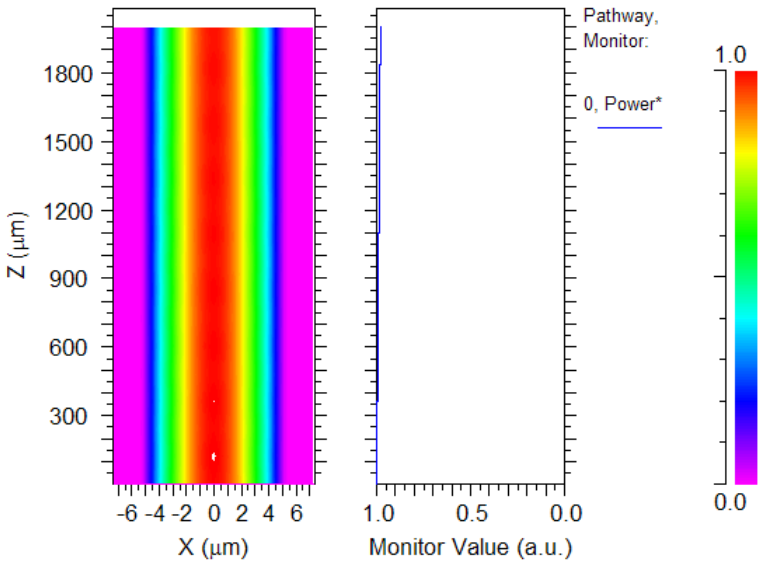

Figure 2.13: Optical power losses of the TAPE waveguide

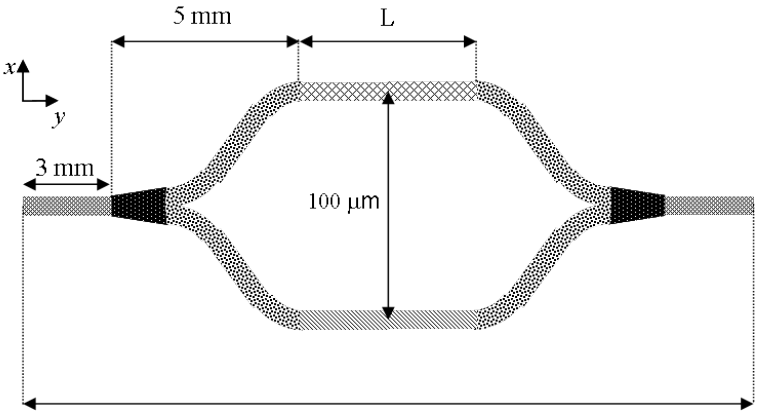

Figure 2.14: Designed Mach-Zehnder Interferometer

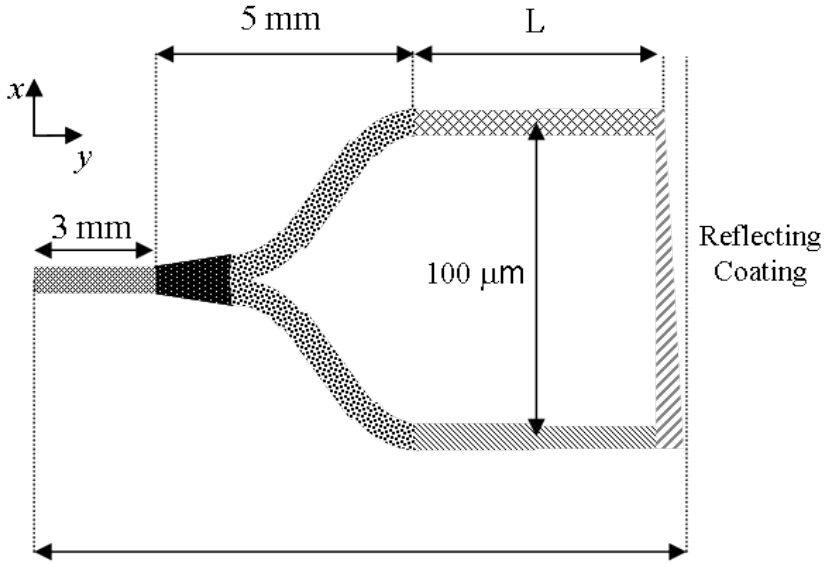

Figure 2.15: MZI operating in reflection

The MZI operating in reflection enables a simpler and effective solution to the optical biasing of the interferometer. Indeed, once the device has been realised, by means of a cut and try lapping process the correct phase bias can be easily obtained. Therefore, the biasing problem can be reminded later on when the final probe topology will be defined.

2.4.2 Transmission Line Design

Typically, two different coplanar guiding structures can be used to realize EO TW modulators [47]: asymmetrical coplanar stripes (ASL) and coplanar waveguides (CPW) [28]. These two guiding structures differ essentially for the number of electrodes: three for CPW and two for ASL. Depending on the crystal cut and the TL choice, the position of the integrated MZ interferometer can change. Indeed, the various configurations that can be exploited are schematically illustrated in Fig. 2.16. A CPW configuration has been chosen to realize

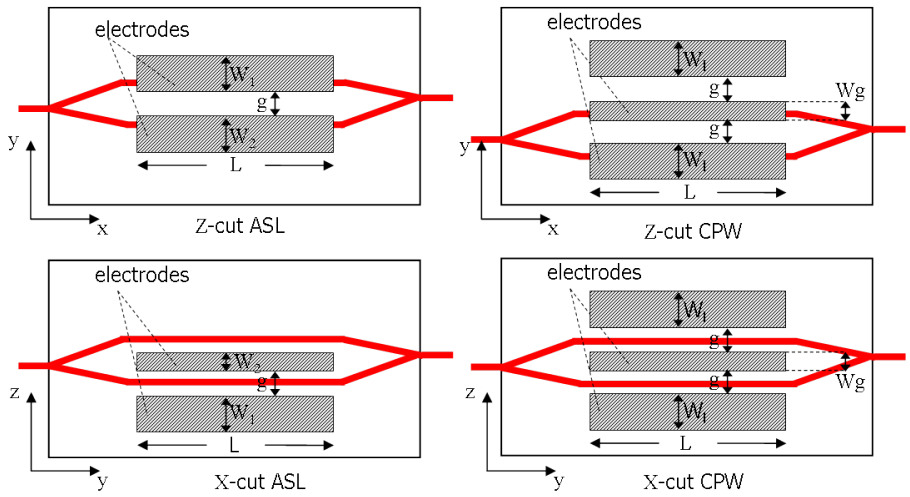

Figure 2.16: Travelling Wave EO configurations

the TW interferometer as it can provide a lower half-wave voltge [47]. In Fig. 2.17 the geometry of the TL is depicted, enlighten the design parameters. In a first design stage, parameters of the CPW has been determined by exploiting synthesis formulas [48], based on the conformal mapping approach [48, 28]. The anisotropic substrate has been taken into account accordingly to [46]. This

Parameter	Value	Unit
$G_1 = G_2$	16	μm
$W_1 = W_3$	100	μm
W_2	8	μm
H	1	μm
T	12	μm
Z_m	48.6	Ω
V_π	5.94	V/m
α_0	0.39	$dB/cm\sqrt{GHz}$
B	19.5	GHz

Table 2.3: EO TW Parameter

stage has been necessary in order to rapidly but approximately determine the geometrical dimensions of the TL. Then, these values have been exploited as input values of a parametric analysis, based on the more accurate Fourier Series [49] approach, that leaded to the final design parameters. Tab. 2.3 shows

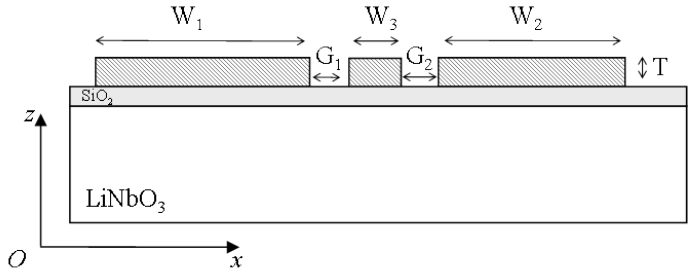

Figure 2.17: Coplanar Wave-Guide Transmission Line: cross-section view

the geometrical parameters together with the relative characteristic of the EO TW modulator. where $G_1, G_2, G_3, W_1, W_2, W_3, T, H$ are geometrical parameters defined in Fig. 2.16, Z_m is the characteristic impedance of the TL line, B is the bandwidth, V_π is the half-wave voltage and α_0 is the loss coefficient of the TL.

In principle, the connection of the optical circuit integrated in the $LiNbO_3$ substrate to the optical part of the measurement chain would require two fiber optics and two relative connectors at the terminals of the MZ interferometer. One, the up-link fiber, carries the optical signal from the source to the integrated circuit, while the other, the down-link fiber, carries the modulated

signal to detection instrumentations. It's worth noting that optical connections are typically fragile and require special care in handling. In addition, their realization is not a trivial task: micro-metric positioners are needed to accomplish the connection. Naturally, it's evident that, even if the scattering section of fiber optics is negligible, the possibility of connecting the probe with only one fiber optic can make easier the interfacing of the device with the AUT. Indeed, the input-output connection can be located in the back-side, the side not in front of the AUT, making the other sides free from the connector that could limit the manageability of the probe. Clearly, in this case the probe must be polled in a reflection fashion and an optical circulator must be employed. In Fig. 2.18 a schematic of the probe structure in reflection fashion is depicted. Unfortunately, the realization of the return path (Rx in Fig. 2.18)in integrated

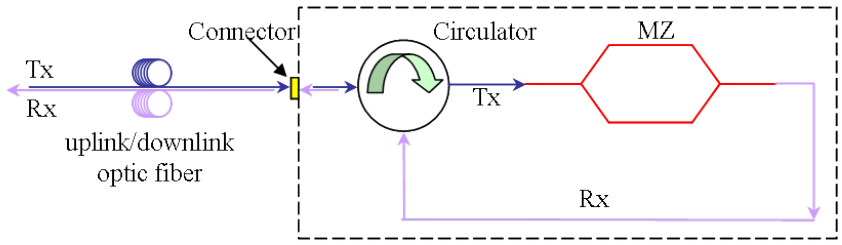

Figure 2.18: Reflection polled probe

optical technology introduces unavoidably high optical power losses. Indeed, in order to obtain a shorter path and contain probe dimensions, lossy sharp bends of the waveguide can be used. Alternatively, leaving aside the problem of the scattering section, smooth bend waveguides can be employed realizing longer paths thus still contributing to the optical power losses.

The above considerations have pursued a different solution to allow the device operating in a reflection fashion. In particular, to avoid high power losses an interferometer working in reflective configuration has been considered the possibility of exploiting the one optical path for forward and backward direction, by introducing a reflecting mirror. This leaded to an alternative configuration of MZ interferometer where there is a single Y-branch and the two arms are terminated on a reflecting coating so that a complete interferometer is achieved by forward and backward propagation of the optical signal. In Fig. 2.19 it is schematically depicted the considered MZ interferometer configuration. This MZ configuration is adopted only in lumped EO modulators.

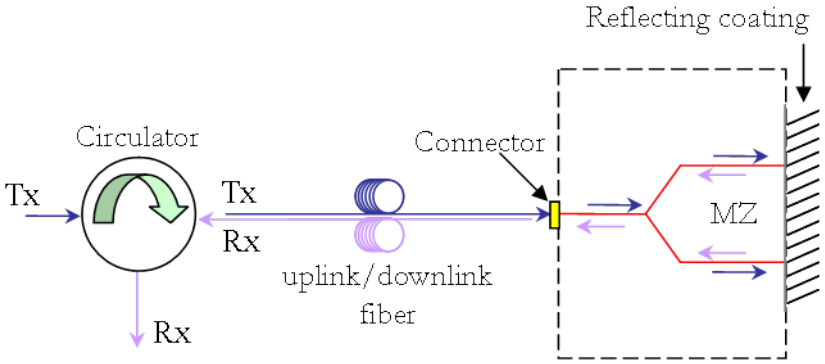

Figure 2.19: Reflection MZ interferometer

Such MZ configuration has been generally considered not suitable for TW EO modulators, because of the phase velocity mismatch that arises in the backward propagation of the optical signal. Nevertheless, the analysis performed showed that under certain conditions this solution can be adopted even in a TW modulator. In Fig. 2.20 it is schematically represented the TW modulator configuration, where β_z is the guided wave propagation constant [50] and Z_0 is the line intrinsic impedance.

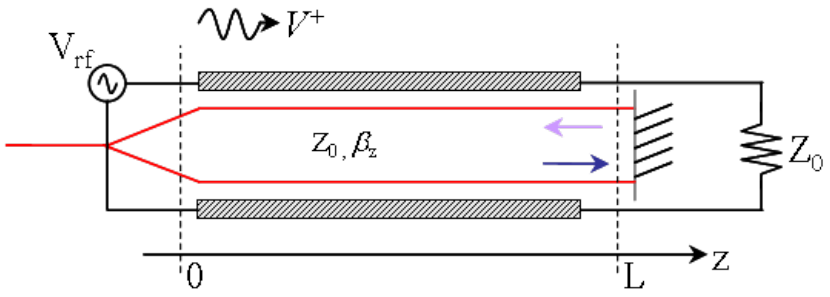

Figure 2.20: Reflection TW modulator

Let us assume that the phase velocity match condition is valid in the forward propagation: $\nu_o = \nu_{rf}$, where ν_o is the optical signal phase velocity and ν_{rf} is the microwave signal phase velocity. Then, the EO retardation [3]

accumulated in the forward path is given by:

$$\Delta\phi_f = \beta_0 \frac{n_e^3}{2} r_{33} \frac{E_z}{d} L \tag{2.3}$$

In the return path $\nu_o = -\nu_{rf}$ and the EO retardation is instead given by:

$$\Delta\phi_b = \frac{\beta_0 n_e^3 r_{33}}{2} \int_L^0 \frac{|E_z|}{d} \cos\left(\beta_z z + \omega_{rf} t + \angle E_z\right) dz \tag{2.4}$$

Due to the small refractive index change by EO effect, it is reasonably to assume that the phase velocity of the optical signal does not change and the signal propagates with a constant velocity equal to ν_o. This allows to retain that at the time t, the optical wave front is at the section $z = L - \nu_o * t$. Substituting in eq. 2.3, it results:

$$\begin{aligned} \Delta\phi_b &= \tfrac{\beta_0 n_e^3 r_{33}}{2} \textstyle\int_L^0 \tfrac{|E_z|}{d} \cos\left(\beta_z z + \omega_{rf} \tfrac{L-z}{\nu_o} + \angle E_z\right) dz = \\ &= \tfrac{\beta_0 n_e^3 r_{33}}{2} \textstyle\int_L^0 \tfrac{|E_z|}{d} \cos\left(\tfrac{\omega_{rf}}{\nu_{rf}} z + \tfrac{\omega_{rf}}{\nu_o}(L-z) + \angle E_z\right) dz \end{aligned} \tag{2.5}$$

Recalling the relationship between ν_o and ν_{rf}, eq. 2.3 becomes:

$$\begin{aligned} \Delta\phi_b &= \frac{\beta_0 n_e^3 r_{33}}{2} \int_L^0 |E_z| \cos\left(\frac{\omega_{rf}}{\nu_{rf}} z - \frac{\omega_{rf}}{\nu_{rf}}(L-z) + \angle E_z\right) dz \\ &= \frac{\beta_0 n_e^3 r_{33}}{2} \int_L^0 |E_z| \cos\left(\frac{\omega_{rf}}{\nu_{rf}}(2z-L) + \angle E_z\right) dz = \\ &= \frac{\beta_0 n_e^3 r_{33}}{2} \frac{|E_z|}{d} \frac{\nu_{rf}}{\omega_{rf}} \left[-\sin\left(\frac{\omega_{rf}}{\nu_{rf}}(2z-L) + \angle E_z\right)\right]_L^0 \\ &= \frac{\beta_0 n_e^3 r_{33}}{2} \frac{|E_z|}{d} \frac{\nu_{rf}}{\omega_{rf}} 2\sin\left(\frac{\omega_{rf}}{\nu_{rf}} L + \angle E_z\right) \\ &= \beta_0 n_e^3 r_{33} \frac{|E_z|}{d} \frac{\omega_{rf}}{\nu_{rf}} \sin\left(\frac{\omega_{rf}}{\nu_{rf}} L + \angle E_z\right) \end{aligned} \tag{2.6}$$

The total EO retardation accumulated during the propagation consists in the two contributions of eqs. 2.3 and 2.4, and is given by:

$$\begin{aligned} \Delta\phi &= \Delta\phi_f + \Delta\phi_b = \frac{\beta_0 n_e^3 r_{33}}{2} \frac{|E_z|}{d} L\left[1 + \frac{\nu_{rf}}{\omega_{rf} L} \sin\left(\frac{\omega_{rf}}{\nu_{rf}} L + \angle E_z\right)\right] \\ \Rightarrow\ & \Delta\phi \le \Delta\phi_f + \Delta\phi_b^{max} = \frac{\beta_0 n_e^3 r_{33}}{2} \frac{|E_z|}{d} L\left[1 + \frac{\nu_{rf}}{\omega_{rf} L}\right] \end{aligned} \tag{2.7}$$

TW modulator have usually electrodes length much longer than the guided wavelength. Therefore, it results that:

$$L \gg \lambda_{rf} \Rightarrow \frac{\nu_{rf}}{\omega_{rf} L} = \frac{\lambda_{rf}}{2\pi L} \ll 1 \tag{2.8}$$

It's worth nothing that, as quantities concerned are involved in a phase term, periodicity of 2π should be considered. This means that even if implication in 2.8 holds in the general case, no approximation can be made in 2.7 as it is not possible to state if $\Delta\phi_b^{max}$ is negligible with respect to $\Delta\phi_f$. Indeed, forward and backward contributes should be evaluated modulus 2π and therefore their values can be arbitrary.

Nevertheless, as far as the hypothesis of linear functioning of the EO modulator holds, the phase shifts introduced in the both the forward and return paths are much smaller than the biasing contribute of $\pi/2$. Accordingly, their values fall inside the interval $[0, 2\pi]$ and periodicity can be disregarded, achieving the result:

$$\Delta\phi = \Delta\phi_f + \Delta\phi_b \cong \frac{\beta_0 n_e^3 r_{33}}{2} \frac{|E_z|}{d} L \tag{2.9}$$

Hence, it is possible to retain that the contribute to EO modulation introduced by the return path is negligible if compared to the contribute of the forward path as far as the EO modulator operates in the linear region and the interferometer length is greater that the guided wavelength. Concluding, it is possible to realise a TW modulator in reflection fashion exploiting half a MZI travelled two times in opposite directions.

2.4.3 Printed Antenna Design

In order to exploit the wide operating frequency band of the TW modulator, wideband antenna configurations have been considered. In particular, Bow-Tie dipole, loop and spiral antenna. Among them, the Bow-Tie resulted to be the most proper configuration, as it ensures the best compromise between the feasibility needs and the radiative and circuital behaviour required. Indeed, the realisation of the antenna electrodes and its feeding network is not critical in planar technology. Further, such a configuration provides a radiative behaviour comparable to that one of an elementary dipole in a wide frequency band. In Fig.2.21 the Bow-Tie antenna is schematically represented, with its design parameters. Naturally, the design parameters values must be compliant with the physical limitation imposed by the substrate. Indeed, to contain the scattering section the substrate dimensions have been fixed to $2cm$x$5cm$x$0.5mm$.

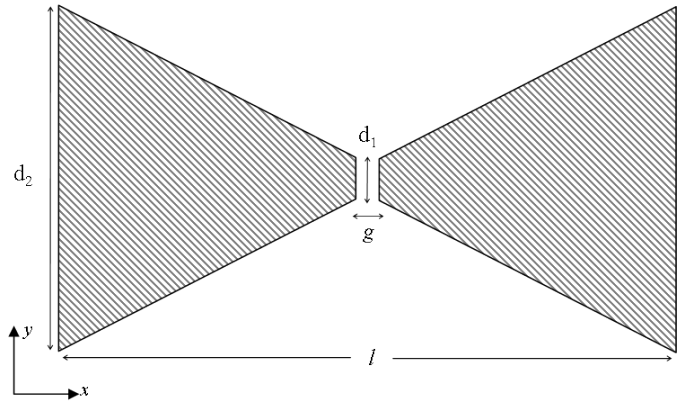

Figure 2.21: Printed Bow-Tie Antenna

By means of a parametric numerical analysis the optimal geometrical parameters d_1, d_2, g and l have been determined, in order to ensure the proper circuital and radiative behaviour to the structure. Tab.2.4 reports the antenna parameters: The feeding line of the antenna is a symmetrical coplanar stripes

Parameter	Value	Unit
d_1	1.14	mm
d_2	13.3	mm
g	20	μm
l	19	mm

Table 2.4: Bow-Tie antenna design parameters

(CPS) [28], schematically represented in Fig.2.22 The design parameters of the feeding network are indicated in Tab. 2.4.3. The transverse dimension of

Parameter	Value	Unit
w_{cps}	80	μm
l_{cps}	1	mm

Table 2.5: Bow-Tie antenna feeding line design Parameters

the CPS have been chosen optimizing the impedance match with the antenna.

The circuital behaviour of the antenna has been analysed by means of the voltage standing wave ratio (VSWR) numerically estimated at the transmission line terminals. Fig.2.23 reports the VSWR normalised to an input impedance

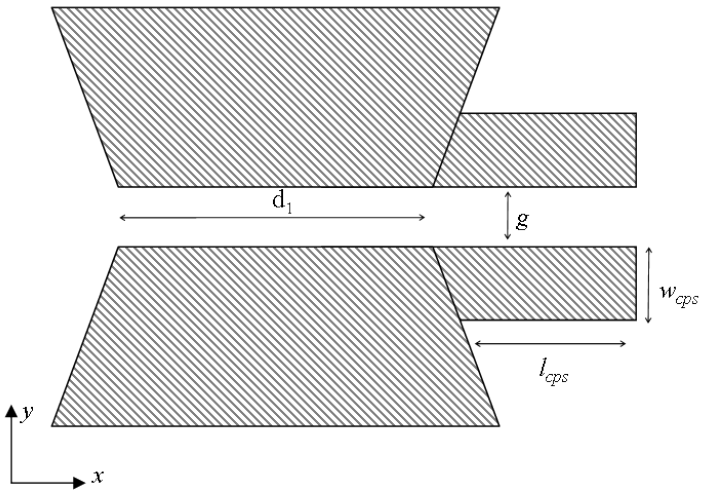

Figure 2.22: Bow-Tie Antenna feeding line

of $50Ohm$ (blue line) and a reference line (red line) that represents the typical acceptable threshold value, that is 1.75. Is is evident that in a wide frequency range $[2.6GHz, 12Ghz]$ the VSWR is under the threshold value. In particular, the Bow-Tie antenna presents an almost flat behaviour in all the X-Band. Therefore, the numerical analysis shows that the considered structure can be employed to pilot the EO TW modulator in a wide portion of its operating frequency band. Only low frequency of the interest bandwidth are, indeed, excluded.

The numerical analysis showed that radiative characteristics of the considered antenna do not change significantly in the interest bandwidth. Therefore, for sake of brevity, the estimated radiative behaviour is presented at only one representative frequency: the middle frequency of X-band, $10.25GHz$. The pattern is reported on three coordinate plane cuts, plane xy, plane xz and plane yz, which are presented in Figs. 2.24-2.26, respectively. The copolar component is assumed to be E_θ while cross-polar is E_ϕ. As expected, the radiative behaviour of the bow-tie antenna is quite close to that one of an elementary dipole. Further, numerical analysis showed that the antenna ensures a sufficient isolation between copolar and crosspolar components that it's effective length can be assumed linearly polarized.

Concluding, the bow-tie antenna satisfies the requirements concerning the

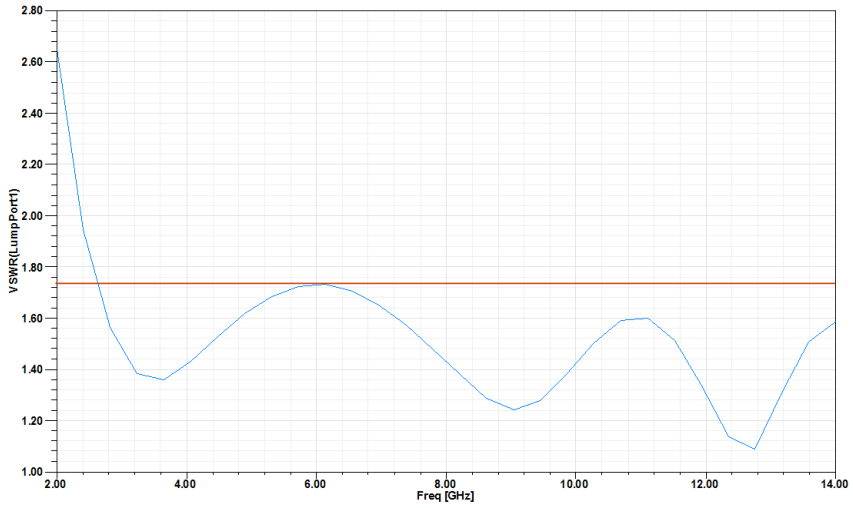

Figure 2.23: Bow-Tie Antenna Voltage Standing Wave Ratio

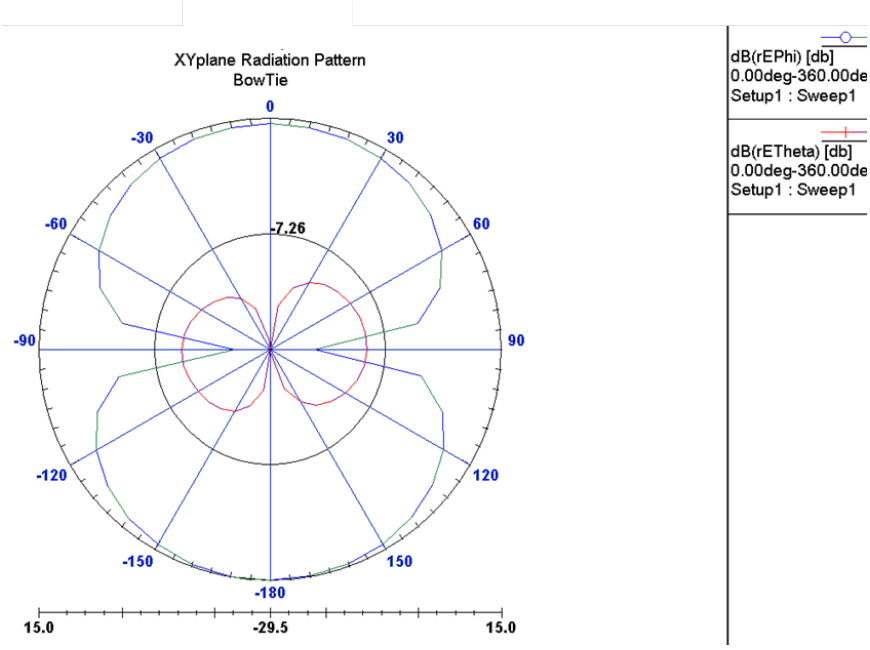

Figure 2.24: Radiation pattern cut - plane xy ($\theta = \pi/2$)

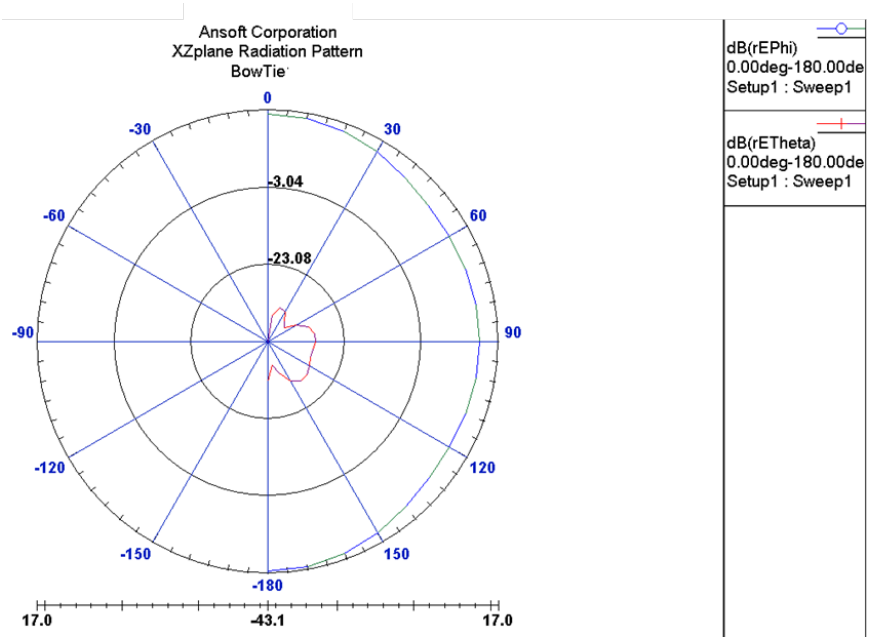

Figure 2.25: Radiation pattern cut - plane xz ($\phi = 0$)

operating bandwidth and the selectivity towards the impinging polarization.

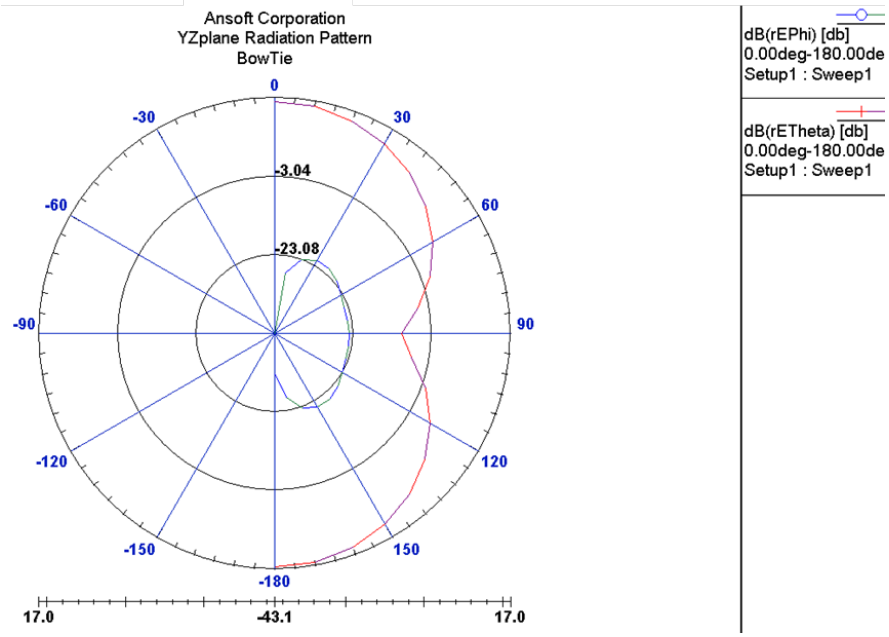

Figure 2.26: Radiation pattern cut - plane yz ($\phi = \pi/2$)

Chapter 3

Phaseless Antenna Characterization

Near-Field techniques [51, 52] are nowadays consolidated and routinely exploited for the experimental characterization of antenna systems. Naturally, the diagnosis of the antenna from NF data requires the accurate knowledge of complex (amplitude and phase) near-field distribution, on a surface of pre-assigned geometry that, in principle, encloses the radiator.
It's worth noting that the direct phase measurement bears significantly on the complexity of a NF characterization system, imposing stricter specifications on the overall system devices. Indeed, it requires more sophisticated and performing equipments, such as vectorial network analysers (VNA) [59], phase-stable cables [60], high-accuracy positioners [61, 62], environmental conditions (humidity, temperature) controlling systems, that become more and more expensive with the increasing frequency. When dealing with the millimeter and submillimeter bandwidths [109], constraints imposed by phase measurements can hardly be satisfied by NF facility equipments and the accuracy of the measurements can reduce significantly, up to become unacceptable in some cases. Accordingly, reliability of conventional NF-FF transformation techniques can be compromised and the NF characterization can be impracticable.

The above described issues have recently pursued the development of alternative NF-FF phaseless techniques, able to estimate the FF pattern by only amplitude data. In particular, in the last decades a significant effort has been devoted to the development of various *phaseless* NF-FF techniques [63, 64, 65, 66] that retrieve the phase information from field amplitude data.

Basically, phase retrieval consists in an inverse problem and it amounts to

optimize a non-linear cost functional [70], whose local minima can affect significantly the performances, trapping the optimization algorithm into useless *false solutions*. As a consequence, the key point for a successful retrieving involves either a proper formulation of the inverse problem, a suitable choice of the starting guess of the iterative procedure and/or, when possible, the use of an effective global optimization strategy [68, 69].

On this basis, in the last years at DIBET of *University of Naples Federico II* phaseless NF-FF techniques have been successfully developed [71, 72, 73] and widely experimentally validated [74, 75] even at millimetre-wave frequencies [76, 77]. This approach exploits a proper representation of the aperture field based on a suited set of basis functions, in order to include the available *a-priori* information on the radiating system.

In this chapter the results in antenna phaseless NF-FF characterization field of the activity accomplished during the Ph.D. Course at DIBET is presented. In particular, a novel approach, that generalizes the representation strategy introduced in [71] for the the planar scanning geometry, is here discussed. The approach exploits the development of a proper generalized set of basis functions, referred to as Generalized Prolate Spheroidal Wave Functions (G-PSWFs). By means of this suited set all the available a-priori information, concerning the radiator geometry and the general properties of far-field, can be completely incorporated in the model, mitigating typical problematic of phase retrieval problems.

The proposed approach has been extended to cylindrical scanning geometries, by means of a proper mathematical framework. The considered modelling, however, is independent from the representation adopted for the aperture field and, thus, valid in the general case (PSWFs, G-PSWFs, Sinc).

In addition, by referring to the planar scanning geometry, the phase retrieval problem in presence of mild incoherence of the measurement planes has been addressed. Indeed, alignment in antenna measurement is not trivial [116] and especially when two measurement surface are concerned for a phaseless characterization, a small offset between acquisition planes can occur. In order to make more robust and reliable the developed phase retrieval technique, misalignment has been properly introduced in the mathematical model and retrieved by the inversion algorithm.

Before discussing details of the above described topics, a preliminary section introduces the statement of the problem of phase retrieval. Furthermore, in the final section of the chapter some representative experimental results will be presented.

3.1 Phase Retrieval Problem

The phase retrieval problem [78, 79] consists in the determination of the phase of a monochromatic source from the knowledge of only-amplitude of the tangential field over prescribed observation domains. This problem is of interest in several branches of applied physics, such as optics, holographic image electron microscopy, where only the field amplitude information can, or can more conveniently, be measured [80, 81, 82]. Clearly, when dealing with antenna characterization the measurement domain is located in the near-field region of the radiator.

Phase retrieval is intrinsically a non-linear problem [70, 78], that is naturally faced as an inverse one. In addition, the retrieve of phase information is further complicated by the presence of noise. Noise, indeed, unavoidably affects data making the problem ill-posed [83].

It's worth noting that in phase retrieval problems uniqueness of solutions is in general an issue, and it is ensured under certain conditions [85]. Much work has been done about this subject in phaseless retrieval problem, therefore we do not discuss uniqueness of solution in this thesis work. We assume from now on that uniqueness is guaranteed in the considered formulation and we remand to references [84, 85, 86, 87, 88, 89] for a complete treatment of the subject.

Several approaches have been proposed in literature to retrieve the phase from amplitude data, all practically based on the optimization of a proper objective cost functional. These techniques can be, however, divided in two main categories. On one hand, those exploiting two probes on the same scanning domain [66, 92] to collect the data set. On the other hand, techniques exploiting the same probe on two different scanning surfaces [63, 64, 65, 71].

From now on we will focus on the two acquisition surfaces strategy, as this is the approach adopted by the techniques recently developed at DIBET [71]. In particular, we assume that the measurement surfaces are planar and the source is equivalently represented by a planar aperture of finite extent and arbitrary geometry. Hence, the problem of phase retrieval can be stated as follows.

Let us consider a $Oxyz$ reference system and assume that the planar source, say D_{ap} (the aperture domain), lies on the plane Oxy. The two measurements surfaces, say Σ_1 and Σ_2, located in the near field zone and (ideally) enclosing the radiator are planes parallel to Oxz coordinate plane and far apart from the aperture z_1 and z_2, respectively. The geometry of the problem is schematically depicted in Fig.3.1. For sake of simplicity, let us also assume

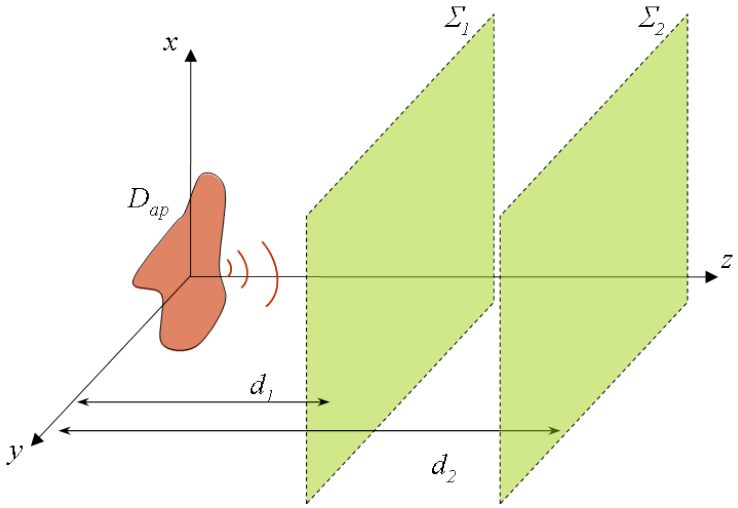

Figure 3.1: Geometry of the Phase Retrieval Problem

that the electromagnetic field is linearly polarized. It's worth noting that this assumption do not affects the generality of the problem.

Let us denote with E_{ap} the component of the electric field, tangential to the aperture plane, and with X the functional space of all possible aperture field. It is natural to assume that $\mathcal{X}$ is a subset of the space of the square integrable function on D_{ap}: $\mathcal{X} \subseteq \mathcal{L}_2(D_{ap})$. Let us now define $M \doteq (M_1, M_2)$, where M_1 and M_2 are the amplitude of the component of the electric field tangential to the first and the second measurement surface, respectively. Then, it results that:

$$\begin{cases} M_1(x,y) = \|\mathcal{F}^{-1}[\mathcal{F}[E_{ap}]e^{-j\beta z_1}]]\| \doteq \|\mathcal{T}_1[E_{ap}]\| \\ M_2(x,y) = \|F^{-1}[F[E_{ap}]e^{-j\beta z_2}]]\| \doteq \|\mathcal{T}_2[E_{ap}]\| \end{cases} \tag{3.1}$$

where β is the wavenumber, $\mathcal{F}$ is the Fourier Transform operator and $\mathcal{T}_i = \mathcal{F}^{-1}[\mathcal{F}[\cdot\,]\exp -j\beta z_i]$, i.e. the composite linear operator transforming the aperture field to the field on the i-surface, with $i = 1, 2$. It's sounds clear that the range of the operator $\mathcal{T}_i$, $i = 1, 2$ is a subset of the functional space of square integrable functions defined on the plane $\Re^2$:

$$\mathcal{T}_i : \mathcal{X} \subseteq \mathcal{L}_\in(\mathcal{D}_{\dashv\atop\surd}) \to \mathcal{T}_\rangle(\mathcal{X}) = \mathcal{Y} \subset \mathcal{L}_\in(\Re^\in),\ \rangle = \infty, \in \tag{3.2}$$

Then, the problem of phase retrieval turns into an inverse problem that amounts to determine the aperture field, E_ap, in order to satisfy eqs. 3.1. Unfortunately,

due to noise presence measured data differ from quantities M_1 and M_2. Let us indicate with $\tilde{M}_1$ and $\tilde{M}_2$ respectively the noisy data measured on Σ_1 and Σ_2. Then, the inverse problem becomes in general ill-posed as it results that:

$$\begin{cases} \tilde{M}_1 \neq M_1 = \|\mathcal{T}_1[E_{ap}]\| \\ \tilde{M}_2 \neq M_2 = \|\mathcal{T}_2[E_{ap}]\| \end{cases} \tag{3.3}$$

The problematic from the set point of view is depicted in Fig. 3.1.

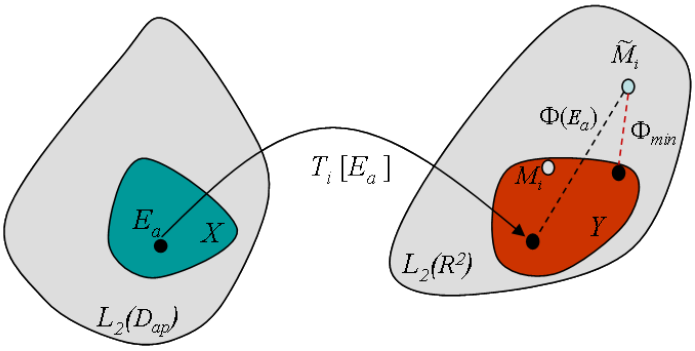

Figure 3.1: Geometrical representation of the phase retrieval problem

Hence, the problem of phase retrieval is afforded as the optimization of a proper objective functional, $\Phi(E_{ap})$. Due to the more global effectiveness in avoiding traps [90, 91], the objective functional is formulated by means of the squared amplitudes of tangential field components on the measurement surfaces, say $\tilde{M}_1^2$ and $\tilde{M}_2^2$. In particular, the objective function is given by:

$$\Phi(E_{ap}) = \sum_{i=1,2} \frac{\|\tilde{M}_i{}^2 - |\mathcal{T}_i[E_{ap}]|^2\|^2}{\|\tilde{M}_1{}^2\|^2} \tag{3.4}$$

where $\|\cdot\|$ is the usual norm in L_2.

Concluding, the phase retrieval problem amounts to minimize the functional Φ, with respect to the unknown quantity, E_{ap}. It's straightforward that the representation of the aperture field plays a key role in the optimization process as we will see in the next section.

3.2 The A-Priori Information

The phase retrieval problem is a non-linear inverse problem that suffers from ill-posedeness [83]. Furthermore, noise on measured data affects the reliability of the inversion algorithms. Indeed, the minimization process of the *quadratic* cost functional can be trapped in local minima, commonly referred as *traps*, that lead to false solution of the problem, especially when dealing with tilted beam antennas [75]. In addition, unsuited representations of the unknowns space, X, can introduce ill-conditioning, making the re-solution of the phase retrieval more complicated.

As pointed out in [93, 94], available a-priori information plays a fundamental role in the optimization, contributing significantly to reduce ill-conditioning and to the trapping problem. Accordingly, to attain reliability and accuracy in phaseless NF-FF transformation a sound formulation, residing on an effective representation of the unknown of the problem is an essential requirement. Indeed, by exploiting *at best* all the available a-priori information on the radiator and the scanning geometry it is possible to reduce the number of parameters, to be sought for, to the least possible, for a given accuracy on the near-field representation. In this way, it is possible to exclude unnecessary basis components of the unknowns-space that belong practically to the kernel of the aperture-surface transforming operators, T_i with $i = 1, 2$, mitigating ill conditioning and reducing the occurrence of local minima. Naturally, the reduction of the number of unknowns provides beneficial effects even when global optimizers are used: the considerable computational burden, that generally characterizes global approaches, can be significantly reduced.

In the general case, all the a-priori information available in NF antenna characterization concerns the following points.

I **The geometry of the radiator**: provides fundamental information about the extent and the shape of the aperture domain, D_{ap}.

II **General properties of far-field**: the FF pattern determination requires the knowledge of the PWS only in the *visible region* [96], say Ω_c, the circle in the spectral domain (u, v) of radius $\beta = 2\pi/\lambda$, being λ the wavelength (u and v being conjugate variables of x and y, respectively).

III **The geometry of the measurement**: provides information about where measurement data have been collected.

As known, the Plane Wave Spectrum (PWS) is related to the aperture field by means of a Fourier transformation relationship. Hence, according to the sec-

ond point of the above list, in order to determine the FF pattern it is necessary to take into account the visible contribute of the $\mathcal{F}$-transform of E_{ap}. On the contrary, considering the invisible part would lead to ill-conditioning: from the mathematical point of view, such components have *small* or negligible image in the range of the operators $\mathcal{T}_1$ and $\mathcal{T}_2$.

Therefore, the basis set that span the unknowns-space, should be effectively able to represent functions:

(i) with *essentially* finite spatial support, D_{ap};

(ii) whose $\mathcal{F}$-transform has *essentially* support to the visible domain.

In other words, the desired set functions constitutes a basis for band-limited (to D_{ap}) functions with support *essentially* compact (equal to Ω_c).

$$\begin{cases} f(x,y) = 0 & (x,y) \notin D_{ap} \\ \hat{f}(u,v) = \mathcal{F}_{D_{ap}}[f] \cong 0 & (u,v) \notin \Omega_c \end{cases} \tag{3.5}$$

where $\hat{f}(u,v)$ is the two-dimensional (2d) truncated Fourier transform of the aperture field:

$$\mathcal{F}_{D_{ap}}[f] = \frac{1}{(2\pi)^2} \iint_{D_{ap}} f(x,y) e^{i\cdot(ux+vy)} dxdy \tag{3.6}$$

The adopted strategy is to exploit a proper representation of the aperture field (or equivalently of the PWS) in order to incorporate in the model simultaneously information about the geometry of the radiator (point I) and the properties of FF (point II).

Let us observe that, as far as the geometry of the measurement surface (point III) is concerned, the representation of the aperture field can incorporate also the relative information content. Indeed, the basis functions of the representation could be computed by explicitly accounting for such information, but this would further burden the procedure needed for their evaluation.

Accordingly, we prefer to exploit a suited sampling strategy [95] to account for information about scanning geometry. Indeed, given the geometry of both the radiator and the acquisition surfaces, it is possible to spatially tune the sampling rate according to the *local field bandwidth* [95]. In this way, acquired data, and thus the problem model, can incorporate information about the scanning geometry as well.

Furthermore, the choice of introducing separately but simultaneously the

a-priori knowledge at point I and II in the aperture field representation and that one at point III in the measurement data constitutes a flexible and modular approach that will be crucial in the extension to the cylindrical scanning case.

3.3 The Representation of Aperture Field

Aperture field representation plays a key role in the optimization process as it can mitigate ill-conditioning, reduce both traps occurrence and computational burden of the inversion algorithm. Therefore, a significant part of the research activity, accomplished during the Ph.D. course, has been focused on this aspect. In particular, the research effort contributed to the development of an optimal representation for the aperture field, as enhancement of a sub-optimal but effective approach, developed recently at DIBET as well.

This section presents the results of the this research activity, and is articulated in sub-sections in order to make easier the reading. For sake of completeness, it is first presented the sub-optimal approach, laying the theoretical foundations for the optimal one, that is successively discussed together with an implementing numerical procedure. Some considerations about numerical features of the algorithm are pointed out and finally a comparison between the approaches is reported.

3.3.1 Prolate Spheroidal Wave Functions

Prolate Spheroidal Wave Functions (PSWFs), introduced by Slepian and Pollak [97], have the properties described by eq.3.5. PSWFs are the eigenfunctions of the truncated 1d-Fourier operator and they represent a complete basis set to span the space of band-limited function with support essentially compact. Due to their properties [98], PSWFs allows to represent with the minimum number of coefficients, given the acceptable error, a band-limited function with essentially compact support.

PSWFs have been extended to the N-dimensional case in rectangular coordinate systems [99] and, hence, also to the two-dimensional case of interest, where polar coordinates have considered [101] as well.

Therefore, it is straightforward that by exploiting PSWFs in the representation of the aperture field (or equivalently of the PWS) it is possible to incorporate in the model simultaneously information about the geometry of the radiator (point I) and the properties of FF (point II).

Let us consider the minimum rectangular domain containing D_{ap}, say

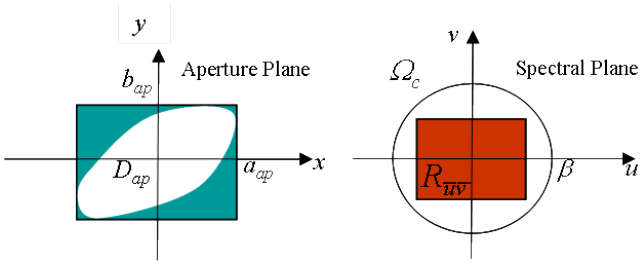

Figure 3.2: PSWFs domains

$R_{ap} = [-a_{ap}, a_{ap}] \times [-b_{ap}, b_{ap}]$ and a rectangle in the spectral domain, say $\mathbb{R}_{\overline{uv}} = [-\overline{u}, \overline{u}] \times [-\overline{v}, \overline{v}]$, that in the most general case should contain the overall Ω_c. Then, exploiting factorization, it is possible to represent the aperture field, E_{ap}, by means of 1d-PSWFs, as a function essentially defined on R_β and band-limited to R_{ap}.

$$\begin{cases} E_{ap}(x,y) = \sum\limits_{\substack{n=0 \\ m=0}}^{N,M} \dfrac{a_{mn}}{\sqrt{\lambda_n(c_x)\lambda_n(c_y)}} \Phi_n[c_x, x]\Phi_m[c_y, y] \\ \hat{E}(u,v) = \frac{1}{2\pi} \sum\limits_{\substack{n=0 \\ m=0}}^{N,M} i^{n+m} a_{mn} \sqrt{\dfrac{a_{ap}b_{ap}}{uv}} \Phi_n[c_x, \dfrac{a_{ap}}{\overline{u}}u]\Phi_m[c_y, \dfrac{b_{ap}}{\overline{v}}v] \end{cases} \tag{3.7}$$

where $\Phi_j[c_w, w]$ is the j-th one-dimensional PSWF (1d-PSWF) with *space-bandwidth product* c_w, $\lambda_j(c_w)$ is the corresponding eigenvalue, $c_x = a_{ap}\overline{u}$, $c_y = b_{ap}\overline{v}$ and the a_{nm}'s are the expansion coefficients to be retrieved in the near-field phaseless characterization from the amplitude data. Naturally, in the expansion series of eq. 3.7 only a finite number of $(N+1)\cdot(M+1)$ elements has been considered.

The use of PSWFs defined on rectangular domain does not allow to exploit completely all the information available a-priori concerning the finite extent of the aperture domain, as D_{ap} can have in general an arbitrary geometry and the aperture field can be be significantly different from zero on a subset smaller than R_{ap}. Similarly, in the spectral domain, when all the visible region is of interest, R_β takes into account a larger portion of the PWS than the needed one. In order to recover some way the amount of information, that is not possible to introduce by means of PSFWs, and accordingly make the representation more robust, projections [114] on a suited subset of the functional space spanned by PSWFs are introduced. In particular, aperture field is projected on the actual

aperture while the invisible part of PWS is filtered out, in order to eliminate all the undesired contributes.

Projector operator are, hence, given by:

$$\mathcal{P}_{D_{ap}}(x,y) = \begin{cases} 1 \ \ (x,y) \in D_{ap} \\ 0 (x,y) \notin D_{ap} \end{cases} \tag{3.8}$$

$$\mathcal{P}_{\Omega_c}(u,v) = \begin{cases} 1 \ \ (u,v) \in \Omega_c \\ 0 (u,v) \notin \Omega_c \end{cases} \tag{3.9}$$

In Fig.3.3 it is graphically illustrated the projections. It's worth noting that the

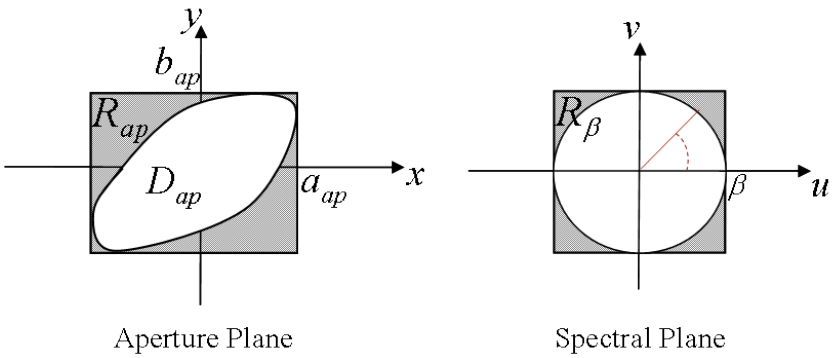

Figure 3.3: Projections of aperture field and PWS: filtered out regions (grey)

above $\mathcal{P}_{\Omega_c}$ and $\mathcal{P}_{D_{ap}}$ projects on convex subsets of $\mathcal{L}_2(R_\beta)$ and $\mathcal{L}_2(D_{ap})$, respectively. Therefore, as well known, this step affects positively the reliability of the optimization iterative algorithms [115]. Accordingly, the aperture field and the PWS can are given by:

$$\begin{cases} E_{ap}(x,y) = \mathcal{P}_{D_{ap}} \sum\limits_{\substack{n=0 \\ m=0}}^{N,M} \dfrac{a_{an}}{\sqrt{\lambda_n(c_x)\lambda_n(c_y)}} \Phi_n[c_x,x]\Phi_m[c_y,y] \\ \hat{E}(u,v) = \mathcal{P}_{\Omega_c} \frac{1}{2\pi} \sum\limits_{\substack{n=0 \\ m=0}}^{N,M} i^{n+m} a_{an} \sqrt{\dfrac{a_{ap}b_{ap}}{uv}} \Phi_n[c_x, \frac{a_{ap}}{\overline{u}}u]\Phi_m[c_y, \frac{b_{ap}}{\overline{v}}v] \end{cases} \tag{3.10}$$

It's worth noting that this approach is sub-optimal. Indeed, the optimal approach would require the development of the suited set of basis functions able to represent with the minimum number unknowns, given the acceptable error,

functions band-limited to the actual aperture and essentially supported to Ω_c. In other words, functions defined on D_{ap} with their $\mathcal{F}$-transform essentially supported to Ω_c. Due to reasons that are clarified in the following, we however refer to the projected PSWFs as the quasi-optimal approach, denoting the projected PSWFs as Quasi-optimal PSWFs(Q-PSWFs).

3.3.2 Generalised Prolate Spheroidal Wave Functions

As concluded in the previous section the optimal approach to the representation of the aperture field would employ a basis functions set able to represent *at best* PWS with support, essentially compact, equal to Ω_c and band-limited to D_{ap}. From now on, let us refer to these functions as *Generalised Prolate Spheroidal Wave Functions* (G-PSWFs).

$$\{\Upsilon_j\}_{j=1}^{\infty} \;\; Generalised\; PSWFs$$

Due to the arbitrary shape of the aperture domain, the development of these function is not trivial and only for few particular geometries can be analytically faced. [100]. Therefore, in the general case, such problem require a numerical approach.

Therefore, part of the research activities accomplished during the Ph.D. Course have been aimed at the development of G-PSWFs. In particular, it has been build up a numerical method based on a discretization of a properly truncated $\mathcal{F}$ operator and on an orthogonalization process, able to determine functions, essentially band-limited to D_{ap}, with support essentially limited to Ω_c, i.e. the G-PSWFs. The method and its underling theory is presented in the rest of the section.

The operator that is concerned is the truncated Fourier transform, say $\mathcal{F}_T$, that, crudely speaking, *relates with a Fourier transform the aperture D_{ap} to the β-circle, Ω_c*'. From mathematical point of view, it is given by:

$$\mathcal{F}_T = \mathcal{P}_{\Omega_c}[\mathcal{F}_{R_{ap}}[\mathcal{P}_{D_{ap}}]] : \; f(x,y) \in \mathcal{L}_2(D_{ap}) \rightarrow \hat{f}(u,v) \in \mathcal{L}_2(\Omega_c) \quad (3.11)$$

The first point to be addressed, when discretising an operator, concerns the representation with proper functional basis of its domain and its range. In the particular case, the operator domain is the functional set of $\mathcal{L}_2(D_{ap})$, where D_{ap} is a compact set of the plane with arbitrary geometry. Then it is straightforward to chose as basis function Q-PSWF:

$$f(x,y) \in \mathcal{L}_2(D_{ap}) => f(x,y) \cong \mathcal{P}_{D_{ap}} \sum_{h=0}^{H} s_h \Phi_h(x,y) \qquad (3.12)$$

where: $\Phi_h(x,y) = \Phi_n[c_x, x] \cdot \Phi_m[c_y, y],\ h = n(M+1) + m.$

Conversely, the PWS is vanishing outside the circle Ω_c. This naturally leads to use a PSWFs with circular symmetry. Circular PSWFs [101], say synthetically C-PSWFs, represents, indeed, the analogous of PSWFs in the case of polar coordinates in the plane. They, indeed, are the eigenfunctions of the truncated (on circles) $\mathcal{F}$ operator when polar coordinates are exploited to map spatial and spectral plane. In a manner similar to PSWFs, they are essentially supported in the spatial and spectral domain on circular, but the supports are circles.

Let us, then, consider the circle in the spatial domain circumscribing R_{ap}, say Ω_{ap} (see Fig.3.3.2). We can introduce C-PSWFs, by referring to two circles

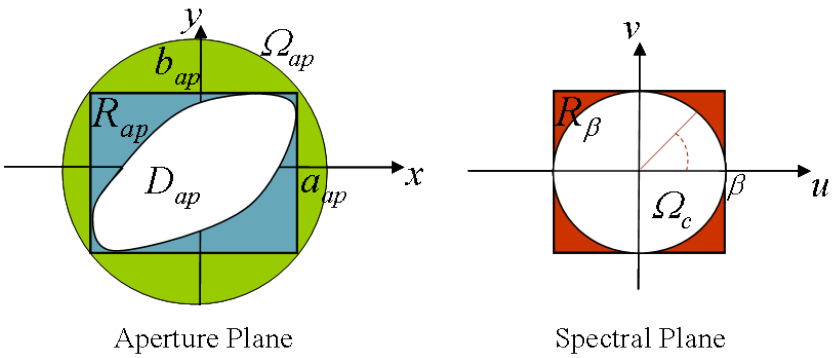

Figure 3.4: PSWFs and C-PSWF supports in both spatial and spectral domain

Ω_{ap} and Ω_c.

$$\{\Psi_k(u,v)\}_{k=0}^{\infty} \qquad Circular\ PSWFs$$

$$\Psi_k(u,v) \cong 0, \qquad (u,v) \notin \Omega_c, \quad k = 0, 1, 2, ...$$

Hence, it results:

$$g(u,v) \in \mathcal{L}_2(\Omega_c) => g(u,v) \cong \sum_{k=0}^{K} t_h \Psi_k(u,v) \tag{3.13}$$

where K is the chosen number of Circular PSWFs, given the desired accuracy of the representation. By transforming $f(x,y)$ with the $\mathcal{F}_{R_{ap}}$ it results:

$$\hat{f}(u,v) = \mathcal{F}_{R_{ap}}[f] \cong \sum_{h=0}^{H} s_h \hat{\Phi}_h(u,v) \in \mathcal{L}_2(R_\beta); \tag{3.14}$$

where: $\hat{\Phi}_h(u,v) = \mathcal{F}_{R_{ap}}[\mathcal{P}_{D_{ap}}\Phi_h(x,y)]$. The attained function is vanishing outside R_β in general.

Then, by projecting the spectrum of $f(x,y)$ on Ω_c it results:

$$\hat{f}_{P_{\Omega_c}}(u,v) = \hat{f}(u,v)\cdot\mathcal{P}_{\Omega_c} \quad \cong \quad \mathcal{P}_{\Omega_c}\sum_{h=0}^{H} s_h \hat{\Phi}_h(u,v) \in \mathcal{L}_2(\Omega_c) \tag{3.15}$$

At the same time, we are allowed to represent $\hat{f}_{P_{\Omega_c}}(u,v)$ as follows:

$$\hat{f}_{P_{\Omega_c}}(u,v) \quad \cong \quad \sum_{k=0}^{H} t_k \Psi_k(u,v) \tag{3.16}$$

From eq.3.15 and eq.3.16 it results:

$$\begin{aligned} t_k \quad &= \quad < \hat{f}_{P_{\Omega_c}}(u,v), \Psi_k(u,v) >_{\mathcal{L}_2} \\ &\cong \quad \sum_{h=0}^{H} s_h < \mathcal{P}_{\Omega_c}\hat{\Phi}_h, \Psi_k >_{\mathcal{L}_2}, \quad k = 1,2,\cdots,K \end{aligned} \tag{3.17}$$

where $< \cdot,\cdot >_{\mathcal{L}_2}$ is the usual inner-product in $\mathcal{L}_2$. Concluding, it is possible to write:

$$\hat{f}_P(u,v) \quad \cong \quad \underbrace{\sum_{h=0}^{H}\sum_{k=0}^{K} < \mathcal{P}_{\Omega_c}\hat{\Phi}_h, \Psi_k >_{\mathcal{L}_2} s_h}_{\underline{\underline{F}}\cdot\underline{s}} \cdot \Psi_k(u,v) \tag{3.18}$$

Let us define the following quantities:

$$\begin{cases} \underline{\underline{F}} = (F_{kh})_{h,k=0}^{h=H,k=K} \in \mathcal{M}_{(H+1)\times(K+1)}(\mathcal{C}), \quad F_{hk} \doteq < \mathcal{P}_{\Omega_c}\hat{\Phi}_h, \Psi_k >_{\mathcal{L}_2} \\ \underline{s} \doteq (s_1, s_2, s_3, \cdots, s_H) \in \mathcal{C}^{H+1} \\ \underline{t} \doteq (t_1, t_2, t_3, \cdots, t_K) \in \mathcal{C}^{K+1} \end{cases} \tag{3.19}$$

where $\mathcal{M}_{p\times q}(\mathcal{C})$ represents the set of matrix of dimension $p\times q$ on the complex plane, $\mathcal{C}$. It's evident that eq.3.17 can be arranged in a matrix form:

$$\underline{t} = \underline{\underline{F}} \cdot \underline{s} \tag{3.20}$$

Concluding, the operator $\mathcal{F}_T$, can be effectively represented by the matrix $\underline{\underline{F}}$.

In order to determine the G-PSWFs, it is possible to exploit a Singular Value Decomposition (SVD) procedure [102] of the discretisation of $\mathcal{F}_T$. The SVD, indeed, allows to determine the eigenvalues and the eigenvector of the matrix $\underline{\underline{F}}$ and hence the eigenfunctions of the, approximated in a finite dimensional space, operator $\mathcal{F}_T$, that represent the basis functions set we are looking for: the generalised PSWFs.

Assuming for sake of simplicity that $H \leq K$, e SVD allows to write matrix $\underline{\underline{F}}$ in the following manner:

$$\underline{\underline{F}} = \underline{V} \cdot \underline{\Lambda} \cdot \underline{U} \tag{3.21}$$

where:

$$\underline{U} = \begin{pmatrix} u_{1,1} & u_{1,2} & \cdots & u_{1,H} \\ u_{2,1} & a_{2,2} & \cdots & u_{2,H} \\ \vdots & \vdots & \ddots & \vdots \\ u_{H,1} & u_{H,2} & \cdots & u_{H,H} \end{pmatrix} \in \mathcal{M}_{H\times H}(\mathcal{C}) \tag{3.22}$$

$$\underline{\Lambda} = \begin{pmatrix} \lambda_1 & 0 & \cdots & 0 \\ 0 & \lambda_2 & 0 & \cdots \\ \vdots & \vdots & \ddots & \lambda_H \\ \vdots & \vdots & \vdots & \vdots \\ 0 & \cdots & \cdots & 0 \end{pmatrix} \in \mathcal{M}_{K\times H}(\mathcal{C}) \tag{3.23}$$

$$\underline{V} = \begin{pmatrix} v_{1,1} & v_{1,2} & \cdots & v_{1,K} \\ v_{2,1} & v_{2,2} & \cdots & v_{2,K} \\ \vdots & \vdots & \ddots & \vdots \\ v_{H,1} & v_{H,2} & \cdots & v_{K,K} \end{pmatrix} \in \mathcal{M}_{K\times K}(\mathcal{C}) \tag{3.24}$$

Rows of matrix $\underline{U}$ contain the component of the eigenfunctions in the spatial domain with respect to basis set of Q-PSWFs or equivalently the first H rows of matrix $\underline{V}$ contain the eigenfunctions components in the spectral domain with respect to the basis made of C-PSWFs.

The Generalised PSWF can be, then, expressed as follows:

$$\begin{cases} \Upsilon_j(x,y) = \sum_{h=0}^{H} u_j h\Phi_j(x,y), \quad (x,y) \in D_{ap} \\ \hat{\Upsilon}_j(u,v) = \sum_{h=0}^{K} v_j h\Psi_j(u,v), \quad (u,v) \in \Omega_c \end{cases} \qquad j = 0, 1, \cdots, H \quad (3.25)$$

Naturally, depending on the particular case the number of the required G-PSWFs, say L, can be lower than H, given the desired accuracy. Therefore, the functional basis is chosen according to the eigenvalues determined by the SVD process. A threshold values is fixed and eigenfunctions, with corresponding eigenvalues under the threshold level, are cut-off of the representation basis as their contribution can be disregarded.

Concluding, the representation of the aperture field by means of G-PSWFs is given by:

$$\begin{cases} E_{ap}(x,y) = \sum_{l=0}^{L} \Upsilon_l(x,y) a'_l \\ \hat{E}(u,v) = \sum_{l=0}^{L} \hat{\Upsilon}_l(u,v) < E_{ap}, \Upsilon_j(x,y) >_{\mathcal{L}_2(D_{ap})} \end{cases} \quad (3.26)$$

where:

$$\begin{aligned} a'_l &= < E_{ap}, \Upsilon_j(x,y) >_{\mathcal{L}_2(D_{ap})} >= \\ &= < E_{ap}, \hat{\Upsilon}_j(x,y) >_{\mathcal{L}_2(\Omega_c)}, \quad l = 0, 1, \cdots, L \end{aligned} \quad (3.27)$$

Hence, the unknowns of the problems turns to be the $L + 1\{a'_l\}_{l=0}^{L}$

3.3.3 Numerical evaluation of Generalised PSWFs

The numerical determination of Generalised PSWFs can be summarised in the following steps:

i The generation of 2d-PSWFs essentially supported to $\mathbb{R}_\beta$ and to R_{ap} in the spectral and spatial domain, respectively.

ii The generation of C-PSWFs essentially supported to Ω_c and in the spectral and spatial domain, respectively.

iii The evaluation of matrix F

iv The singular value decomposition of T

Due to factorization, 2d-PSWFs can be easily calculated by means of 1d-PSWFs. Indeed, factorization allows to generate the required set of functions with two sets of 1d-PSWFs of reduced cardinality. Therefore, 2d-PSWFs can be evaluated with a good accuracy and a low computational burden [97].

On the contrary, factorization is not possible in polar coordinate and all the C-PSWFs needed must be singularly determined. According to [101] the evaluation of C-PSWFs requires the numerical computation of Jacobi polynomials [103]. Indeed, C-PSWFs can be approximated as follows:

$$\Upsilon_{J,p}(\rho,\theta) \;=\; i^J(-1)^p\sqrt{\frac{1}{2\pi qr}}\psi_{J,p}(\rho/q)e^{iJ\theta} \tag{3.28}$$

with:

$$\phi_{J,p}(\xi) \;=\; \sum_{l=0}^{\infty} d_l^{J,p}(q)\xi^{J+\frac{1}{2}}\frac{J!l!}{(J+l)!}P_l^{(J,0)}(1-2\xi^2) \tag{3.29}$$

where (ρ,θ) is a polar coordinate system in the spectral domain, q is the space-bandwidth parameter in the circular case, $P_l^{J,0}$ is the l-th Jacobi polynomial of order $(J,0)$ and $d_l^{J,p}(c)$ are suited coefficient satisfying a recurrence relationship as shown in [101].

Naturally, in practical applications summation in eq.3.28 must be properly truncated over a finite number of terms. However, in order to obtain the necessary accuracy even when dealing with with low index C-PSWF, a significant number of terms, and hence of Jacoby polynomials, are required to represent the C-PSWF. The situation can become problematic when the index of C-PSWFs increases: factorial terms and the power order of the polynomials involved in the summation increases and accordingly the accuracy of conventional numerical procedures for their evaluation reduces. This implies that accuracy of the overall C-PSWFs computation decreases with the index of the function.

In many cases of practical interest for our applications, number of C-PSWFs needed is typically high (~ 100). Unfortunately, these imply that the accuracy of the evaluation of C-PSWFs of high index can be significantly degraded, unless accurate numerical procedure are exploited. Therefore, point (ii) of the numerical procedure can be a critical one and can affect the overall

process.

As far as point (iii) is concerned, it's quite straightforward that it is not problematic, given an accurate evaluation of C-PSWFs. It, indeed, involves only the computation of inner-product, i.e. discretized integrals.

Concluding, SVD at point (iv), do not represent an issue, as effective numerical algorithms are currently available [104].

3.3.4 Comparison Between Aperture Field Representation

The use of G-PSWFs represents the optimal approach to the representation of the aperture field. However, as pointed out in the previous section, this approach requires accurate end effective numerical procedures to evaluate the expansion functions, as the accuracy of conventional ones can be reduced. Accordingly, a preliminary significant numerical effort could be needed to exploit the phase retrieval algorithm. In many cases, the sub-optimal (Q-PSWFs) approach, which does not suffer of numerical issues pointed out for G-PSWFs, can provide the required accuracy and reliability for the pattern estimate [74, 75]. This naturally leads to the questions of how much close are the two representations.

. The problem of comparing representations essentially amounts at calculating the *distance* between the sub-space spanned by the Q-PSWFs and that spanned by the G-PSWFs. Such a problem can be addressed by using the concepts of principal angles and of angle between subspaces [105], commonly exploited to evaluate the nearness of two subspaces as illustrated in [105].

To this end, given two subspaces, V_1 and V_2, let us define, as usual, by $\theta_k(V_1, V_2)$ the k-th principal angle between V_1 and V_2, and by $\theta = \max_k \theta_k(V_1, V_2)$ the angle between V_1 and V_2. Furthermore, let us define as V_G=Span{G-PSWFs}, V_Q=Span{Q-PSWFs}, V_R=Span{R-PSWFs}, and V_S=Span{sinc}, i.e. the sinc functions associated to the standard sampling rate, and restricted to those having maximum in Ω_c [106]. For sake of completeness, also sinc functions have been considered as they are usually dealt with in phaseless approaches [[64, 66].

From numerical and experimental results we expect that $\theta(V_G, V_Q) < \theta(V_G, V_R)$ and that $\theta(V_G, V_Q) < \theta(V_G, V_S)$. In other words, we now point out the role of the projections 3.8 in drawing the subspace V_Q close to V_G.

To this purpose, let us consider a square aperture with $D_{ap} = [-7\lambda, 7\lambda] \times [-7\lambda, 7\lambda]$ and the entire visible region,Ω_c. In this case, the number of G-PSWFs is $P = 484$. In Fig. 3.3.4, the cosines of the principal angles $\cos[\theta_k(V_G, V_Q)]$ (solid line), $\cos[\theta_k(V_G, V_R)]$ (dashed line), $\cos[\theta_k(V_G, V_S)]$

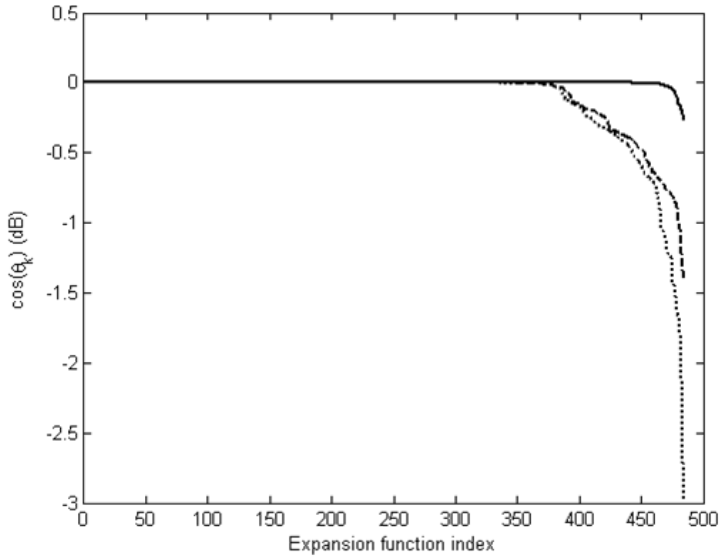

Figure 3.5: Cosines (in dB) of the principal angles between V_G and V_Q (solid line), between V_G and V_R (dashed line), and between V_G and V_S (dotted line).

(dotted line) are illustrated in a dB scale. The values of $\cos(\theta_k)$ have been accurately evaluated by the procedure devised in [34]. As it can be seen, $\theta(V_G, V_Q) = 14^\circ$, $\theta(V_G, V_R) = 31^\circ$, and $\theta(V_G, V_S) = 44^\circ$. It is worth noting also that $\theta(V_G, V_R) < \theta(V_G, V_S)$. Therefore, we expect that, when ill-conditioning and trapping problem are not critical, the use of the Q-PSWFs provides similar performances if compared to the optimal G-PSWFs, with a dramatic reduction of the effort needed for an accurate computation of the expansion functions.

Hence, projected PSWFs are very close to set of the optimal ones, among those one considered. That is why they have been referred to as quasi-optimal.

3.4 Representation of the Near Field Data

The sampling strategy of the near field radiated on the acquisition surfaces is another key aspect of the considered solving approach of the phase retrieval

problem. It, indeed, allows to explicitly account for the information related to the scanning geometry.

According to [95], any component E-field of the near-field on either Σ_1 or Σ_2 can be sampled at the non-uniformly spaced points:

$$x_{r,i} = x_{r,i}(\Delta\xi) = \frac{4a_{ap}}{\pi} r\Delta\xi \sqrt{\frac{r\Delta\xi)^2 - \pi^2 \frac{a_{ap}^2 + d_{s,i}^2}{a_{ap}^2}}{(r\Delta\xi)^2 - \pi^2}} \tag{3.30}$$

and

$$y_{s,i} = y_{s,i}(\Delta\eta) = \frac{4b_{ap}}{\pi} s\Delta\eta \sqrt{\frac{s\Delta\eta)^2 - \pi^2 \frac{b_{ap}^2 z_{s,i}^2}{b_{ap}^2}}{(s\Delta\eta)^2 - \pi^2}} \tag{3.31}$$

where the subscript i indicates the i-th measurement surface, with $i = 1, 2$, χ is a *bandwidth enlargement factor* controlling the approximation error, and:

$$\begin{cases} \Delta\xi = \pi/(\chi W_\xi), \quad W_\xi = 4 * a_{ap}/\lambda \\ \Delta\eta = \pi/(\chi W_\eta), \quad W_\eta = 4 * b_{ap}/\lambda \\ d_{s,i} = \begin{cases} z_i, \ |y_{s,i}| \leq b_{ap} \\ \sqrt{z_i^2 + (y_{s,i} - b_{ap})^2} \end{cases} \end{cases}$$

The corresponding non-uniform sampling representation of the complex near-field on the i-th surface, say $E_i(x, y)$, is provided by:

$$\begin{aligned} E_i(x,y) = e^{-i(\gamma_\xi(\xi)+\gamma_\eta(\eta))} \sum_{r,s} \{ & E(x_{rs}, y_s) \cdot \\ & e^{i(\gamma_\xi(\xi_r)+\gamma_\eta(\eta_s))} T[\xi - \xi_r] T[\eta - \eta_s] \cdot \\ & sinc[\frac{\pi}{\Delta\xi}(\xi - \xi_r)] sinc[\frac{\pi}{\Delta\eta}(\eta - \eta_s)] \} \end{aligned} \tag{3.32}$$

where $R_1(x)$ and $R_2(x)$ are defined in Fig.3.4, $T(\cdot)$ is a suitable windowing function controlling the truncation error, and:

$$\begin{cases} \gamma(x) = \beta/2[R_1(x) + R_2(x)] \\ \xi(x) = \beta/(2W_\xi)[R_1(x) + R_2(x)] \end{cases}$$

The non-uniform sampling rate depends on the local field bandwidth [95] that in turns is strictly related to the geometrical properties of the radiator and on the acquisition domain.

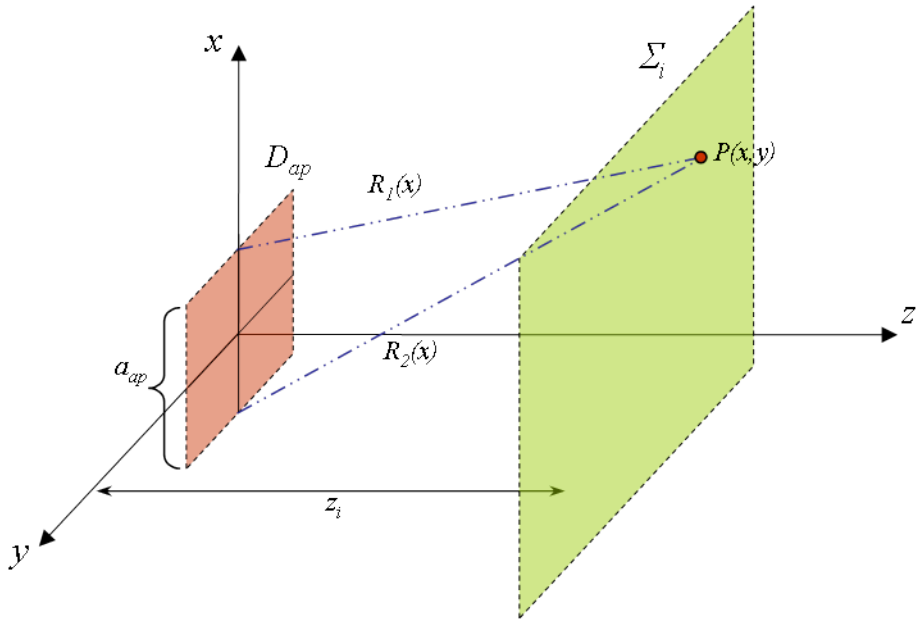

Figure 3.6: Relevant of the sampling strategy

As the squared amplitudes of the near-field is concerned in the measurement, it is necessary to taking into account that the bandwidth is twice the bandwidth of the field. Therefore, the measured data is represented by:

$$\begin{aligned} |E_i(x,y)|^2 = \quad & \sum_{r,s} \{|E(x_{rs}^{SQ}, y_s^{SQ})|^2 T[\xi - \xi_r^{SQ}] T[\eta - \eta_s^{SQ}] \cdot \\ & sinc[frac\pi\Delta\xi^{SQ}(\xi - \xi_r^{SQ})] \cdot \\ & sinc[frac\pi\Delta\eta^{SQ}(\eta - \eta_s^{SQ})]\} \end{aligned} \tag{3.33}$$

where:

$$\begin{cases} \xi_r^{SQ} = r\Delta\xi^{SQ} \\ \eta_s^{SQ} = r\Delta\eta^{SQ} \\ \Delta\xi^{SQ} = \Delta\xi/2 \\ \Delta\eta^{SQ} = \Delta\eta/2 \end{cases}$$

Concluding, the field squared amplitudes acquired on the measurement surfaced can be represented by samples collected on the irregularly spaced points $(x_{rs,i}^{SQ}, y_{s,i}^{SQ})$, with $x_{rs,i}^{SQ} = x_{rs,i}(\Delta\xi/2)$ and $y_{s,i}^{SQ}) = y_{s,i}(\Delta\eta/2)$. It is worth pointing out that the application of non-uniform sampling, is tantamount to

filtering out, from the near-field, some of the noisy contributions due to the unwanted reflections and diffractions coming from points outside the aperture D_{ap} (environmental clutter) [107, 108]. Further, we observe that the measurement strategy presented above is easy to be implemented and dramatically reduces the measurement points and, thus, the measurement time, a key point in the millimetre and the sub-millimetre frequency ranges [109].

3.5 Phase Retrieval in The Planar Case

Previous section have discussed aspects related to the representation of the aperture field and the measurement data, illustrating the adopted solutions. On the basis of these considerations we want now to present the algorithm developed for phase retrieval in the planar case.

For sake of commodity, the geometry of the problem in the planar case is here reminded with Fig.3.5 Based on the expansions in eq. 3.10 (Q-PSWFs)

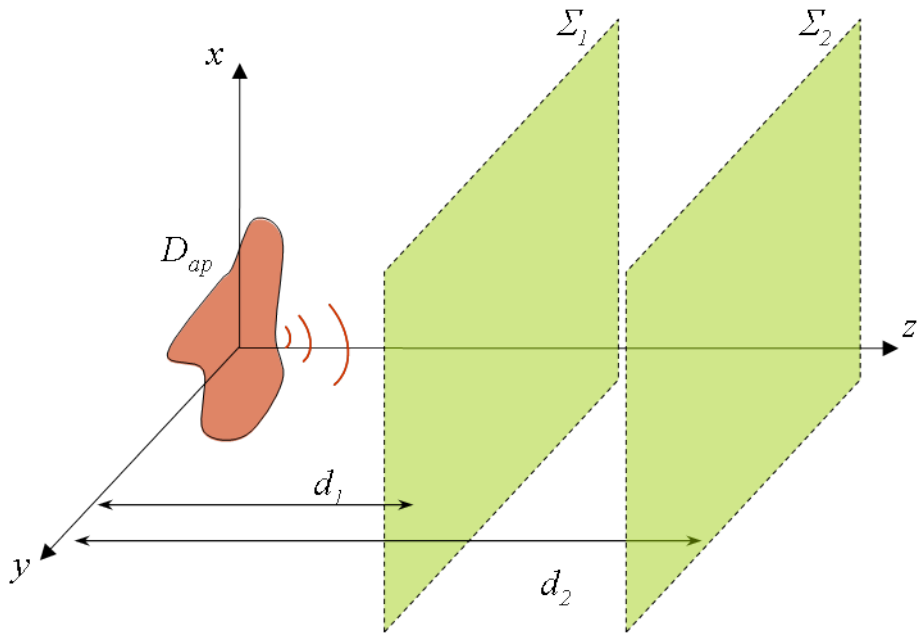

Figure 3.7: Geometry of the problem: planar case

or eq. 3.26 (G-PSWF) and on the near-field squared amplitude values measured on the irregular grid of points $(x_{rs,i}^{SQ}, y_{s,i}^{SQ})$, with $i = 1, 2$, on Σ_1 and Σ_2,

the proposed algorithm amounts to estimate the unknown coefficients anms (or equivalently the a_l's), then the PWS from eq.3.7 (or equivalently from eq. 3.26), and, finally, the far-field pattern from the well known relationship between the PWS and the AUT far-field [110].

The a_{nm}'s (or equivalently the a_l''s) must be such that the squared amplitude of the corresponding theoretical near-fields on Σ_1 and Σ_2 are as close as possible to the measured data. Let us denote by $\underline{\underline{a}}$ the matrix (or equivalently the vector) of the unknowns. From eq.3.4 it results that:

$$E_i(x,y) = \mathcal{T}_i[E_{ap}(x,y,\underline{\underline{a}})] = \mathcal{F}_{\Omega_c}^{-1}[[E_{ap}(x,y,\underline{\underline{a}})e^{-i\beta z_i}], \;\; i=1,2 \quad (3.34)$$

In eq.3.34 it has been explicitly indicated the dependence of E_{ap} from the unknowns $\underline{\underline{a}}$ Then, by recalling eq.3.4 $\underline{\underline{a}}$ is obtained by minimizing the objective functional:

$$\Phi(\underline{\underline{a}}) = \sum_{i=1}^{2} \frac{\|\tilde{M}_i^2(x,y) - |E_i(x,y,\underline{\underline{a}})|^2\|^2_{\mathcal{L}(\Sigma_i)}}{\|\tilde{M}_i^2(x,y)\|^2_{\mathcal{L}(\Sigma_i)}} \quad (3.35)$$

Since the objective functional 3.35 to be optimized is an algebraic polynomial of the fourth order, the conjugate gradient method of Polak and Ribière, suited for the case at hand, is exploited [112]. At each step of the iterative procedure, the integrals concerning the norms involved in the evaluation of the objective functional 3.35 and the scalar products needed for its gradient computation require estimates of the complex (i.e., amplitude and phase) near-field $E_i(x,y),\; i=1,2$, as well as of $\tilde{M}_i^2(x,y),\; i=1,2$, over a grid G of (x,y) coordinates with a proper sampling step. To this end, starting from the knowledge of the a_{nm}'s,$E_i(x,y),\; i=1,2$, is firstly estimated over the non-uniform grid (x_{rs},y_s). Subsequently, the complex near-field is evaluated over the regular grid G by exploiting eq. 3.32, which amounts at an interpolation formula. To save computer time, because this interpolation is required at each step, a traveling sampling approach [113] is exploited. As pointed out in [76], this strategy is convenient for filtering purposes, having beneficial effects on the quality of the reconstructions.

Similarly, the values of $|E_i(x,y)|^2,\; i=1,2$, over G are obtained, once at a time, at the beginning of the iterative procedure needed to minimize Φ, by applying the interpolation scheme given by eq. 3.32.

A flow chart summarizing the main steps of the algorithm is reported in Fig. 3.5.

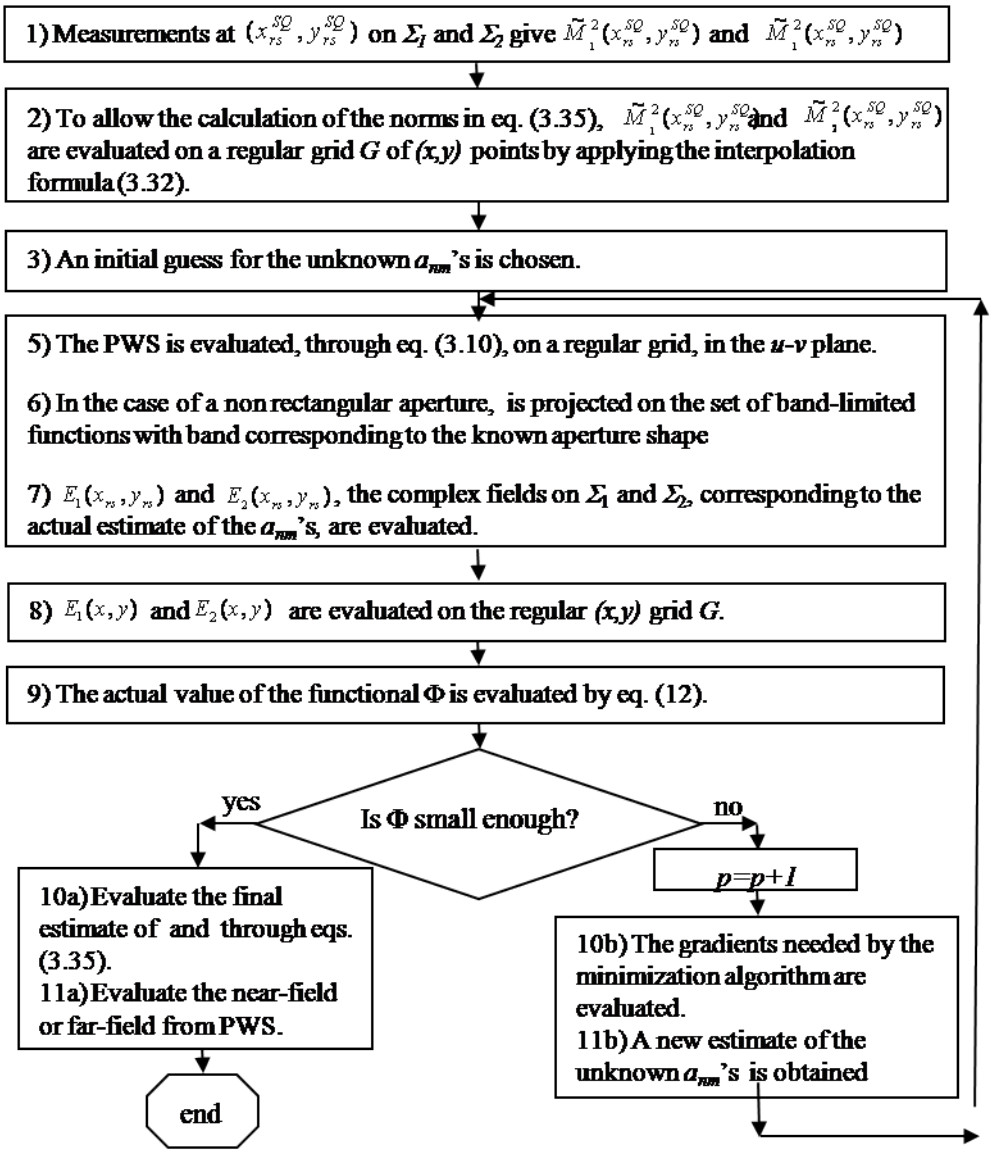

Figure 3.8: Geometry of the problem: planar case

3.6 Phase Retrieval from Data with Mild Incoherency

A problematic that, typically, affects overall antenna characterization is the alignment of devices[116]. Indeed, even when sophisticated equipments, such as theodolites or laser pointers, are employed in the measurement set-up, the accuracy of the alignment between AUT and probe essentially depends on the human eye sensitivity. Therefore, a small residual error can occur and affect the measurement. Naturally, when dealing with phaseless characterization, two measurement surfaces are required and the possibility of incoherency between the surfaces can become more probable.

Sometimes, when the radiated beam have symmetry properties, a visibly rough alignment is rapidly accomplished and then tuned by exploring small region around the symmetry axis of the pattern with oversampled acquisitions. However, this strategy is not applicable in the general case and even when possible the presence of noise on data can affects the alignment.

In the case of planar geometry, the theoretical modelling assumes that scanning planes are parallel and both concentric with the aperture. Typically, the commercial NF facilities, provides accurate positioning systems and hardware mounts, that hardly engage AUT and probe ensuring that aperture plane and plane of acquisition are parallel. Therefore, only centring of surfaces is reminded to the the operator. Hence, relative offsets between the measurement surfaces and the aperture can occur. From now on let us refer to the case of data acquired on planar surfaces with a relative offset errors as *incoherent* data.

Naturally, phase retrieval from incoherent data can affect the FF pattern estimate. In particular, the beam pointing direction can be erroneously determined. Indeed, from the point of view of intuition, it is easy to understand that the beam pointing will tend to the direction, connecting the positions of the points on the measurement planes, where the relative maximum field amplitude value is attained. Therefore, if the position is affected by an offset error, the estimate of the pattern is accordingly altered.

For sake of simplicity, let us assume that the first surface is correctly centred while the second presents a small centring offset. It's worth noting that this assumption, practically, does not affect the generality of the problem. In Fig.3.6 it is schematically depicted the geometry of the problem. Let us, then, introduce the offset vector $\underline{v} \doteq (x_0, y_0)$ (see 3.6), that represent the relative misalignment of surfaces Σ_1 and Σ_2 in the Oxy plane. We want now to show how the phase retrieval model, above presented, can be modified in order to become more robust against mild incoherence of data.

The presence of an offset in one surface can be modelled as a unknown

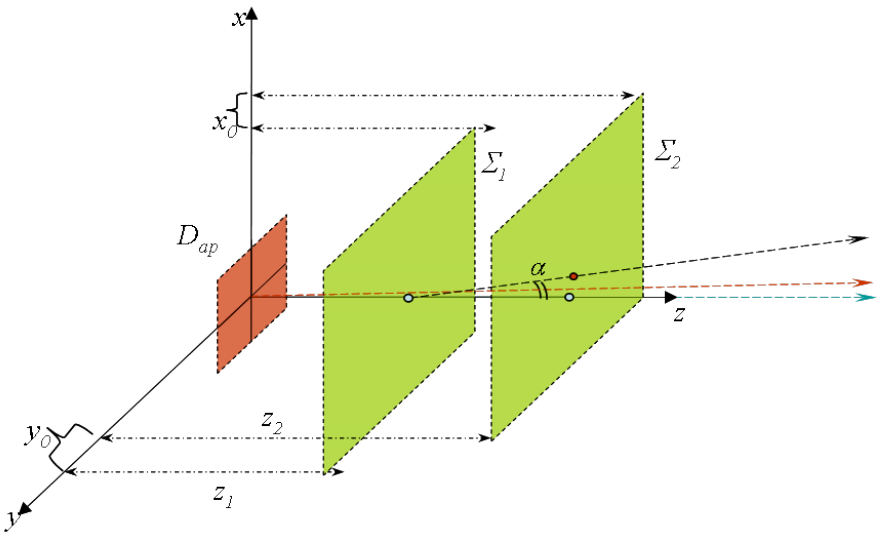

Figure 3.9: Incoherency of measurement planes: correct maximums position (blue circles), erroneous maximums positions (red circles), correct beam pointing direction (blue dashed arrowed line), erroneous beam pointing direction(red dashed arrowed line)

spatial translation that centre the reference system Oxy with the centre of the reference system, $O'x'y'$, on second aperture. Accordingly, the aperture field is given by:

$$\begin{cases} x' = x - x_0 \\ y' = y - y_0 \\ E_{ap}(x', y') = E_{ap}(x - x_0, y - y_0); \end{cases} \tag{3.36}$$

Naturally, this spatial translation amounts to linear phase terms in the PWS:

$$\begin{aligned} \mathcal{F}[E_{ap}(x', y')](u, v) &= \mathcal{F}[E_{ap}(x, y)](u, v) \cdot e^{-i(x_0 u + y_0 v)} \\ &= \hat{E}(u, v) e^{-i(x_0 u + y_0 v)} \end{aligned} \tag{3.37}$$

Then, operators $\mathcal{T}_i,\ i = 1, 2$ of eq.3.34 becomes parametric and are given by:

$$\mathcal{T}_i[\cdot, \underline{v}] = \mathcal{F}_{\Omega_c}^{-1}[\mathcal{F}[\cdot] e^{-i(x_0 u + y_0 v)} e^{-i\beta z_i}], \quad i = 1, 2 \tag{3.38}$$

Accordingly, functional Φ expressed in 3.35 is given by:

$$\Phi(\underline{\underline{a}}, \underline{v}) = \sum_{i=1}^{2} \frac{\|\tilde{M}_i^2(x,y) - |\mathcal{T}_i[E_{ap}(x,y,\underline{\underline{a}}), x_0, y_0|^2\|^2_{\mathcal{L}(\Sigma_i)}}{\|\tilde{M}_i^2(x,y)\|^2_{\mathcal{L}(\Sigma_i)}} \tag{3.39}$$

An initial guess is assumed for the parameter $\underline{v}$. Then the minimization of the 3.39 is faced by means of a two-stage optimization strategy for each step of iteration, in a fashion similar to alternate projections. Indeed, in the first stage $\underline{v}$ is fixed and unknowns $\underline{\underline{a}}$ are updated by means of the procedure described in section 3.5, then, in a second stage unknowns are fixed and parameter $\underline{v}$ is optimized.

3.7 Phase Retrieval In The Cylindrical Case

The cylindrical scanning geometry allows measuring completely around the radiator (see Fig.3.7), providing a reduction of the truncation error.Therefore, this scanning geometry does not comply with the aperture modelling because of the radiation symmetry along the y axis that the planar source exhibits. An optimal approach, indeed, would require that a proper ellipsoidal surface, enclosing the radiator, should be considered and a set of spheroidal prolate functions, defined on the ellipsoid to represent equivalent currents. However, it is possible to limit the angular range of the scansion in order to collect field data in only one semi-space in order to avoid the symmetry issues. This allows to extend the mathematical framework to the cylindrical scanning geometry as well. Naturally, in order to completely enclose the radiator, it is possible to collect NF intensities on the overall angular domain and process separately data coming from the two different semi spaces.

Let us, then, refer only to the positive y axis and introduce a two cylindrical acquisition surfaces Π_1 and Π_2, whose radii are r_1 and r_2, respectively. Let us also introduce an equivalent planar aperture domain D_{ap}, parallel to plane $0xy$ but spaced a distance d in y axis from the Oxy plane. This spacing is necessary to take into account the fact that the actual aperture of the antenna cannot lye on the rotation axis of the scanning system. Fig.3.7 shows a top view of the considered geometry. A polar reference system, (r, ϕ) has been introduced in the plane Oxy.

By restoring in the the cylindrical geometry the presence of an planar source aperture, all the considerations about the representation of the aperture field presented in the planar case can be similarly repeated. In particular, to incorporate in the modelling all the a-priori information related to the geometry

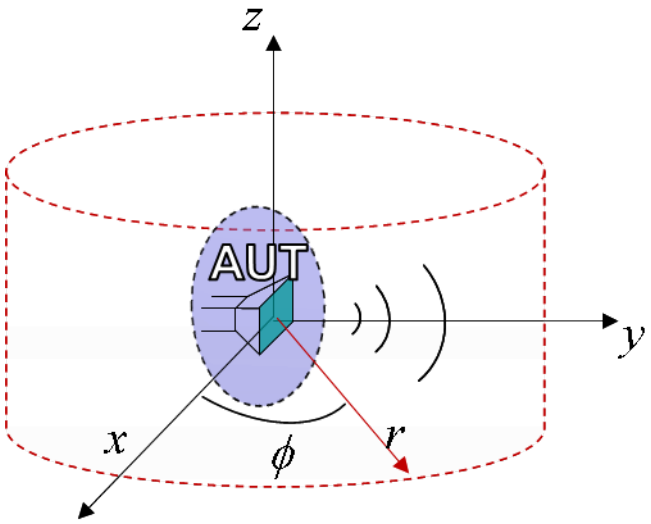

Figure 3.10: Geometry of Cylindrical Case

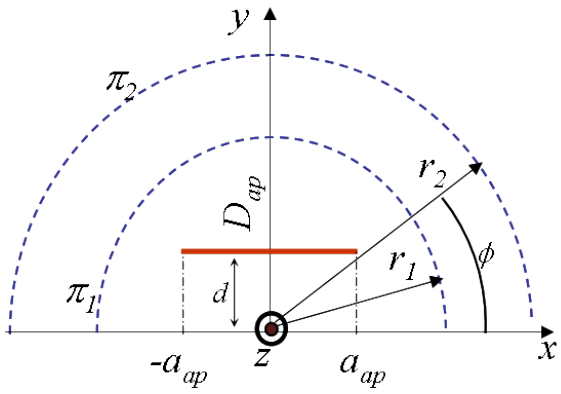

Figure 3.11: Top view of the cylindrical geometry

of the radiator (point I in section 3.2)and the general properties of the FF (point II in section 3.2), the representation of the E_{ap} can be realised by means of Q-PSWFs or (eventually by means of G-PSWFs). Accordingly, the unknowns of the problem turns to be again the expansion coefficients a_{nm}'s defined in refeqIII.10. Concerning the scanning geometry, as in the planar case, the field data can be collected by means of a proper sampling strategy [95] in order to

introduce the relative information.

The last point to be addressed in order to extend the mathematical model to the cylindrical case concerns the operator, say $\mathcal{T}_i,\ i = 1, 2$, that allows to evaluate fields on the cylindrical surface $\Pi_i,\ i = 1, 2$ from the aperture field. To this purpose, it has been exploited once again the PWS and the $\mathcal{F}$ transform operator. Let us denote the sampling points on the i-surface with $P_pq = (r_i, \phi_p, z_q)$, we indeed can define: by defining.

$$\mathcal{T}_i : E_{ap} \in \mathcal{L}_2(D_{ap}) \rightarrow E_i(x, y, z) \in \mathcal{L}_2\Pi_i,\ \ i = 1, 2 \quad (3.40)$$

$$\mathcal{T}_i[E_{ap}](r_i, \phi_p, z_q) = calF^{-}_{\Omega_c}1[\mathcal{F}_{D_{ap}}[E_{ap}]e^{-i(ur_i\cos(\phi_p)+vr_i\sin(\phi)_p+\beta z_q)}] \quad (3.41)$$

Accordingly, the functional 3.35 becomes:

$$\Phi(\underline{\underline{a}}) \quad = \quad \sum_{i=1}^{2} \frac{\|\tilde{M}_i^2(r_i, \phi_p, z_q) - |\mathcal{T}_i[E_{ap}(\underline{\underline{a}}](r_i, \phi_p, z_q)|^2\|^2_{\mathcal{L}(\Phi_i)}}{\|\tilde{M}_i^2(r_i, \phi_p, z_q)\|^2_{\mathcal{L}(\Phi_i)}} \quad (3.42)$$

3.8 Phaseless Antenna Characterization: Experimental Result

The formulation based on the criteria pointed out in sections 3.3 and 3.4 may be successfully exploited in difficult situations, as those involving tilted-beam radiators. We now wish to show that the recent developments put phase-less near-field characterization in a position to deal with antennas having radiating behaviours never considered until now, also making the performance of this approach close to that of standard near-field/far-field transformations. To this end, we present experimental results concerning two different test benchmarks.

The first test is a tilted-beam reflectarray designed at the Antenna Lab of the DIBET. The reflectarray has been designed to radiate a pencil beam with a pointing angle of about 20° from the broadside direction. This pointing angle is equal to the angle already considered in [118, 119], where the problem of characterizing steeredbeam antennas has been raised.

The second test is a phased array, designed and realized by SELEX Sistemi Integrati S.p.A. It radiated scanned beams with tilt angles up to approximately 25° [120]. This antenna is an ideal test for discussing the accuracy and the reliability of phase-less near-field characterization because:

- It is an operating array, actually employed in real-world applications;
- It is of large electrical size;

- It radiated both broadside and tilted beams, with maximum beam tilt even larger than that considered until now [118, 119].

3.8.1 Experimental Results: The Reflectarray Case

The reflectarray considered has a working frequency of $14.15GHz$. It is made up of 20x20 patches, arranged on a regular grid, with step size of 0.62λ along both the x and y axes, so that the overall physical aperture size is 122λ x 122λ. The patches were printed over an Arlon DiClad 870 substrate, having a dielectric permittivity equal to 2.33, a thickness of $1.524mm$, and a dielectric loss tangent of 0.0013. The feeding antenna is a Ku-band pyramidal horn antenna, mounted in an offset configuration at a distance of about 20λ from the aperture plane.

The indoor environment wherein the field measurements for the reflectarray has been performed is the anechoic chamber, designed and realized by MI Technologies, for the Antenna Lab of DIBET, Università di Napoli Federico II. The environment, of size $8m$ x $5m$ x $3.5mn$ (length x width x height), has been set up to work in the $900MHz$ to $40GHz$ frequency band. The chamber has ben equipped with a planar scanner, made up of two orthogonal linear positioners, allowing a maximum scanning area of $180cm$ x $180cm$, and driven by an external controller, MI-4190. All of the operations in the chamber were controlled by a PC, which has been equipped with proprietary software to drive the measurements and to work out standard near-field/far-field transformations.

For the measurements described, the non-uniform acquisition strategy has been implemented using a customized program, written in Visual Basic and exploiting the primitives and the software libraries made available from MI Technologies.

A VNA, Anritsu 37397C, working in the $40MHz$ to $65GHz$ frequency band, and also providing phase measurements for the near field, has been employed. This allowed a comparison between the phase-less characterization and the standard near-field/far-field transformation. During the data acquisition a standard open-ended waveguide has been employed as a probe antenna.

The squared-amplitude near-field samples required by the phase-less characterization algorithm has been collected on two planar surfaces, S_1, and S_2 of size 56.6λ x 66λ each. These has been located on the planes $z_1 = 30\lambda$ and $Z_2 = 50\lambda$, and they have hosted 53 x 57 and 39 x 43 sampling points, respectively. It is worth noting that due to the tilt of the radiated beam, the acquired near-field maps presents a significant truncation (of approximately -10 dB, be-

low the maximum) over the upper regions of both the near-field surfaces, S_1, and S_2. The amplitude and phase near-field samples needed for the standard near-field/far-field transformation have been acquired over S_1 at a sampling step of $\lambda/2$. For the phase-less characterization, the domain R_{ap} (see section 3.3) has been assumed to be a rectangle as large as 13.7λx13.7λ. The reconstruction algorithm has been rum by exploiting an expansion of the aperture field involving 484 unknowns. The starting point has been obtained by back-propagating a constant-phase field, the amplitude of which was equal to the measured field's amplitude, from the first scanning surface (S_l) to the aperture plane. Remarkably, again due to the tilt of the radiated beam, the phase distribution over S_1 is far from being constant, so that the chosen starting point is far from the actual solution. The estimated far-field (red solid line) and the reference field (blue dashed line) obtained by the standard near-field/far-field technique, evaluated on a cut parallel to the v-axis and passing through the direction of maximum far-field intensity, are shown in Figure 3.8.1

3.8.2 Experimental Results: The Phased Array Case

The planar phased-array radiated scanned beams with tilts ranging between approximately -15° and 25° with respect to the broadside direction. The amplitude and phase near-field data have been acquired by SELEX Sistemi Integrati S.p.A. during a former campaign, aimed at characterizing the radiating behaviour of the AUT with a standard near-field/far-field transformation technique. The only scanning plane considered has been set at a distance of $z = 5\lambda$, and uniform sampling with a sampling step of 0.42λ have been applied along each scanning axis.

In order to evaluate the performance of the phase-less NFFF transformation, the data acquired over the measurement plane at $z = 5\lambda$ have been synthetically re-sampled to a nonuniform grid. Moreover, the uniform acquisitions have been used to synthetically generate the data needed for the phase-less characterization over the second scanning plane, chosen at a distance of 11λ from the aperture plane. In order to make the test as realistic as possible and to decorrelate the noise over the two surfaces, the data over the first and second scanning surfaces have been corrupted by noise with a signal-to-noise ratio of $30dB$. The domain R_{ap} (see section 3.3)has been chosen as large as the physical aperture, but enlarged by 1λ along each border. Following this choice, the overall number of unknown parameters searched for during the phase-less characterization procedure has been 1027. The starting point was constructed by using the same criterion exploited in the reflectarray test case.

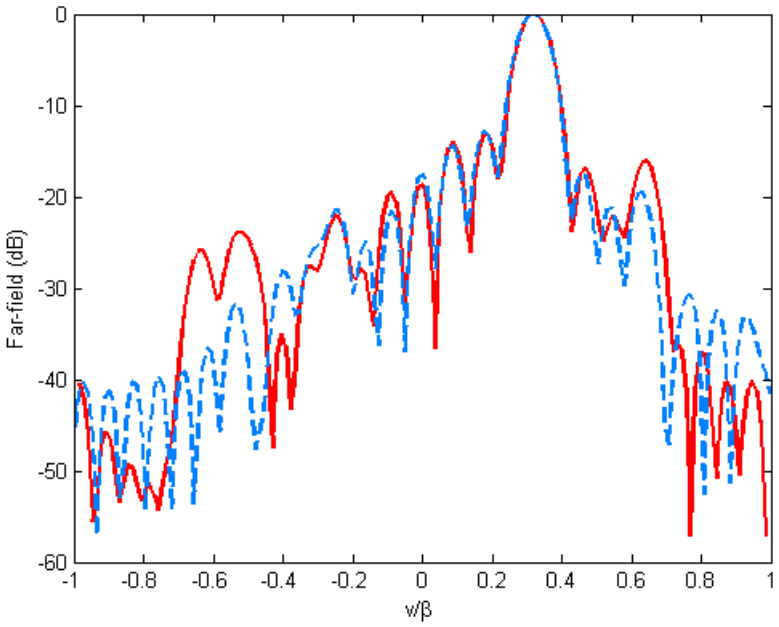

Figure 3.12: The tilted-beam reflectarray: (red solid line) the far field reconstructed by the developed approach; (blue dashed line) the far field reconstructed by the standard NF-FF transformation.

The estimated far-field (solid line) and the reference field (dashed line) obtained by the standard near-field/far-field technique, evaluated on cuts parallel to the v-axis and passing through the directions of maximum far-field intensity, are shown in Figures 3, 4, and 5 for the cases of the broadside beam, and the scanned beams with tilt angles of approximately -15° and 25°, respectively. The plots in such figures have been centred on the respective main beams of the far-field pattern, whereas the beams are represented over intervals with randomly chosen widths, different from Fig. 3.8.2 to Fig. 3.8.2.

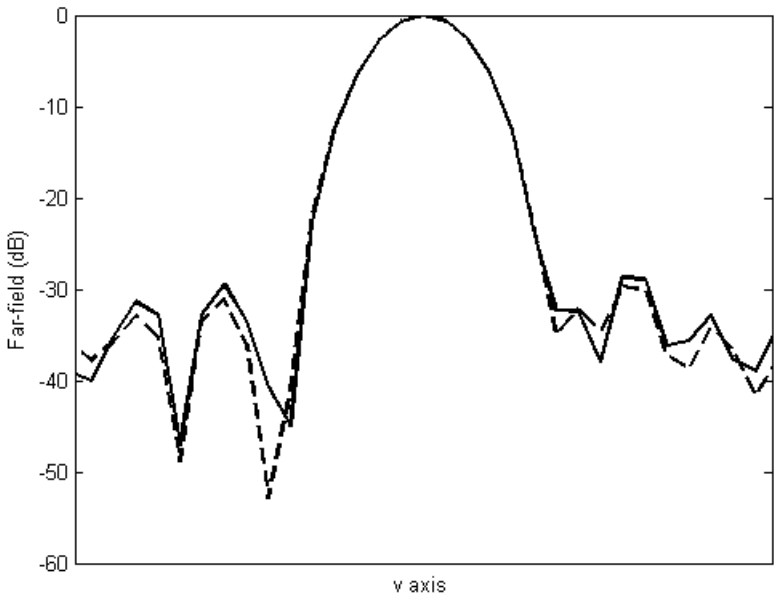

Figure 3.13: The scanned-beam phased array, for a broadside beam.: (solid fine) the far field reconistructed by the developed approach; (dashed line) the far field reconstructed by the standard NF-FF transformation.

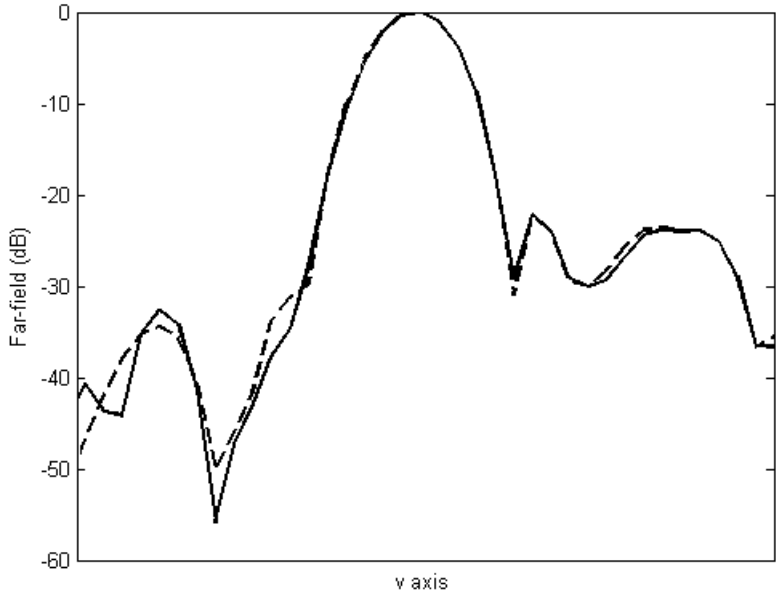

Figure 3.14: The scanned-beam phased array, for a beam with a tilt of approximately -150: (solid line) the far field reconstructed by the developed approach; (dashed line) the far field reconstructed by the standard NF-FF transformation.

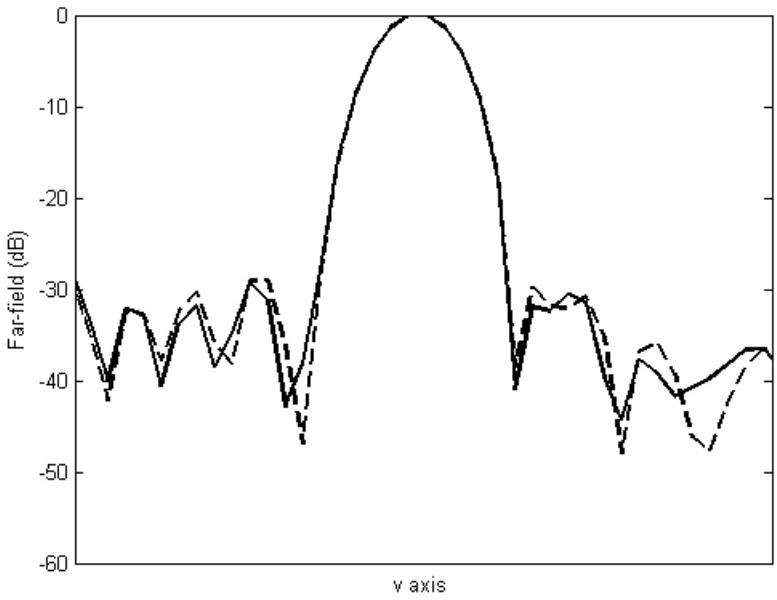

Figure 3.15: The scanned-beam phased array, for a beam with a tilt of approximately 25": (solid line) the far field reconstructed by the developed approach; (dashed line) the far field reconstructed by the standard NF-FF transformation..

Chapter 4

Compact, Fast and Very NF Antenna Characterization

The innovative characteristics of photonic probes and accurate and reliable algorithms for antenna characterization are now going to revolutionize NF testing facilities.

Thanks to their limited size, essentially dielectric nature and fully non-metallic (i.e. fiber optics) connections, photonic probes represent small, lightweight, non-invasive field sensors, capable to be hold by a non-perturbing dielectric structure and weakly changing the working conditions of the system to be tested. Such a technology, which has demonstrated to provide promising performances in terms of stability, sensitivity, frequency behaviour and scattering cross section, is a good candidate to accomplishing measurements in the close proximity of the radiator, eventually even in the reactive zone. This reduction of electrical distances between the AUT and the measurement surface, under the limits of standard antenna NF characterization facilities, adduces beneficial effects to the accuracy of the characterization, reducing the truncation error and the effects of environmental clutter on the data to be processed by NF-FF transformation.

In addiction to the non perturbing behaviour, the small-size and the lightweight of the ensemble, made up of sensor-mount-fiber, allow the development of Probe Array (PA), where the NF mapping is accomplished by means of dielectric sensors acquiring simultaneously multiple data samples. The faster acquisition, provided by PA's, can significantly speed up the measurement, reducing the operative costs. Accordingly specifications enforced on the stability of the measurement can be relaxed, allowing the realization of the

test facility with cheaper equipments. Furthermore, the easy handling of photonic sensors enables the realization of positioning system able to move over unconventional surfaces, leading eventually to radiator-tailored acquisition domains, that allows to reduce the truncation error and the scanning times.

Naturally, the possibility of accessing to the reactive zone of the radiator as well as performing acquisition on unconventional surfaces must be sustained by effective NF-FF transformation algorithms, capable to process the related measurement data. Indeed, the larger information content available in the very near field region or the unusual distribution of the field samples requires the development of new NF-FF algorithms, possibly phaseless, able to properly exploit the data in order to provide reliable and accurate estimate of the FF pattern.

The use of phaseless techniques can, indeed, significantly reduce the complexity of the antenna characterization facility, especially in the appealing millimetre and sub-millimetre bandwidths, where constraints imposed by phase measurements can hardly be satisfied and as a consequence the accuracy of the FF pattern estimate can be compromised up to became unacceptable. Therefore, NF-FF phaseless techniques require in general less sophisticated, hence, cheaper apparatus and can allow antenna NF characterization in all those cases where phase measurements are impracticable. It's worth noting that the reduction of the measurement distances between AUT and probe is particularly profitable when phaseless characterization is concerned, as it typically requires two different and sufficiently spaced measurement surfaces.

By conjugating the advantages of dielectric sensors with the benefits of phaseless techniques, a new generation of cost-effective NF antenna characterization systems can be developed, providing innovative features. Depending on the needs of the application, some features may be more appealing than others, and accordingly may be particularly pushed in the implementation of the system. Three main classes of NF test ranges can be individuated within this new generation of antenna characterization systems, each one focused on a peculiar feature.

- **Compact Near Field (CNF)** test range: antenna characterization system with test facility, whose dimensions are significantly reduced with respect to standard systems.

- **Fast Near Field (FNF)** test range: antenna characterization systems, where, to significantly speed up the measurement, a probe array is exploited to perform the NF mapping.

- **Very Near Field (VNF)** test range: antenna characterization systems, where field data are collected in the very NF region, in order to improve the stability and the reliability of phase retrieval algorithms or eventually to access to the invisible part of the PWS.

The chapter can be divided in two parts. The first one points out the potentialities of the proposed antenna characterization system, enlightening the innovative features it can provide. In particular, each one of the three main class just above introduced is separately discussed in a section. The second part deals with the experimentally validation of the innovative antenna characterization system. The results of a phaseless characterization of a standard gain horn (SGH) antenna both in the CNF and VNF test ranges are presented. The characterization system is based on a photonic probe, developed at AIST (see section 1.7) and made available thanks to a cooperation established between DIBET and AIST.

4.1 Compact Near Field Antenna Characterization

The use of photonic sensors for the NF mapping allows to significantly reduce the distance between the AUT and the probe under distances typically involved in conventional antenna NF characterization, that rarely are shorter that five wavelengths. Indeed, the dielectric nature of the probe, the connection with fiber optics ensures a small scattering-section acquisition system that makes negligible mutual coupling effects with the radiator, allowing to acquire field samples closer to the source or radiation. Therefore, when open surfaces are employed it is possible to acquire a higher dynamic range of the field intensities, obtaining a lower truncation on NF data that improves the accuracy and the reliability region of the FF estimate. Furthermore, the closer measurement may ensure a higher signal-to-noise ration (SNR) as a lower contribution from clutter reflection of side-walls can be collected in the measurement. Independently from the acquisition geometry, the closer measurement ensures also a reduction of acquisition times. A schematic of the problem is depicted in Fig. 4.1

Another important advantage deriving from the reduction distances in NF measurements concerns the dimensions of the test facilities. Indeed, anechoic environment can be consequently reduced, leading to a new class of antenna NF indoor characterization systems: Compact Near Field (CNF) test range. This is particularly appealing when dealing with low frequencies (f.i. VHF, UHF, L, bandwidths) as a compression of measurement set-up of just few

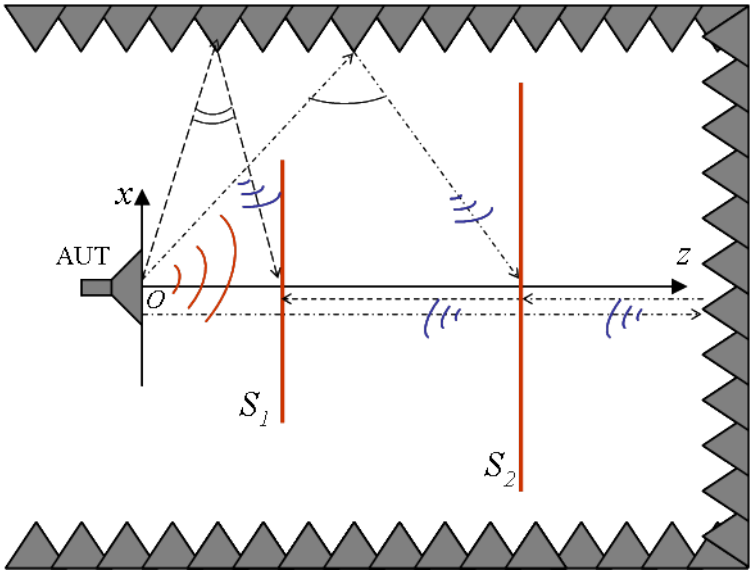

Figure 4.1: Schematic of side-wall clutter reflection

wavelengths $(4-5\lambda)$ can imply even meters of reduction in the dimensions of the anechoic chamber and, hence, bear down costs of test facility site realization. The potentiality of a CNF with respect to a standard NF facility (S-NF) are schematically illustrated in Fig. 4.2. The advantages of a CNF test range can be also enlightened by numerical (and later on by experimental, see section 4.4) arguments. To this end, we address planar acquisitions, referring to a horn antenna, having an aperture $193mm \times 144mm$ sized, a phase centre located $290mm$ behind the aperture, and working at $9GHz$ (Scientific Atlanta model no. 12-8-2 standard gain horn).

Let us then begin by pointing out that, as long as the scanning surfaces are moved away from the AUT, the spatial field distribution broadens and the measured field on the acquisition domains weakens. Accordingly, the truncation on the data worsen, when open surfaces are employed. At the same time, noise contribution arising from side-wall reflections can increase or can remain essentially unchanged, when moving away from the AUT. In any case, the SNR decreases. This is confirmed by Figs. 4.3 and 4.4 which report the numerical evaluations of the SNR and of the minimum truncation level of the measured field, respectively, when a planar surface, $260mm \times 180mm$ sized and centred to the AUT aperture is scanned at different distances from the AUT ranging in

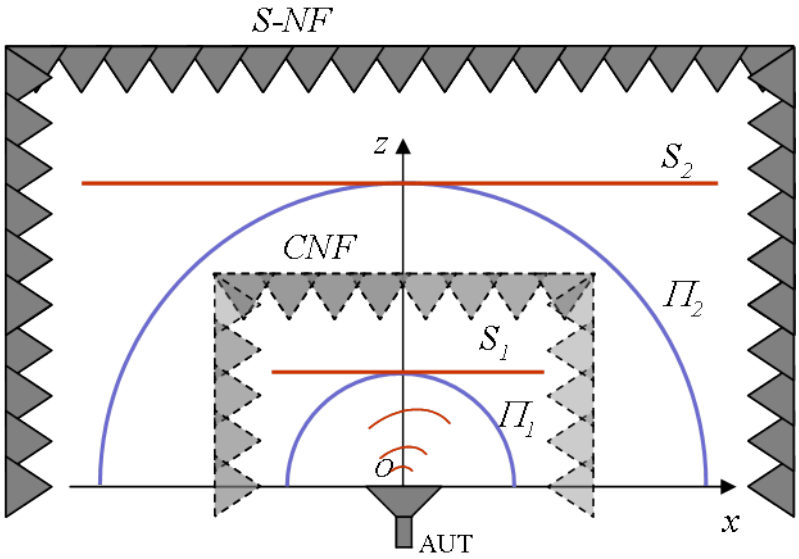

Figure 4.2: CNF and S-NF test range comparison: planar scan (red line), cylindrical scan (blu line)

$(0.2\lambda, 20\lambda)$. For sake of simplicity, noise power has been fixed to $-30dB$ with respect to the signal power at 0.2λ, and assumed constant at all the acquisition surfaces considered in the numerical analysis. Therefore, it does not account for changes of the clutter contribution due to side-wall reflections. Although referring to an ideal case, the analysis results can be considered representative of the the SNR behaviour in the actual experimental case.

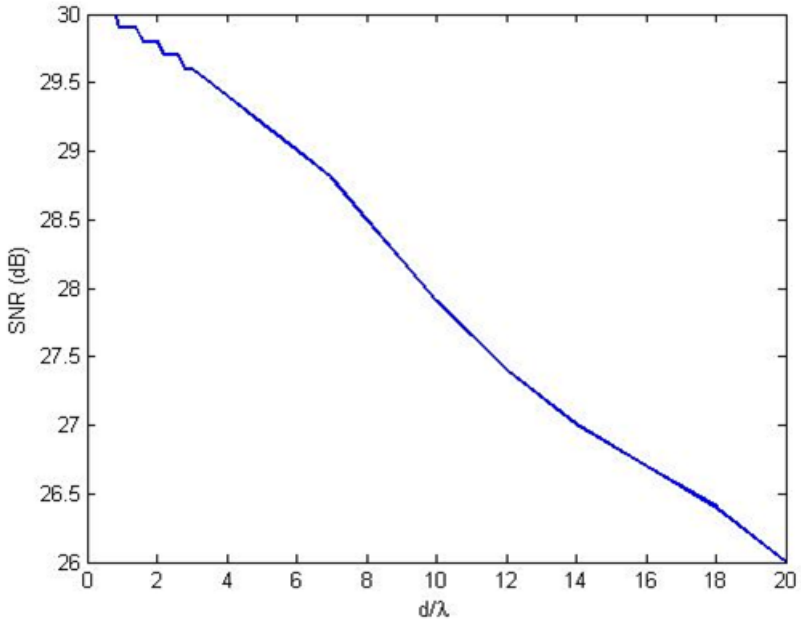

Figure 4.3: SNR against the reciprocal distance between AUT and measurement plane

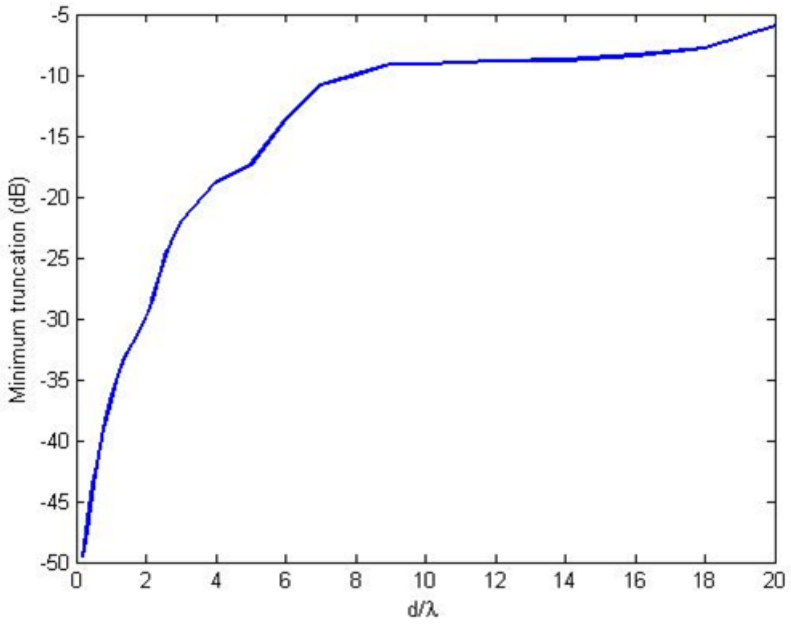

Figure 4.4: Minimum field truncation level against the reciprocal distance between AUT and measurement plane

As a consequence of these effects, the accuracy of the FF reconstructions from NF data worsens. Indeed, Fig. 4.5 shows the root mean square (RMS) error in the reconstruction of the FF amplitude by a complex transformation. Already for a probe-AUT distance of 6λ (a typical distance for metallic probes), the percentage RMS error is 21.3% and, to reach the 3% error corresponding to a distance of 0.4λ, the scanning surface should be extended to $1222mm \times 846mm$, i.e., to an overall area which is approximately 22 times bigger.

It's worth noting that as far as phaseless NF-FF transformations are concerned, the issue of bounding the test range dimensions is even more relevant as compared to standard (complex) ones since these techniques require larger measurement volumes, needing two, sufficiently spaced scanning surfaces to provide reliable results.

In a conventional NF facility only some pre-defined geometries are

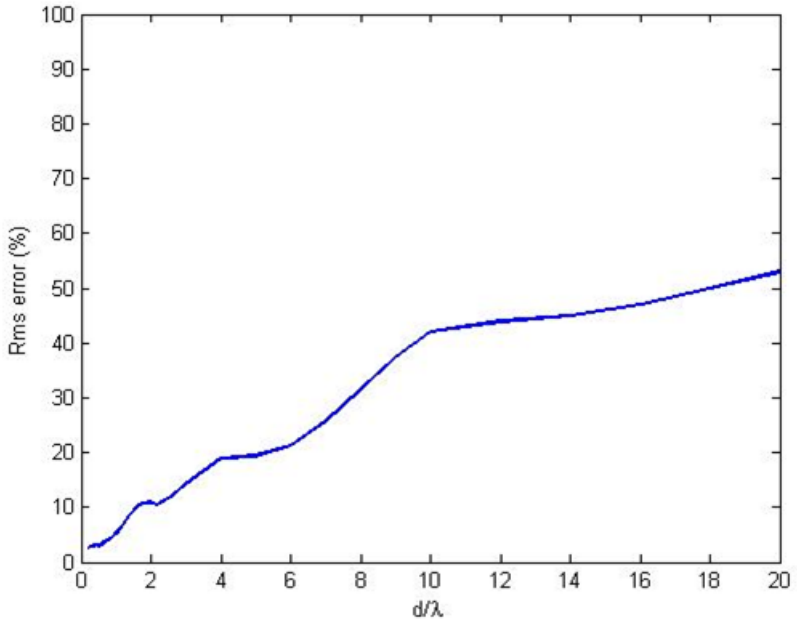

Figure 4.5: Rms error (%) in the estimation of the FF amplitude under a complex transformation against the reciprocal distance between AUT and measurement plane

implemented for the NF surface mapping and they typically are: planar and/or cylindrical and/or spherical. Metallic probes are weighty and cumbersome, especially when frequency decreases, therefore probe movement over surfaces with a non-standard geometry can be problematic. Instead, the easy handling of photonic sensors allows to realize positioning system able to freely move the probe along the three dimensions. Indeed, their lightweight enables the positioning system to perform an isolated longitudinal movement, that typically is not allowed in conventional systems. Accordingly, it is possible to perform acquisition of the field data on surfaces of unconventional geometry, eventually tailored for the considered radiator, in order to reduce the truncation error and/or the measurement time. Naturally, the processing of field samples distributed over non-standard surfaces must be accomplished by means of suited NF-FF techniques, able to operate with the chosen geometry. For sake of ex-

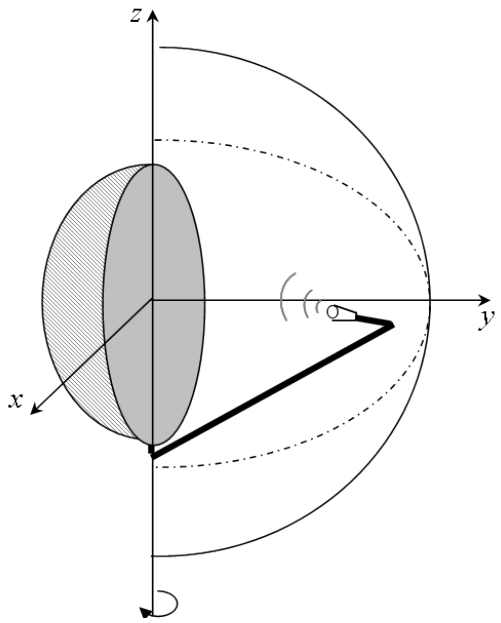

Figure 4.6: Unconventional geometry for NF measurement in a CNF: spherical acquisition surface (dash-dot), revolutionary ellipsoidal surface (dashed).

emplification, in Fig. 4.6 it is reported a possible unconventional geometry for the characterization of a reflector antenna (with a low ratio of diameter to

focal distance), where the presence of the feed can limit the minimum distance of acquisition in a planar scanning. Hence, to reduce the truncation error a cylindrical or spherical measurement surface can be exploited in conventional systems. In a CNF test facility, instead, it would be possible to use a revolutionary ellipsoidal surface, properly determined, tightening the measurement surface on the antenna and thus further reducing the acquisition domain, even when compared to the spherical geometry.

In summary, compact NF test ranges provides several advantages with respect to standard ones, that encompass:

(i) an significant improvement of the accuracy and reliability of the antenna NF characterization, thanks to a reduction of truncation error and also to the higher of signal-to-clutter;

(ii) a reduction of operating times;

(iii) a significant reduction of encumbrance of test facility.

4.2 Fast Near Field Characterization

Especially when dealing with the NF characterization of electrically large radiators, the NF mapping can require long measurement times, that can grow up to some days. This, naturally, bears on the operating cost as well as on the measurement apparatus costs as they are required to satisfy tighter time-stability specifications.

Photonic sensors can provide a significant speed up in the measurement, leading to Fast Near Field antenna characterization systems. Indeed, the non perturbing behaviour, the small size and the easy handling of dielectric probes allows the realisation of a probe array, where multiple sensors operate in parallel collecting simultaneously a set of field samples on the acquisition domain. It's worth noting that the entire ensemble made up of the probe, the mount and the connection can be essentially realised in dielectric material: thanks to the low lightweight of probe and fiber optic the realisation of mount can exploit low permittivity materials ($\epsilon_r \cong 1$) and, thus, the overall perturbation introduced in the measurement is negligible. Further the small size of the photonic sensors enables to put side by side multiple probes without practical limits on elements spacings. Therefore, the realization and, moreover, the use of a PA is

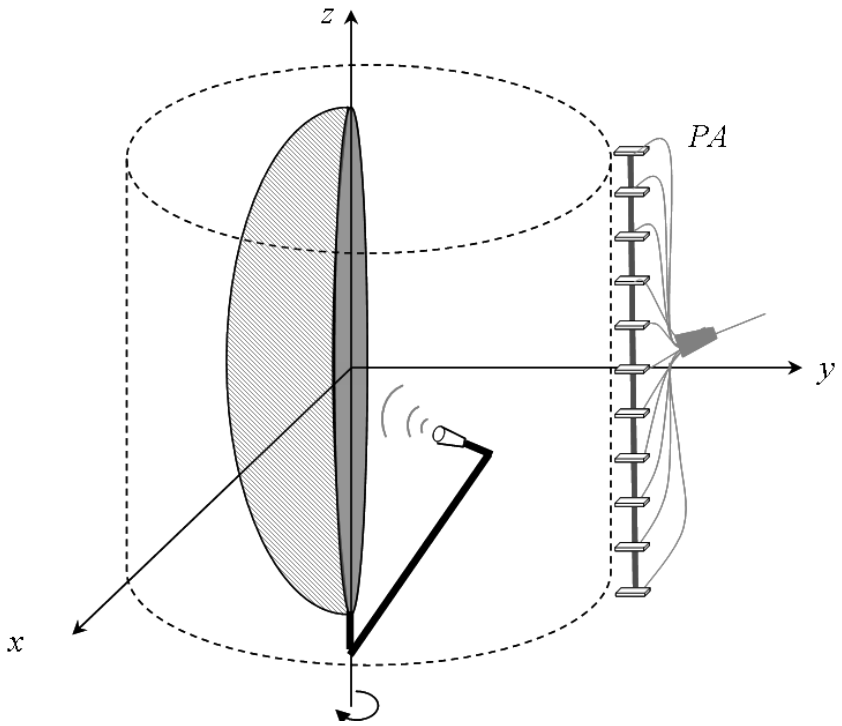

Figure 4.7: Probe array

feasible. In Fig. 4.7 a schematic of a PA is depicted.

A dielectric rod, holding multiple photonic sensors, can be used to realize a simple linear PA, suited for cylindrical or spherical geometries, where it could be able to simultaneously acquire an entire line of samples. As only AUT rotation is required, PA enables attractive *static* acquisition systems, where all the problems related to probe positioning and movement are drastically reduced [61, 62]. Naturally, more sophisticated configuration of PA, especially suited for operating on revolutionary geometries as the unconventional ellipsoidal surface (see section 4.1), can be realised.

In conclusion, the use of PA for NF antenna characterization is enabled by photonic sensors and leads to FNF test ranges, providing the following advantages:

(i) drastically reduce the characterization times;

(ii) a significant reduction of the operating costs;

(iii) a considerable relaxation of the stability constraints imposed on facility equipments (VNA, environmental condition controlling systems, amplifiers) by long-term measurements.

4.3 Very Near Field Characterization

The significant reduction of measurement distances in antenna characterization coming from the non invasive behaviour of photonic probe presents a remarkable potentiality: the possibility of accomplishing measurement in the Very Near Field (VNF) zone of the radiator, i.e. the reactive near field region according to [51]. Indeed, the different radiating regions typically con-

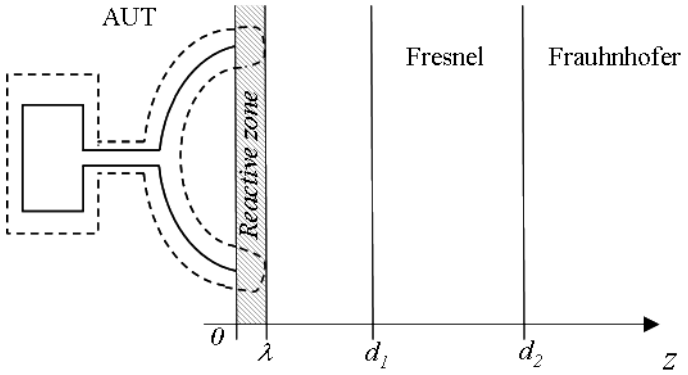

Figure 4.8: Antenna radiating regions

sidered in antenna application are schematically depicted in Fig. 4.8, where $d_1 = \sqrt{D/2\lambda}D/2 + \lambda$ and $d_2 = 2D^2/\lambda + \lambda$, being D the the radius of the small sphere containing the radiator and λ the wavelength.

In addiction to all the advantages above described, concerning the compactness of test facility, the accuracy (truncation error), the operating times, VNF measurements can enable the direct access practically to the quantity of interest in an antenna characterization, namely aperture field distribution. This significantly helps the reconstructions, especially for phaseless acquisitions, when the squared amplitude of the measured VNF approximates the squared amplitude of the unknown. This improves the reliability and the stability of

the inversion (see section 3.1), mitigating the trapping point

It's worth noting that the VNF region of the AUT may convey information also about the evanescent (invisible) part of the PWS, which is on the contrary unavailable under a standard NF scanning. Grasping this information requires even so the development of a proper VNF acquisition scheme. Indeed, although fast and effective NF sampling techniques are available throughout the literature [95], such strategies request the scanning surfaces to be at least some wavelengths apart from the radiator.

A complete discussion about a VNF sampling strategy is beyond the purposes of this work, nevertheless during the Ph. D. this problem has been started facing, achieving some interesting results. Therefore, we want here to trace the outline of a method for determining the sampling scheme in the VNF region, which is currently under development at DIBET.

The presence of the unknown invisible part of the PWS in the reactive zone does not allow to determine the bandwidth of the field and, then, the standard sampling strategy with half-wavelength (or quarter-wavelength in phaseless case) equally spaced samples may lead to aliasing in the represented PWS. Therefore, in principle, the field over surfaces in VNF should be properly oversampled in order to avoid folding of invisible PWS inside the visible region. The key point of the developed approach relies on the fact that information needed to evaluate the FF pattern is related to the only visible region of the PWS and, accordingly, it is not required to represent the PWS on its entire support, but it is sufficient to extract from the NF mapping the spectral content related to the visible region. Hence, field samples should be properly collect in order to allow the accurte determination of PWS only inside the visible region.

In other words, the proposed approach essentially aims to properly sample the very near field in order to reconstruct the components of the aperture field contributing to the FF pattern, i.e. the part of the aperture field accounting for the visible region. This consideration naturally leads to employ PSWFs (see section 3.3.1) as basis functions for the aperture field and, consequently, the problem amounts to find the field sample positions on the acquisition surface in order to correctly determine the N expansion coefficients, say c_n, of the aperture field with respect to to chase basis. To this purpose let us consider the discrete operator, say $\mathcal{T}$ that transforms the the aperture field to the M field values, E_m, at the sampling points, say $x_m,\ m = 1, \cdots, M$ and $M \geq N$. Naturally, if $\mathcal{T}$ is invertible, the determination of c_n's from E_m's at x_m's can be straightforwardly accomplished. As sampling points are unknowns of the problem, $\mathcal{T}(\rfloor_\infty, \cdots, \rfloor_\mathcal{N}; \S_\infty, \cdots, \S_\mathcal{M})$ can be considered as parametric oper-

ator on parameters $x_m,\ m = 1, \cdots, M$. Therefore, the problem turns into the determination of the set of parameters that allows to invert $\mathcal{T}$. To this purpose, it is possible to perform the optimization of a proper objective functional, based on $\mathcal{T}$ eigenvalues and exploiting x_m's as tuning parameters. The optimization, indeed, aims to determine the choice of x_m's and, hence, of the specific operator $\mathcal{T}$, that minimizes ill-conditioning.

A numerical test is here presented as supporting argumentation for the above discussion. For sake of simplicity let us refer to a 2d case: a linear aperture and a linear acquisition domain, parallel to the aperture ad spaced apart from it a distance d, equal to 0.3λ. The geometry of the problem is depicted in Fig. 4.9. According to the above consideration, the cost functional to

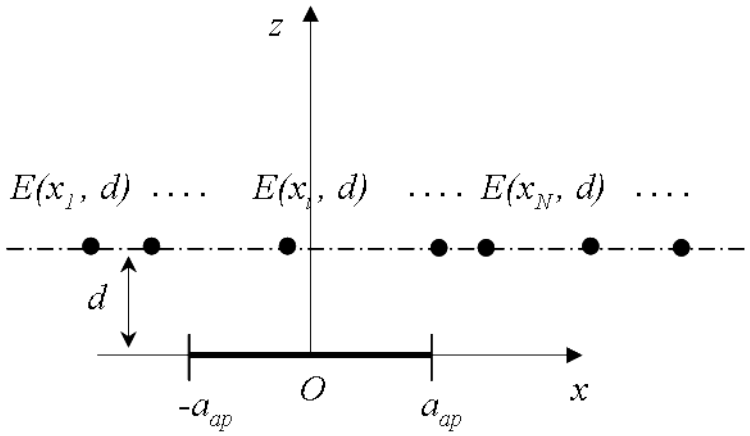

Figure 4.9: Exterior fields of radiating antenna

be optimised is:

$$\phi = \sum_{i=1}^{N} |\lambda_i| \tag{4.1}$$

As initial guess half-wavelength equally spaced samples have been chosen. Results of the optimization of the samples positions are depicted in Fig. 4.10 and the corresponding FF evaluations are depicted in 4.11. The numerical results indicate that the optimized sampling strategy and the PSWFs expansion provide a significant reduction of folding in the visible region of the PWS, ensuring a good estimate of FF pattern. In conclusion, VNF test ranges can provide:

(i) access nearly to the aperture field distribution;

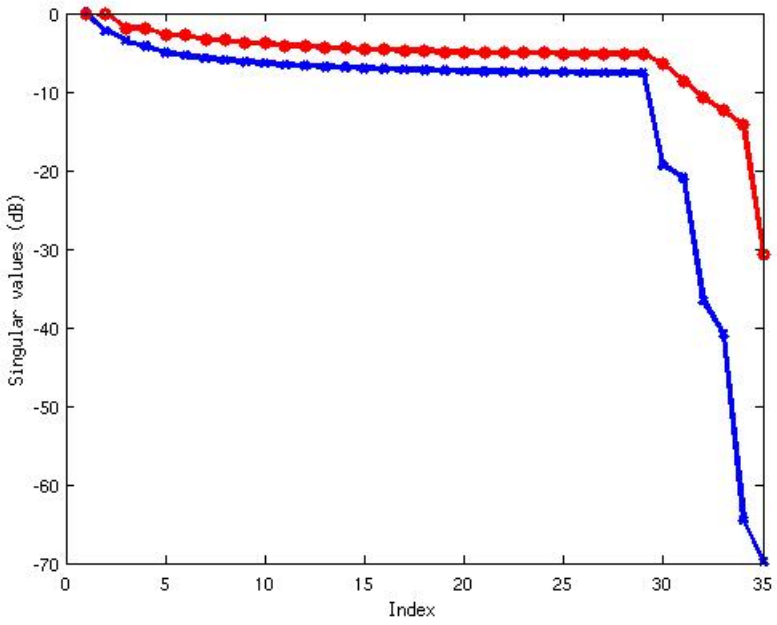

Figure 4.10: Eigenvalues dynamic: optimized eigenvalues (red line), half-wavelength sampling scheme eigenvalues (blue line).

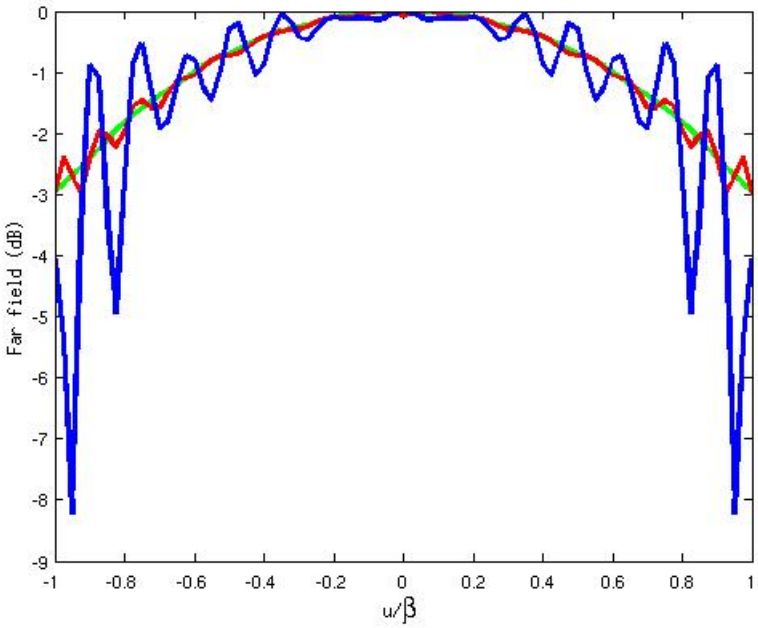

Figure 4.11: FF reconstruction: optimized sampling scheme (red line), half-wavelength sampling scheme (blue line), numerical reference (green line)

(ii) improvement of the stability and the reliability of phase retrieval algorithms.

4.4 Experimental Results

This section reports some representative experimental results that validate the non-invasive, phaseless antenna characterization systems proposed in this thesis. The systems conjugates the phaseless technique described in Chapter 3 and the EO probe, developed at AIST and described in section 1.7.
In particular, a CNF and a VNF test range has been developed and exploited for the experimental characterization of a standard antenna. For the CNF cylindrical geometry has been chosen for the acquisition domains, while planar geometry has been chosen for the VNF. In both cases, the AUT has been a horn antenna, having an aperture $193mm$x $144mm$ sized, a phase centre located $290mm$ behind the aperture, and working at $9GHz$ (Scientific Atlanta 12-8-2 standard gain horn).

Test facilities have been made available by AIST. In particular, the CNF has been implemented in the anechoic chamber for EMC measurement, located at AIST North Site, Tsukuba, while the VNF has been implemented in a semi-anechoic, planar test facility (Tokai Techno NF planar scanner NAS300), at Kyoto Research Park Corp.

For both CNF and VNF, the employed measurement chain is composed by a Radio-Frequency(RF) part and an optical part. The RF part of the measurement chain consists of a VNA Anritsu $37165A$ with $SM5392$ S-parameter test set, for planar measurements, and, in the cylindrical case, of a VNA is a HP $8719D$, a signal pre-amplifier HP $8348A$ and a power amplifier HP $8449B$. The optical part of the chain includes a Nec/Tokin OEFS-S1 optical controller, integrating a light source, a circulator and a photo-detector. In order to improve the SNR, a NTT Electronics optical amplifier FAS550DCS and a variable Agilent Technologies attenuator NTT 427 have been also used.

4.4.1 CNF Phaseless Characterization: Experimental Results

The following cylindrical surfaces have been considered during the measurement campaign:

- Surface Π_1: $[-22^\circ, 22^\circ]$ x $[-0.2m, 0.2m]$ at the distance of $33mm$ (1λ) from the AUT aperture when $\phi = 0$;

- Surface Π_2: $[-35^\circ, 35^\circ]$x$[-0.3m, 0.3m]$ at $22cm$ (7λ) from the AUT aperture when $\phi = 0$;

A uniform sampling has been employed with rates of 2° in the angular range and $2mm$ $(\lambda/10)$ along z axis on S_1 and 2° in the angular range and $8mm$ $(\lambda/4)$ along z axis on S_1 on S_2.

The geometry of the acquisition systems is schematically depicted in Fig. 4.12 Truncation level on the measurement data is about $-25dB$ with respect

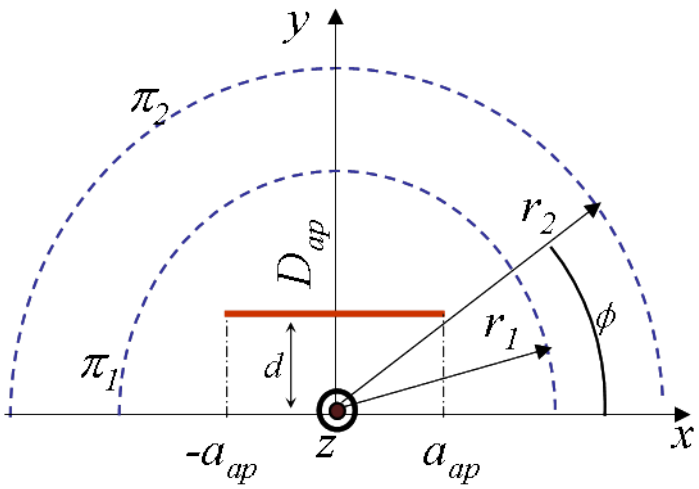

Figure 4.12: Top view of the cylindrical scanning geometry

to the maximum. A comparison between the estimated far-field (red solid line) by means of the developed phaseless technique and standard NF-FF transformation techniques on cuts parallel to the u-axis and v-axis is reported in Figs. 4.13 and 4.14, respectively.

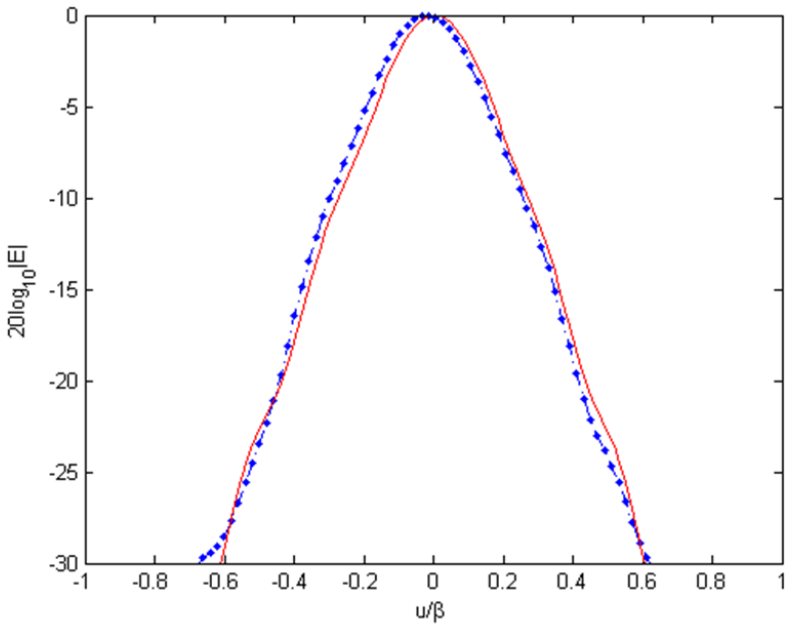

Figure 4.13: Far Field estimate on u- cut: developed phaseless algorithm (blue dash-dot line), standard NF-FF transformation techniques (red solid line).

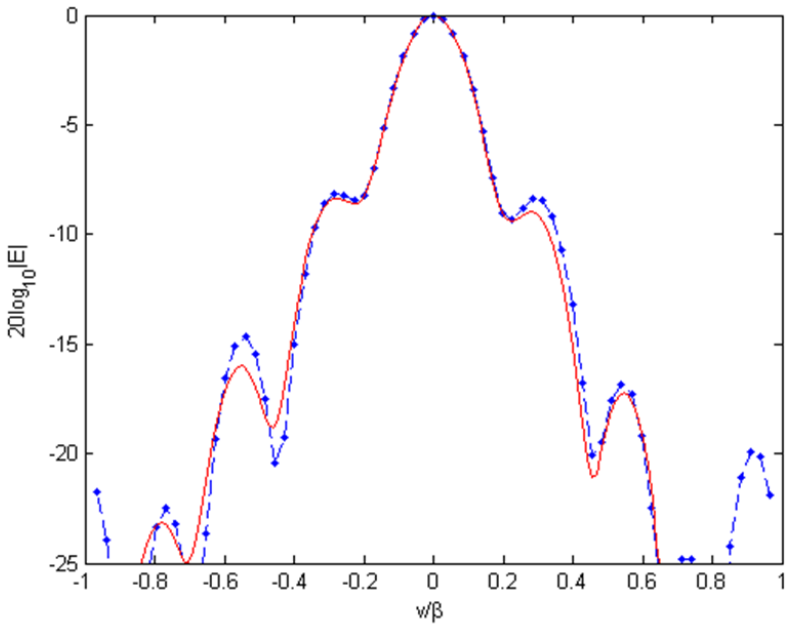

Figure 4.14: Far Field estimate on v- cut: developed phaseless algorithm (blue dash-dot line), standard NF-FF transformation techniques (red solid line)

4.4.2 VNF Phaseless Characterization: Experimental Results

The planar measurement surfaces that have been considered are:

- Surface S_1: $300mm$x$240mm$ sized apart from the AUT $10mm$ (0.33λ);
- Surface S_2: $400mm$x$400mm$ sized apart from the AUT $129mm$ (3.9λ);
- Surface S_3: $640mm$x$640mm$ sized apart from the AUT $295mm$ (8.9λ);

Surface S_1 resides in the VNF region (see Fig. 4.15), whereas surfaces S_2 and S_3 are located in the standard NF. Fig 4.14 shows a comparison between the cuts, along the v-axis, of the FFs as evaluated by the complex NF-FF procedure applied to the data collected over the three mentioned surfaces. For the sake of comparison, the surfaces S_2 and S_3 have been cut out to the same size as for surface S_1.

Although already pointed out in section 3.2 as well as in the literature [71, 72, 73], it is worth remarking also here the role of the PSWFs representation in effectively accounting for the a priori information on the AUT size and in filtering the measurement noise, with beneficial effects on the stability and the accuracy of the characterization algorithm achieving accurate results, as those depicted in Fig. 4.16. Indeed, in CNF test ranges, filtering the environmental noise is a crucial point. To this end, Fig. 4.17 illustrates the same patterns as for Fig. 4.16, but performing the complex NF-FF transformation without exploiting such a representation, with a worse overall accuracy. Figs. 4.18 and 4.19 illustrate a comparison between the cuts, along the u- and v-axes, respectively, of the retrieved FFs under complex and phaseless reconstructions when one of the two surfaces is in the VNF. The complex NF-FF transformation is the same as before when applied to surface S_1, while the phaseless NF-FF transformation has been applied to data from surfaces S_1 and S_2, which are approximately spaced 3.57λ apart. A good agreement can be appreciated between the complex and phaseless techniques.

VNF measurements allow to nearly directly accessing the quantity of interest during the AUT characterization, namely the aperture field. This significantly helps the reconstructions, especially for phaseless acquisitions, when the squared amplitude of the measured VNF approximates the squared amplitude of the unknown. Indeed, Figs. 4.20 and 4.21 illustrates the same comparison as for Figs. 4.18 and 4.19, but now when both the planar surfaces are in the NF range (surfaces S_2 and S_3), with a spacing of approximately 5λ , that is, larger than the reciprocal distance between surfaces S_1 and S_2. As it can be

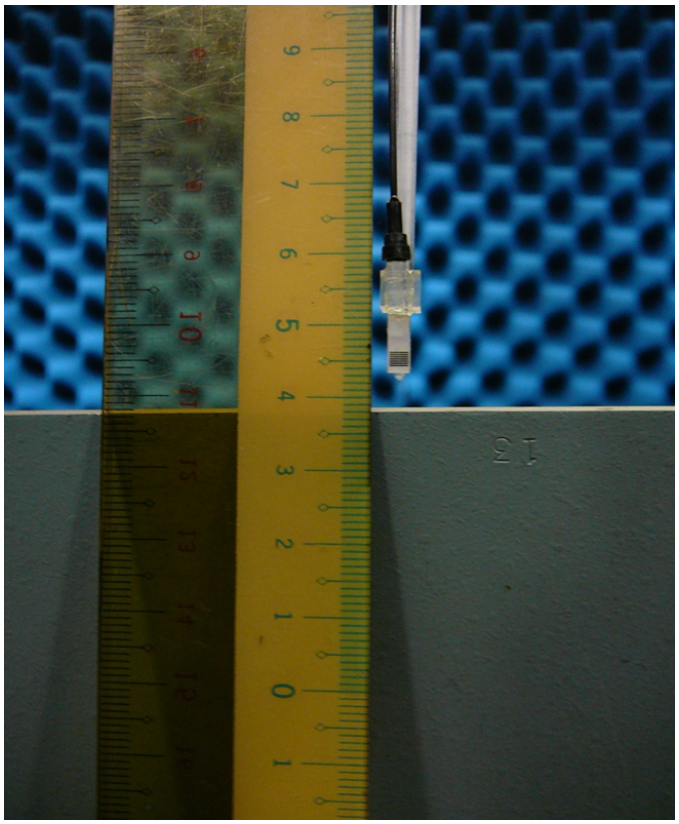

Figure 4.15: Very Near Field measurement: AUT-probe distance

seen, the best agreement between the complex and phaseless NF-FF transformations is obtained anyway when one of the two surfaces is very close to the antenna aperture.

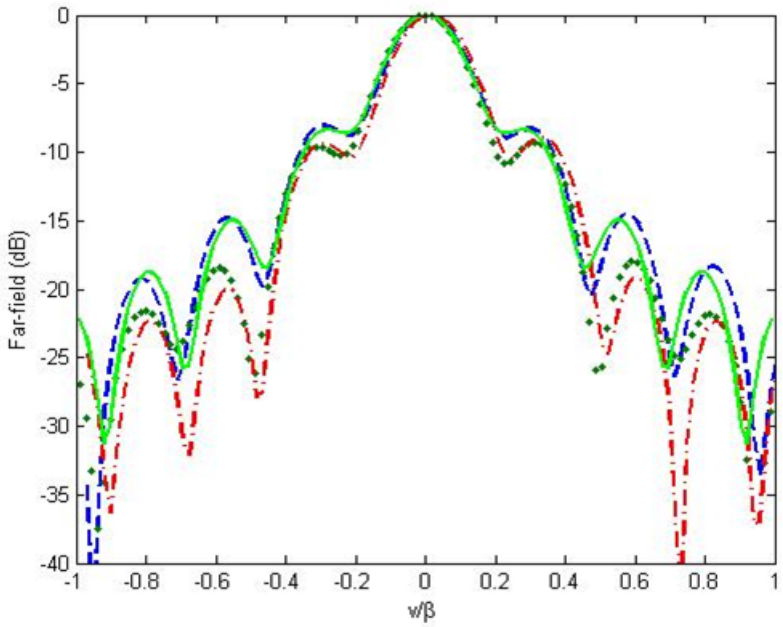

Figure 4.16: Cuts along the v-axis of the FF patterns retrieved from a planar scanning by complex NF-FF transformation. Green solid line: numerical reference. Blue dashed line: surface S_1. Green dotted line: surface S_2. Red dash-dot line: surface S_3

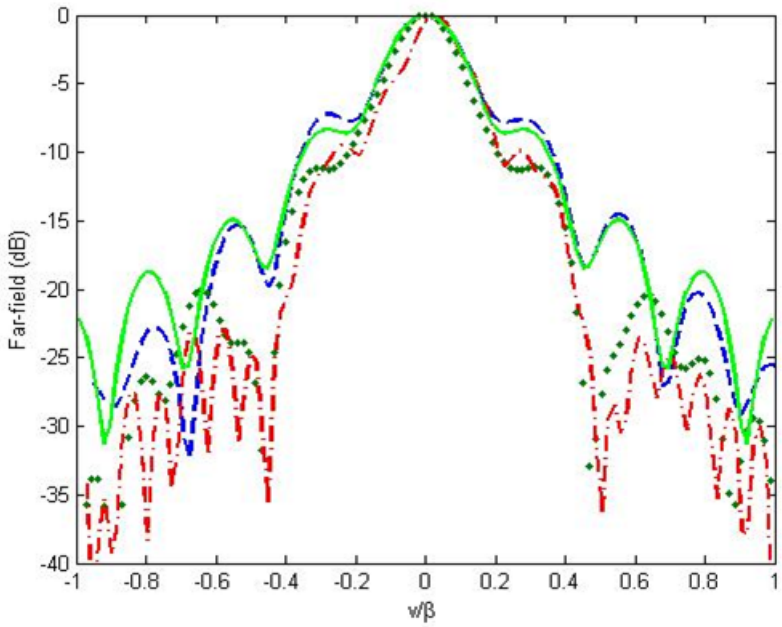

Figure 4.17: Cuts along the v-axis of the FF patterns retrieved from a planar scanning by complex NF-FF transformation without using the PSWFs representation. Solid line: numerical reference. Dashed line: surface S_1. Dotted line: surface S_2. Dash-dot line: surface S_3

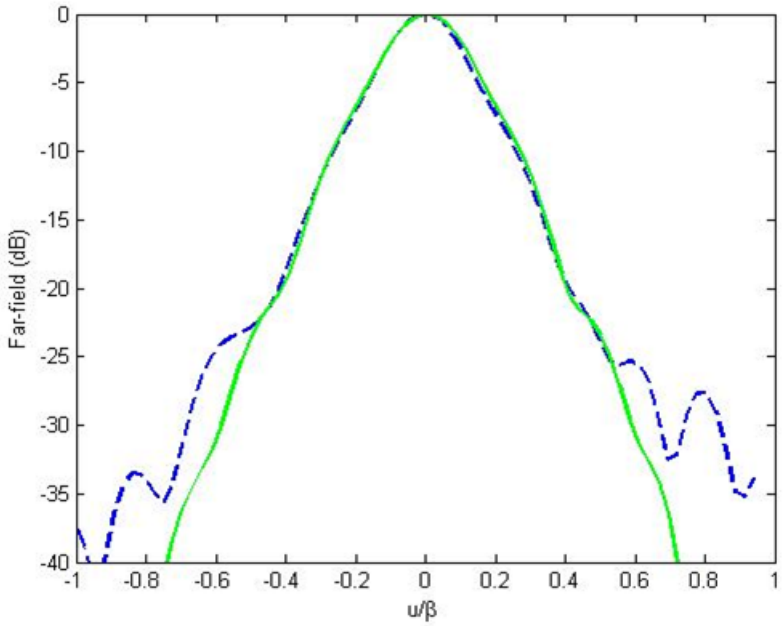

Figure 4.18: Cuts along the u-axis of the FF patterns retrieved from a planar scanning (surfaces S_1 and S_2). Solid line: reference complex NF-FF. Dashed line: phaseless NF-FF.

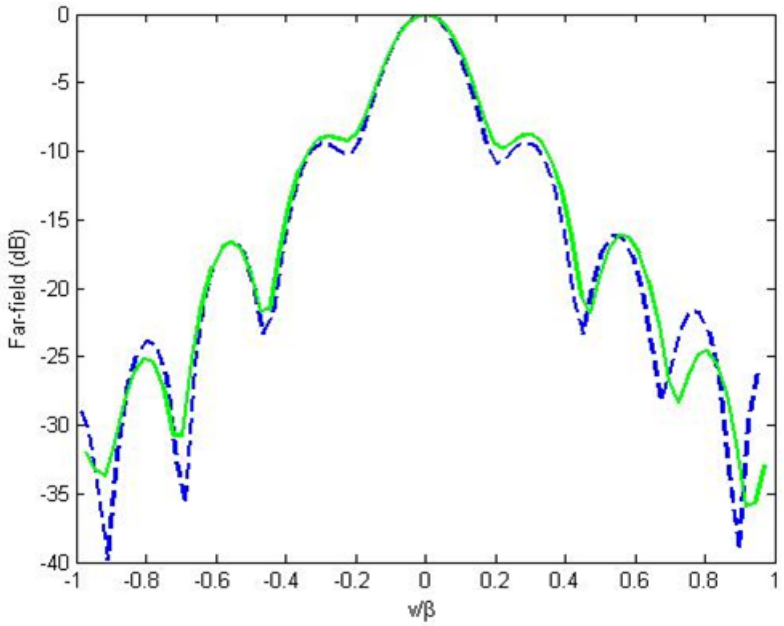

Figure 4.19: Cuts along the u-axis of the FF patterns retrieved from a planar scanning (surfaces S_1 and S_2). Solid line: reference complex NF-FF. Dashed line: phaseless NF-FF.

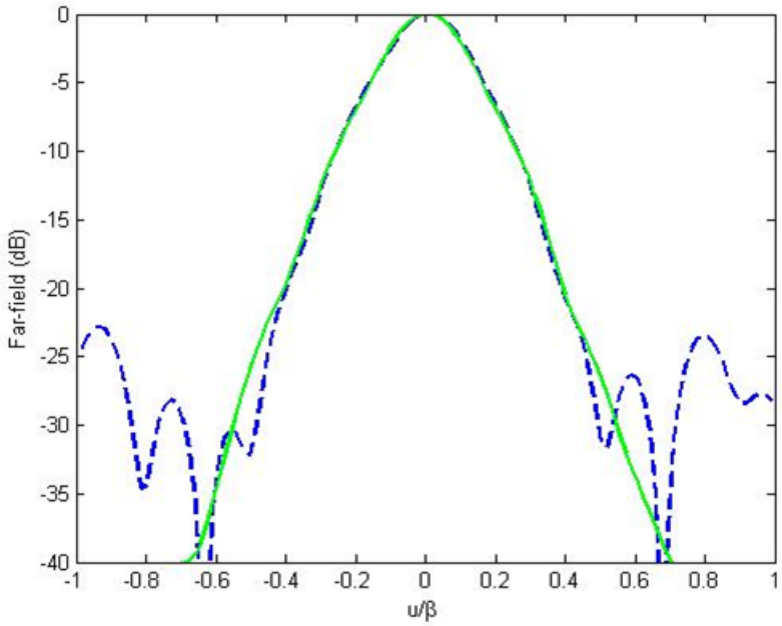

Figure 4.20: Cuts along the u-axis of the FF patterns retrieved from a planar scanning (surfaces S_1 and S_3). Solid line: reference complex NF-FF. Dashed line: phaseless NF-FF.

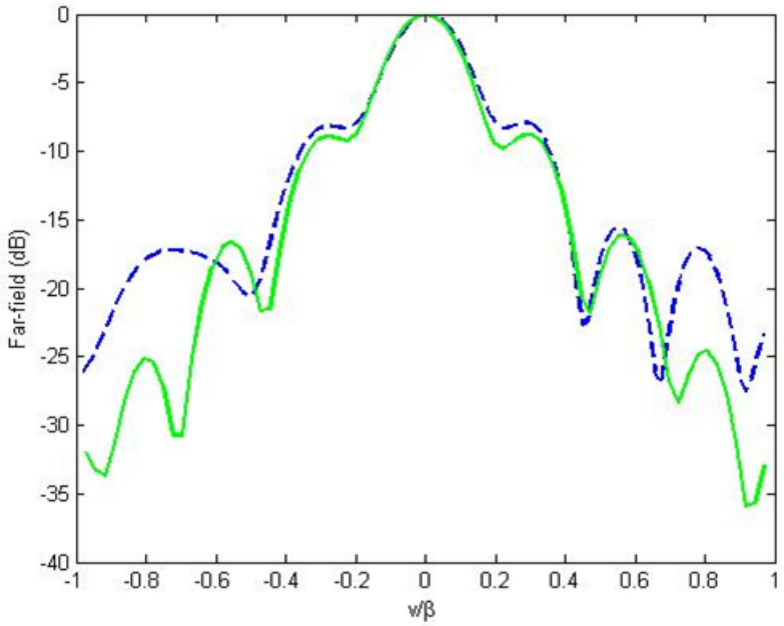

Figure 4.21: Cuts along the v-axis of the FF patterns retrieved from a planar scanning (surfaces S_1 and S_3). Solid line: reference complex NF-FF. Dashed line: phaseless NF-FF.

Bibliography

Bibliography

[1] J. A. Valdmanis, G. A. Mourou, C. W. Gabel, *Subpicosecond electrical sampling*, IEEE Journal of Quantum Electronics, vol. QE-19, pp. 664-667, April 1983.

[2] B. H. Kolner, D. M. Bloom, *Electro-optic sampling in GaAs integrated circuits*, IEEE Journal of Quantum Electronics, vol. QE-22, pp. 79, 1986.

[3] E. Yariv, *Quantum Electronics*, 3rd Edition, New York, Wiley & Sons, 1989.

[4] G. A. Massey, D. C. Erickson, and R. A. Kadlec, *Electromagnetic field components: their measurement using linear electrooptic and magnetooptic effects*, Applied Optics, vol. 14, no. 11, pp. 2712-2719, November 1975.

[5] M. L. VanBlaricum, *Photonic System for Antenna Applications*, Proc. of IEEE Aerospace Applications Conference, Vail, USA, February 5-12, 1994.

[6] K. D. Masterson, L. Driver, M. Kanda, *Photonic probes for the measurement of electromagnetic fields over broad bandwidths*, Proc. of IEEE National Symposium on Electromagnetic Compatibility, Denver, USA, May 23-25, 1989.

[7] H. Kopola, A. Thansandote, J. Chrostowski,S. S. Stuchly *An optical E-field sensor*, Proc. of IEEE National Symposium on Electromagnetic Compatibility, Ottawa, Canada, June 11-14, 1990.

[8] C. H. Bulmer, *Sensitive highly linear lithium Niobate interferometer for electromagnetic field sensing*, Applied Physics Letters, vol. 53, no. 24, pp. 2368-2370, December 1988.

[9] J. C. Bolomey,*Near Field antenna measurements techniques: current status and new trends*, Proc. of IEEE International Symposium on Antennas and Propagation, 2005

[10] T. Nagatsuma, *Characterization of millimeter-wave antenna using Photonic Measurement Techniques*, Int.. J. of RF and Microwave Computer-Aided Engineering, vol. 14, no.3, pp. 290-297, 2004.

[11] S. Grasso, M. Bellucci, G. Cocorullo et Al. *Thermo-optic design for microwave and millimeter-wave electromagnetic power microsensors*, Applied Optics, vol. 41, no. 18, pp. 3601-3612, 2002.

[12] M. N. Deeter, G. W. Day, T. J. Beahn and M. Manheimer *Magneto-optic field sensor with* $1.4pT/\sqrt{Hz}$ *minimum detectable field at* $1KHz$ Electronic Letters, vol. 29, no. 11, pp. 993-994, 1993.

[13] R. Heinzelmann, A. Stohr, M. GroS et Al. *Optically powered remote optical field sensor using an electro-absorption modulator* IEEE Microwave Symposium Digest, vol. 3, pp. 1225-1228, 1998.

[14] T. Nagatsuma,H. Togo, K. Narahara et Al., *Recent progress in optical measurement of radio-wave signal from gigahertz to terahertz*, IEEE Microwave Photonics, pp. 20-23, October 2004.

[15] E. Suzuki, E. Miyakawa, T. Ota et Al. *Characteristics of an optical magnetic probe consisting of a loop element and a bulk electro-optic crystals* Journal of the Magnetics Society of Japan, vol. 28, no. 2, pp 34-38, 2004.

[16] E. Suzuki, E. Miyakawa, T. Ota et Al. *Optical magnetic field sensing with a loop antenna element doubly-loaded with electro-optic crystals* Proc. of IEEE International Symposium on Electromagnetic Compatibility, vol. 1, pp. 88-91, May 2003.

[17] T. Meier,C. Kostrzewa,K. Peterman et Al. *Integrated optical E-field probe with segmented modulator electrodes*, Journal of Lightwave Technology, vol. 12, no. 8, pp. 1497-1503, August 1994.

[18] A. Capozzoli, G. D'Elia, M. Iodice, I. Rendina and P. Vinetti, *A photonic probe for antenna measurements*, Proc. of 9th Int. Conference on Electromagnetics in Adv. Application, Turin, Italy, Sept 12-16, 2005.

[19] M. Hirose, K. Komiyama, T. Ishizone *Antenna pattern measurement using photonic sensor and near-field scanning techniques*, IEICE TRANSACTIONS on Communications, vol. E87-B, pp. 727, 2004.

[20] M. Kuwabara,K. Tajima,R. Kobayashi et Al. *Development and Analysis of Electric Field Sensors Using $LiNbO_3$ Optical Modulator*, IEEE Transaction of Electromagnetic Compatibility, vol. 34, no. 4, pp. 391-395, November 1992.

[21] D. H. Naghski, J. T. Boyd, E. Howard et Al. *An Integrated Photonic Mach-Zehnder Interferometer with No Electrodes for Sensing Electric Fields*, Journal of Lightwave Technology, vol. 12, no.6, pp. 1092-1098, June 1994.

[22] Y. Yongjun,C. Fushen, *Optical Characteristics of the Optical E-Field Sensor Using $LiNbO_3$ M-Z Waveguides in the Static Field*, Proc. IEEE Int. Conf. on Communications, Circuits and Systems Proceedings, vol. 3, pp. 1975-1977, 25-28 June, 2006

[23] J. Born and H. Wolf, *Principles of Optics*, 7th Ed, Cambridge, Cambridge University Press , 2002.

[24] B. E. A. Saleh and M. C. Teich, *Fundamentals of Photonics*, New York, John Wiley & Sons.

[25] R. S. Weis and T. K. Gaylord, *$LiNbO_3$: summary of physical properties and crystal structure*, Appl. Physics A, vol. 37, pp. 191-203, 1985

[26] H. Adachi,K. Nagaoka,F. Tsunesada et Al. *Development and Analysis of Electric Field Sensors Using $LiNbO_3$ Optical Modulator*, IEEE Transaction on Electromagnetic Compatibility, vol. 34, no. 4, pp 391-398, November 2003.

[27] G. Keiser, *Optical Fiber Communications*, New York, McGraw-Hill, 1991.

[28] K. C. Gupta, R. Garg, I. Bahl and P. Barthia,*Microstrip lines and slotlines*, Norwood, Artec House, 1996.

[29] K. Chang, *Handbook of Optical Components and Engineering*, New York, John Wiley & Sons, 2003.

[30] C. A. Balanis, *Antenna Theory*, 3rd Ed., New York, John Wiley & Sons., 2005

[31] S. Miyazawa, *Ferroelectric domain inversion in Ti diffused $LiNbO_3$ optical waveguides*, Journal of Applied Physics, vol. 50, pp. 4599, 1979.

[32] M. Tasson, H. Legal, J. C. Gay et Al., *Piezoelectric study of poling mechanism in $LiNbO_3$ crystals at temperature close to the Curie point*, Ferroelectrics, vol. 13, pp. 479, 1976.

[33] L.B. Felsen and N. Marcuvitz, *Radiation and scattering of waves*, New York, John Wiley & Sons, 1994.

[34] I. Babuska, B. Uday, J. E. Osborn, *Generalized Finite Element Methods: Main Ideas, Results, and Perspective*, International Journal of Computational Methods, vol. 1, pp. 67, 2004.

[35] M. Hirose, T. Ishizone, J. Ichijoh et Al., *Planar Near-Field Measurements of Microstrip Array Antenna Using Photonic Sensor at X Band*, IEEE Antennas and Propagation Society Int. Symposium, 2003.

[36] H. Tanaka, M. Hirose, M. Nagatoshi, et Al., *Photonic Balun for Antenna Measurements Free of Coaxial Cables*, Int. Workshop in Antenna Technology: Small Antennas and Novel Metamaterials, 2008.

[37] S. Kurokawa, M. Hirose, *A New Balun for Antenna Measurement using Photonic Sensor*, Proc. of European Conference on Antennas and Propagation, November 2007.

[38] M. Hirose, S. Kurokawa, K. Komiyama, *Compact spherical near-field measurement system for UWB antennas*, IEEE Antennas and Propagation Society International Symposium, 2005.

[39] W. C. Gibson, *The Method of Moments in Electromagnetics*, Chapman & Hall/CRC, 2008.

[40] C. H. Bulmer, W. K. Bums, and S. C. Hiser, *$Ti : LiNbO_3$ linear interferometric modulators and photorefractive effects*, Proc. 7th Topical Meeting on Integrated and Guided-Wave Optics, Optical Soc. of America, pp. WC1-1-WC1-4, 1984.

[41] D. Paris and W. J. LEach and E. Joy, *Basic theory of probe-compensated near-field measurements*, IEEE Trans. on Antennas and Propagation, vol. 26, no. 3, pp. 373-379, 1978.

[42] M. Armenise, A. Capozzoli, C. Curcio, C. Cimminelli, G. D'Elia, A. Liseno and P. Vinetti, *Photonic field sensors for antenna status detection and dynamic control*, Proc. of First Mediterranean Photonics Conf., Ischia, Italy, 25-28 June, 2008.

[43] H. Y. Yee, *Natural resonant frequencies of microwave dielectric resonators*, IEEE Trans. Microwave Theory Technology, vol. MIT-13, no. 2, pp. 256, 1965.

[44] R. F. Hunsperger,*Integrated Optics* Springer, 2002.

[45] X. F. Cao, R. V. Ramaswamy, and R. Srivastava,*Characterization of Annealed Proton Exchanged LiNbO3 Waveguides for Nonlinear Frequency Conversion* Journal of Lightwave Technology, vol. 10, no. 9, pp. 1302-1313, 1992.

[46] B. T. Szentkuti, *Simple Analysis of Anisotropic Microstrip Lines by a Transform Method*, Electronic Letters, vol. 12, no. 25, pp. 672-673, December 1976.

[47] K. W. Hui, K. S. Chiang, B. Wu, Z. H. Zhang , *Electrode Optimization for High-Speed Traveling-Wave Integrated Optic Modulators*, Journal of Lightwave Technology, vol. 16, no. 2, pp. 232-238, 1998.

[48] R. Simons, *Coplanar Waveguide Circuits, Components, and Systems*, New York, John Wiley & Sons, 2001.

[49] W. Boyu , X. Guangjun, J. Xiaomin, *Travelling wave electrode optimisation for high speed electro-optic modulators using the Fourier series method*, IEE Proc. Optoelectron., Vol. 141, no. 6, 1994, pp. 381-390.

[50] D. M. Pozar, *Microwave Engineering*, New York, John Wiley & Sons, 1998.

[51] A. D. Yaghijan, *An Overview of Near Field Measurements*, IEEE Trans. Antennas Prop., vol. AP-34, n. 1, pp. 30-45, Jan. 1986.

[52] *Special Issue on Near-Field Scanning Technology*, IEEE Trans. Antennas Prop., vol. 36, 1988.

[53] D. Slater, *Near-field antenna measurements*, Artech House, Norwood, MA, 1991.

[54] R.C. Baird, A.C. Newell and C.F. Stubenrauch *A brief history of near-field measurements of antennas at the National Bureau of Standards*, IEEE Trans. Antennas Prop., vol. 36, n. 6, pp. 727-733, Jun. 1988.

[55] M.H.A. Paquay, *State of the art in antenna measurements in Europe*, Proc. of the IEE Antenna Measur. and SAR, Loughborough, England, May 25-26, 2004, pp. 14-18.

[56] D.W. Hess, R. Luna and J. McKenna, *Electromagnetic radome measurements: a review of automated systems*, Proc. of the Loughborough Antennas Prop. Conf., Loughborough, England, Apr. 4-6, 2005, CD-ROM.

[57] G.E. Evans, *Antenna measurement techniques*, Artech House, Boston, MA, 1990.

[58] IEEE Standard Test Procedures for Antennas - ANSI IEEE Std 149-1979 (Reaff. 1990).

[59] J. Saily and P. Eskelinen, *Enhancing the Frequency Stability of a Millimeter Wave Network Analyzer with an Add-On Unit*, Proc. of the IEEE Int. Freq. Control Symp., Tampa, USA, May 2003, pp. 521-523.

[60] J. Saily, P. Eskelinen, and A. V. Rijislinen, *Pilot Signal-Based Real-Time Measurement and Correction of Phase Errors Caused by Microwave Cable Flexing in Planar Near-Field Tests*, IEEE Trans. Antennas Prop., vol. AP-5I, no. 2, February 2003, pp. 195-200.

[61] D. Slater, *Three-Axis Motion Tracking Interferometer for Measurement and Correction of Positional Errors Between an Article Under Test and a Measurement Probe*, US Patent no. 5, 419, 631, May 1995.

[62] R. G. Yaccarmno and Y. Rahmat-Samii, *A Comparison of Conventional and Phaseless Planar Near-Field Antenna Measurements: The Effect of Probe Positioning Errors*, Proc. of the IEEE Int. Conf. on Phased Array Systems and Tech., Dana Point, CA, USA, May 2000, pp. 525-528.

[63] O. M. Bucci, G. D'Elia, G. Leone and R. Pierri, *Far-Field pattern determination from the near-field amplitude on two surfaces*, IEEE Transaction on Antennas and Propagation, vol. 38, pp. 1772, 1988

[64] T. Isernia, G. Leone and R. Pierri, *Radiation pattern evaluation from near-field intensities on planes*, IEEE Transaction on Antennas and Propagation, vol. 44, no. 5, pp. 701, 1996.

[65] R. G. Yaccarino and Y. Rahmat-Samii, *Phaseless bi-polar planar near-field measurements and diagnostics of array antennas*, IEEE Transaction on Antennas and Propagation, vol. 47, pp. 574, 1999.

[66] R. Pierri, G. D'Elia and F. Soldovieri, *A two probes scanning phaseless near-field far-field transformation technique* IEEE Transaction on Antennas and Propagation, vol. 47, no. 5, pp. 792-802, 1999.

[67] O. M. Bucci, G.'DElia and M. D. Migliore, *An effective near-field far-field transformation technique from truncated and inaccurate amplitude-only data*, IEEE Transaction on Antennas and Propagation, vol. 47, no. 9, pp. 1377-1385, 1999.

[68] A. Capozzoli and G. D'Elia, *Global optimization and antennas synthesis and diagnostics, part one: concepts, tools, strategies and performances*, Progr. Electromagnetic Res. PIER, vol. 56, no. 195, 2006.

[69] A. Capozzoli and G. D'Elia, *Global optimization and antennas synthesis and diagnostics, part two: applications to advanced reflector antennas synthesis and diagnosis techniques*, Progr. Electromagnetic Res. PIER, vol. 56, pp. 233-261, 2006.

[70] R. Barakat and G. Newsam *Algorithms for reconstruction of partially known, bandlimited Fourier pairs from noisy data: the nonlinear problem of phase retrieval*, Journal of Int. Equ. Suppl., vol. 9, pp. 77, 1985

[71] A. Capozzoli, C. Curcio, G. D'Elia and A. Liseno, *Phaseless Antenna Characterization by Prolate Function Expansion on the Aperture Field*, Microwave and Optical Technology Letters,**48**,2060, 2006.

[72] A. Capozzoli, G. D'Elia and A. Liseno, *Phaseless antenna characterization Efficient spectral representation and non-uniform spatial sampling*, First AMTA Europe Symposium, Munich, Germany, May 1-4 2006.

[73] A. Capozzoli, C. Curcio, G. D'Elia, A. Liseno, *Phaseless antenna characterization by effective aperture field and data representations*, in print on IEEE Trans. Antennas Prop

[74] A. Capozzoli, C. Curcio, G. D'Elia et Al., *Characterization of a Real World Antenna by Means of Only Amplitude Data*, Antennas and Propagation Magazine,**48**,200, 2006.

[75] A. Capozzoli, C. Curcio, G. D'Elia et Al., *Accuracy and Reliability in Phaseless Antennas Characterization*, Microwave and Optical Technology Letters,**48**,2060, 2007.

[76] A. Capozzoli, C. Curcio, G. D'Elia et Al., *Effective antenna characterization at millimeter-wave frequencies and experimental validation at 100GHz*, Proc. of EuCAP06, Nice (France), Nov. 6-10, 2006.

[77] A. Capozzoli, C. Curcio, G. D'Elia, A. Liseno, *Millimeter-wave phaseless antenna characterization*, IEEE Trans. Instr. Measur., vol. 57, n. 7, pp. 1330-1337, Jul. 2008.

[78] L. S. Taylor *The Phase Retrieval Problem*, Transaction on Antennas and Propagation, vol. 29, pp. 386, 1981

[79] N. E. Hunt, *Phase Retrieval and Zero Crossings*, Kluwer Academic Publishers, 1989

[80] H. P. Baltes, *in Inverse Source Problems in Optics* Springer-Verlag Ed., 1983

[81] R. P. Millane, *Phase Retrieval in Crystallography and Optics*, Journal of Optical Society American A, vol. 7, pp. 394, 1990

[82] A. T. Bajkova, *Phaseless VLBI Mapping of Compact Extragalactic Radio Sources*, Astronomy Letters, vol. 30, no. 4, pp. 218-231, April 2004.

[83] A. Kirsch, *An Introduction to Mathematical Theory of Inverse Problems*, New York, Springer, 1996.

[84] R. H. T. Bates, *Fourier Phase Problems are Uniquely Solvable in More than One Dimension 1: Underlying Theory*, Optik, vol. 61, pp. 247, 1982

[85] R. Barakat and G. Newsam, *Necessary Conditions for a Unique Solution to Two-Dimensional Phase Recovery*, Journal of Mathematical Physics, vol. 25, pp. 3190, 1984.

[86] I. S. Stefanescu, *On the phase retrieval problem in two dimensions*, Journal of Mathematical Physics, vol. 26, 2141, 1985.

[87] M. S. Scivier, *Phase ambiguities and the zeros of multidimensional band-limited functions*, Journal of Optical Society American A, 1985.

[88] J. R. Fienup, *Reconstruction of a complex-valued object from the modulus of its Fourier transform using a support constraint*, Journal of Optical Society American A, vol. 4, 1987.

[89] J. H. Seldin and J. R. Fienup,*Numerical investigation of the uniqueness of phase retrieval*, Journal of Optical Society American A, 1990

[90] T. Iserna, G. Leone and R. Pierri, *Phase retrieval of radiated fields*, Inverse Problems, vol. 11, pp. 183, 1995.

[91] T. Iserna, G. Leone and R. Pierri, *A quadratic inverse problem: the phase retrieval* Inverse Methods in Action, Ed. P C Sabatier (Berlin: Springer), 1990

[92] Y. S. El-Said and A. M. Attiya, *Modified two-probe approach for amplitude only near-field measurements*, Procedings of 21^{st} National Radio Science Conference, 2004

[93] J. C. Dainty and M. A. Fiddy, *The Essential Role of Priori Knowledge in Phase Retrieval*, Journal of Modern Optics, vol. 31, pp. 325, 1984.

[94] T. Isernia, G. Leone, R. Pierri and F. Soldovieri, *Role of support information and zero locations in phase retrieval by a quadratic approach*, Journal of Optical Society America A, vol. 16, pp. 1845, 1999.

[95] O. M. Bucci and G. D'Elia, *Advanced Sampling Techniques in Electromagnetics*, Review of Radio Science 1993-1996, Oxford University Press, 1996.

[96] J. A. Stratton, *Electromagnetic theory*, McGraw-Hill, 1941.

[97] D. Slepian and H. O. Pollak *Prolate spheroidal wave functions, Fourier analysis and uncertainty:I*, Bell System Technical Journal, vol. 1, 1961.

[98] H. J. Landau and H. O. Pollak, *Prolate spheroidal wave functions, Fourier analysis and uncertainty: II. The dimension of essentially time- and band-limited signals*, Bell System Technical Journal, vol. 41, pp. 1295, 1962

[99] H. J. Landau and H. O. Pollak, *Prolate spheroidal wave functions, Fourier analysis and uncertainty. III. The dimension of essentially time- and band-limited signals*, Bell System Technical Journal, vol. 41, pp. 1295, 1962.

[100] D. Splepian, *Prolate spheroidal wave functions, Fourier analysis and uncertainty: IV. Extension to many dimensions; generalized prolate spheroidal funstions*, Bell System Technical Journal, vol. 43, pp. 3009, 1964.

[101] G. D. de Villiers, F. B. T. Marchaud and E. R. Pike, *Generalized Gaussian quadrature applied to an inverse problem in antenna theory. II. The two-dimensional case with circular symmetry*, Inverse Problems, vol. 19, pp. 775, 2003.

[102] R. A. Horn and C. R. Johnson, *Topics in Matrix Analysis*, Cambridge University Press, 1991.

[103] G. Szego, *Orthogonal polynomials*, Publication of American Mathematical Society Collection, **23**, 1939

[104] E.Z. Anderson,C. Bai, S. Bischof and Al.,*LAPACK User's Guide 3rd Ed.*, Society of Industrial and Applied Mathematics, 1999.

[105] Å. Björck and G. H. Golub, *Numerical methods for computing angles between linear subspaces*, Math. Comp., vol. 27, pp. 579, 1973.

[106] O. M. Bucci, G. D'Elia, F. Soldovieri and R. Pierri, *An effective strategy in the planar near-field far-field transformation for focussing antennas*, Proc. of the 20th ESTEC Antenna Workshop on Millimeter-Wave Antenna Tech. and Antenna Measur., 1997

[107] O. M. Bucci, A. Capozzoli, C. Curcio, G. D'Elia, S. Musto, *A filtering strategy of the environmental noise on near-field data and its application to near-field far-field transformation techniques*, Procedings of the 3rd ESA Workshop on Millimetre Wave Tech. and Appl., Espoo, Finland pp. 609-614, 2003.

[108] O. M. Bucci, G. D'Elia, M. D. Migliore, *A general and effective clutter filtering strategy in near-field antenna measurements*, IEE Procedings on Microwave Antennas and Propagation, vol. 151,pp. 227, 2004.

[109] A. V. Räisänen, J. Ala-Laurinaho, J. Häkli et Al, *Measurement of high-gain antennas at mm- and submm- wavelengths: challenges and solutions*, Procedings of 1st AMTA Europe Symposium., pp. 12-17, 2006.

[110] P.C. Clemmow,*Plane wave spectrum representation of electromagnetic fields*, IEEE Press, 1996.

[111] T. B. Hansen and A. D. Yaghjian, *Plane-Wave Theory of Time-Domain Fields: Near-Field Scanning Applications* IEEE Press, 1999.

[112] M.J.D. Powell, *Convergence properties of algorithms for nonlinear optimization*, SIAM Review, vol. 28, n. 4, pp. 487-500, 1986.

[113] G. D'Elia, G. Leone, R. Pierri and G. Schirinzi, *'Traveling' sampling of scattered fields*, Proc. of the Antennas and Prop. Int. Symp. (APS), vol. 23, pp. 531-534, Jun. 1985.

[114] O.M. Bucci, G. D'Elia, G. Mazzarella, G. Panariello, *Antenna pattern synthesis: a new general approach*, Proc. of the IEEE, vol. 82, n. 3, pp. 358-371, Mar. 1994.

[115] H.H. Bauschke, P.L. Combettes and D.R. Luke, *Phase retrieval, error reduction algorithm, and Fienup variants: a view from convex optimization*, J. Opt. Soc. Am. A, vol. 19, n. 7, pp. 1334-1345, Jul. 2002.

[116] A. C. Newell, *Error Analysis Techniques for Planar Near-Field Measurements*, IEEE Trans. on Antennas and Propagation, vol. 36, no.6, 1988.

[117]

[118] S. F. Razavi and Y. Rabmat-Samii, Phaseless Planar Near Field Measurements for Scanned Beams: Difficulties, a Hybrid Solution and Measured Results, IEEE International Symposium on Antennas and Propagation Digest, Albuquerque, NM, July 9-14, 2006, pp. 429-432.

[119] S. F. Razavi and Y. Rahmat-Samii, *A New Look at Phaseless Planar Near Field Measurements: Limitations, Simulations, Measurements, and a Hybrid Solution*, Proc. of the 28 bhA M'TA Annual S vmp., Austin, TX, October 22-27, 2006.

[120] A. Capozzoli, R. Ciotola, C. Curcio, G. D'Elia, 1. De Colibus and A. Liseno, *Experimental Testing of Scanned-Beam Antennas from Amplitude-Only Data*, Internal Report, Università di Napoli Federico JI-SELEX Sistemi Integrati S.p.A., December 2006 (confidential).

[121] *A new, non perturbing system, for the measurement of high frequency electromagnetic fields*, Progetto di Rilevante Interesse Nazionale (PRIN), Research Program Funded by the Italian Ministry for University and Research, April 2005, National coordinator: G. D'Elia.

[122] *Crystal Technology Lithium Niobate data sheet*, Crystal Technology Inc. (http://www.crystaltechnology.com/), Palo Alto, USA